

AD-A033 836

TORONTO UNIV (ONTARIO) INST FOR AEROSPACE STUDIES
ION TEMPERATURE MEASUREMENT IN A FLOWING COLLISIONLESS PLASMA U--ETC(U)
JUL 76 H P MERCURE
UTIAS-202

F/G 20/9

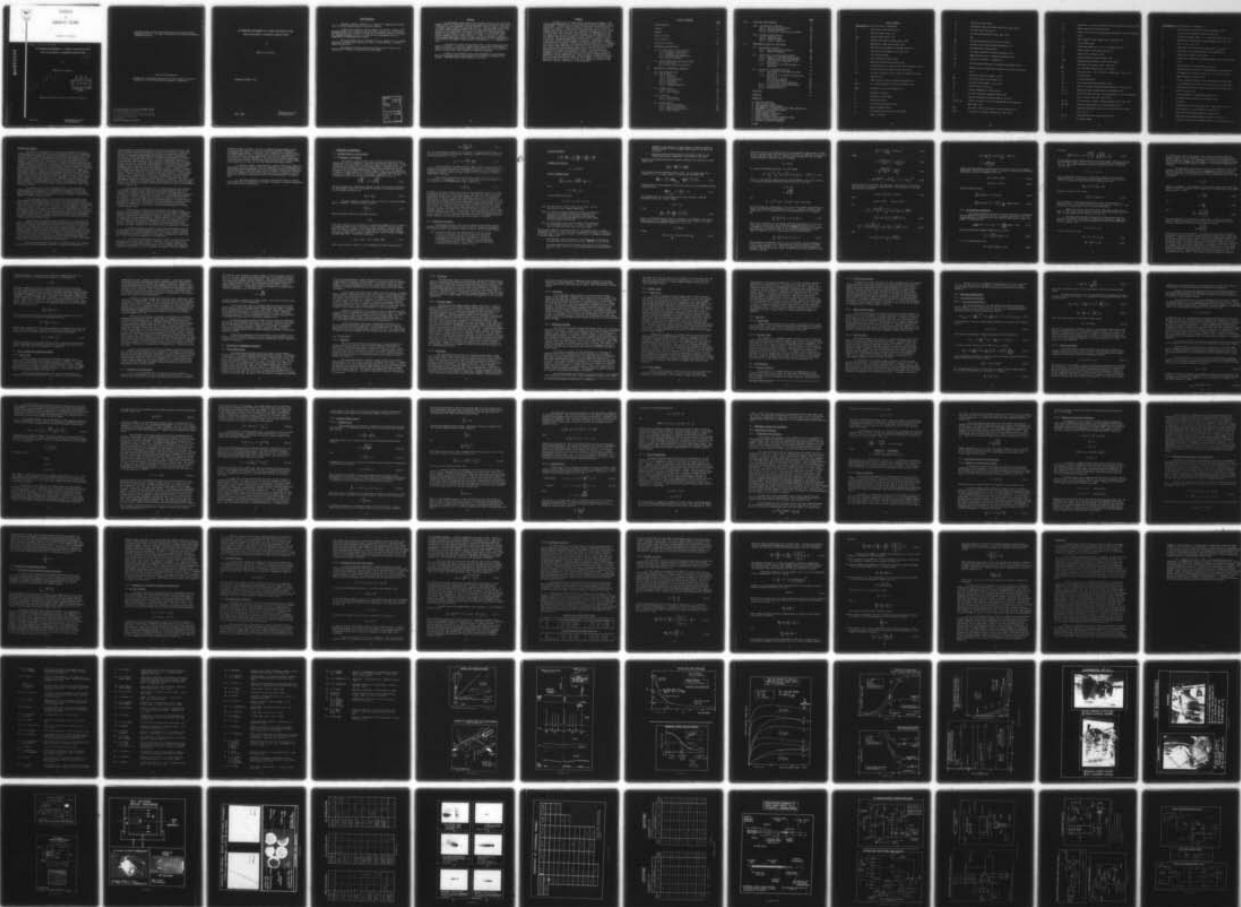
AF-AFOSR-2091-71

AFOSR-TR-76-1411

NL

UNCLASSIFIED

1 of 2
AD
A033836





INSTITUTE
FOR
AEROSPACE STUDIES

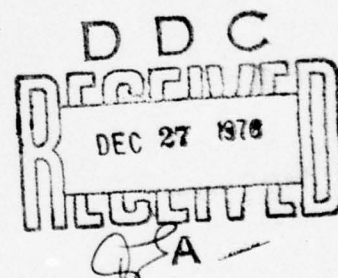
UNIVERSITY OF TORONTO

AFOSR - TR - 76 - 1411

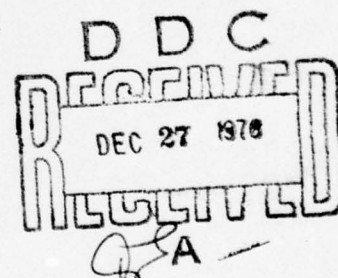
ION TEMPERATURE MEASUREMENT IN A FLOWING COLLISIONLESS PLASMA
USING AN END EFFECT OF CYLINDRICAL LANGMUIR PROBES

by

Hubert P.-E. Mercure



12
B.S.



Approved for public release; distribution unlimited.

July, 1976

UTIAS Report No. 202
CN ISSN 0082-5255

ADA 033836

Qualified requestors may obtain additional copies from the Defense Documentation Center, all others should apply to the National Technical Information Service.

Conditions of Reproduction

Reproduction, translation, publication, use and disposal in whole or in part by or for the United States Government is permitted.

AIR FORCE OFFICE OF SCIENTIFIC RESEARCH (AFSC)
NOTICE OF TRANSMITTAL TO DDC

This technical report has been reviewed and is approved for public release IAW AFR 190-12 (7b). Distribution is unlimited.

A. D. BLOSE
Technical Information Officer

ION TEMPERATURE MEASUREMENT IN A FLOWING COLLISIONLESS PLASMA
USING AN END EFFECT OF CYLINDRICAL LANGMUIR PROBES

by

Hubert P.-E. Mercure

Submitted December, 1975

July, 1976

UTIAS Report No. 202
CN ISSN 0082-5255

Acknowledgements

The author wishes to thank Dr. J. H. deLeeuw for suggesting this topic and for his many enlightening and stimulating comments.

I would like to express a special thanks to Mr. Jacob I. Unger for his valuable guidance on all aspects of the electronic equipment used in conjunction with this project and to my fellow student David Tong for his helpful discussions. The computing assistance of Mr. W. O. Graf and the craftsmanship of Mr. A. Bragg-Smith are acknowledged with thanks.

My sincere thanks are also extended to Miss M. Dagenais for her constant assistance in preparing the figures and to Mrs. W. Dillon and Mrs D. Finlay for typing the manuscript.

The financial assistance provided under DRB Grant No. 9510-111 and USAF/AFOSR No. 71-2091 is also gratefully acknowledged.

ACCESSION for	
NTIS	White Section <input checked="" type="checkbox"/>
DOC	Buff Section <input type="checkbox"/>
UNANNOUNCED	<input type="checkbox"/>
JUSTIFICATION.....	
BY.....	
DISTRIBUTION/AVAILABILITY CODES	
Dist.	Avail. Code
A	

Abstract

An experimental verification of the end effect theory of long cylindrical Langmuir probes in a high-speed collisionless plasma flow is reported. This effect is observed as a sharp departure from the predicted 'infinite probe' current when a strongly negative probe is aligned with the flow. Both the height and the width of the ion current peak measured about the zero-degree attitude are strongly sensitive to ion temperature. The effect is verified for a mesothermal argon plasma with probe radius to Debye length ratio $0.005 < \epsilon < 0.5$ and for ion to electron temperature ratios close to unity. A scheme is developed to obtain a self-consistent measurement of the ion temperature using the basic characteristics of the finite-probe angular response after a modification of J. R. Sanmartin's theory.

A versatile ion source was constructed after a state-of-the-art electrostatic ion thruster. It provides, together with a large size vacuum chamber, a simulation facility for which the plasma stream characteristics can be tailored and the ion speed ratio easily modeled for diagnostics purposes.

A range of flow conditions and of probe parameters are investigated and the overall applicability and reliability of the method to measure T_i are assessed. Potential areas of applications are outlined.

Sommaire

Un effet de bout de longues sondes cylindriques de Langmuir a été vérifié expérimentalement pour un flux moléculaire de plasma à grande vitesse d'écoulement. L'effet observé se révèle très fortement en désaccord avec la théorie bien connue des sondes cylindriques "infinies", quand la sonde est parallèle au faisceau. La hauteur et la dimension angulaire du pic de courant ionique observé, sont toutes deux très sensibles à la température des ions. L'effet de bout a été vérifié à l'aide d'un plasma d'argon mésothermal, où les températures ionique et électronique étaient à peu près égales, et pour des rapports rayon de sonde-longueur de Debye, dénotés ϵ , allant de 0.005 à 0.5 environ. Une méthode autocritique de mesure de la température ionique, à partir des données caractéristiques de la réponse courant-angle d'attaque, a été démontrée en utilisant la théorie quelque peu modifiée de J. R. Sanmartin. Une source d'ions d'opération très flexible inspirée d'un prototype de propulseur ionique a été construite pour cette étude. L'accélérateur d'ions ainsi qu'un caisson-à-vide de grandes dimensions constituent une enceinte de simulation d'écoulements de plasma très flexible. Les caractéristiques principales ainsi que les propriétés de vitesse d'écoulement et de vitesse thermique de ceux-ci peuvent être décrites à l'aide d'un modèle simple, et modifiées à des fins expérimentales. Toute une gamme de conditions d'écoulement et de caractéristiques de sonde ont été étudiées. L'utilisation ainsi que la précision de la méthode de mesure de la température ionique ont été définies et quelques applications y sont mentionnées.

TABLE OF CONTENTS

	<u>Page</u>
Acknowledgements	ii
Abstract	iii
Sommaire	iv
Table of Contents	v
List of Symbols	vii
Introductory Comments	xii
 I. THEORETICAL CONSIDERATIONS	 1
I.1 Pertinent Theory on the End Effect	1
I.1.1 Statement of the Problem	1
I.1.2 Analytical Description	2
I.1.3 Ion Temperature Sensitivity	7
I.1.4 Range of Validity	10
I.2 Some Ion Temperature Measuring Concepts	12
I.2.1 Brief Survey	12
I.2.2 The Merits of the End Effect	13
 II. DESCRIPTION OF EXPERIMENTAL APPARATUS	 14
II.1 The Testing Facility	14
II.2 The Ion Source	15
II.2.1 Background	15
II.2.2 Gas Source	16
II.2.3 Discharge Chamber	16
II.2.4 Accelerator	16
II.2.5 Neutralizer	17
II.2.6 Operating Conditions	17
II.3 Langmuir Probes	18
II.3.1 Construction	18
II.3.2 Probe Cleaning	18
II.4 Cup Probes	19
II.4.1 Button Probes	19
II.4.2 Collimated Cups	19
II.5 Instrumentation	19
II.5.1 Ancillary Equipment	19
II.5.2 Source and Accelerator	20
II.5.3 High-Voltage Protection	20
II.5.4 Probe Circuitry	20

	<u>Page</u>
III. FLOW-FIELD CHARACTERISTICS	21
III.1 Ion Temperature Simulation	21
III.1.1 Ion Velocity Distribution	21
III.1.2 Plasma Stream Model	22
III.1.3 Verification of the Source-Flow Model	25
III.2 Pertinent Plasma Features	29
III.2.1 Background Ions	29
III.2.2 Plasma Potential	31
III.2.3 Electron Temperature	32
IV. EXPERIMENTAL RESULTS AND DISCUSSIONS	33
IV.1 Experimental Procedures	33
IV.1.1 Experimental Probe Response	33
IV.1.2 Range of Parameters	34
IV.2 Verification of the Finite-Probe Theory	35
IV.2.1 Behaviour of the Main Peak Features	35
IV.2.2 Comparison With Previous Experiments	36
IV.2.3 Self-Consistent Measurement of the Speed Ratio	37
IV.2.4 Sensitivity of the Peak Features to Speed Ratio	38
IV.3 Discussion of Experimental Results	40
IV.3.1 Verification of the Geometrical Speed Ratio Model	40
IV.3.2 Reliability of the Method to Measure the Speed Ratio	41
(a) Ion Source Effects	41
(b) Probe Bias Effects	42
(c) Probe Aspect Ratio Dependence	42
IV.3.3 Reconstruction of the Probe Response	43
IV.3.4 Non-Maxwellian Effects	45
IV.3.5 Estimate of Errors	46
CONCLUSIONS	50
REFERENCES	52
APPENDICES:	
A - MASS-FLOW MONITORING	
B - PROBE SPURIOUS EFFECTS	
C - ION BOMBARDMENT PROBE CLEANING	
D - MEASUREMENT OF ION SPEED RATIO USING SMALL FARADAY CUPS	
E - CRITERIA FOR COLLISIONLESS REGIME	
F - LENGTH AND TIME SCALES	
G - TANGENT METHODS TO MEASURE T_e	
H - PROBE STRUCTURAL EFFECTS	
I - INVERSE PROBLEM FOR LONG CYLINDRICAL PROBES	
J - STATUS OF THE MASS-MOTION EFFECT	
K - ESTIMATE OF ELECTRON TEMPERATURE	

FIGURES

List of Symbols

Roman Symbols (first occurrence or definition)

a	cylindrical sheath radius (p.1)
b	impact parameter (Fig. I-2)
c_{\max}	maximum random speed (p.24)
c_x	random speed component along x axis (p.24)
\bar{c}	Maxwellian average random speed (p.24)
c_i	Maxwellian most probable ion thermal speed (p.5)
d	cylindrical probe diameter (p.1; Fig. I-2)
e	unit electric charge
f_i	ion distribution function (p.3)
f_o	Maxwellian distribution function (p.4)
g	ionized fraction of total gas flux from accelerator (p.29)
h	ion source sheath thickness (p.26; Fig. III-2)
$j(\theta)$	ion current density with end effect as function of probe attitude (p.5)
j^*	dummy current density in analytical approach (p.5)
$j_{\infty}(\theta)$	ion current density to an infinite cylinder (p.2)
$\frac{j}{j_{\infty}}(\theta)$	normalized ion current density (p.5)
k	Boltzmann's constant
l	cylindrical probe length
m	unit electron mass
Δn	non-neutrality parameter (p.3)
n	particle number density
n_o	ion density at exit plane on axis (p.28)
r	radial coordinate

r_p	cylindrical probe radius
r_o	cylindrical source exit plane radius (p.23; Fig. III-1)
r_B	ion beam radius (Fig. III-1)
s	ion accelerating distance (p.26; Fig. III-2)
t	time
\vec{u}	ion directed-bulk-velocity (p.23; Fig. III-1)
\bar{u}	average ion directed-bulk-speed magnitude (p.1)
\vec{v}	time dependent velocity (p.21)
v_{\perp}	ion radial speed due to modified potential (p.11)
v_{\perp}^*	dummy transverse speed - analytical approach (p.4)
xyz	cartesian coordinates - 3 dimensions
$\frac{z}{r_o}$	axial distance downstream of accelerator-normalized (p.25)
z_o	distance from ion beam virtual origin to exit plane (p.28; Fig. III-1)
B	accelerator grid-hole diameter (p.26)
\mathcal{D}	ion characteristic drift length (p.9)
D_o	ion source exit diameter = $2r_o$ (p.27)
\vec{E}	electric field vector (p.3)
E	position dependent ion energy (p.21)
E_o	ion directed kinetic energy-average (p.21)
G, G'	explicit analytical functions from Ref. 22 (p.6)
I_N, I_D, I_B	currents pertinent to ion source-neutralizer, discharge and beam (Fig. II-9)
$J(\theta)$	end effect current as function of probe attitude (p.7)
$J_{\infty}(\theta)$	ion current to infinite cylinder (p.1; Fig. IV-1)

\tilde{J}	background - slow ion contribution to probe current (p.34; Fig. IV-1)
I_0	Bessel function of order zero (p.6)
K	ratio of ion current to perpendicular and parallel infinite cylinder (p.34)
L	probe length to Debye length ratio = l/Λ_D (Ref. 22)
M	ion and atomic mass
Ma	hybrid Mach number (p.5; r.h.s. of equation on p.14)
N	number density in 3-D phase space (p.21)
\tilde{O}	residual error notation (p.46)
P	neutral barometric pressure (Fig. II-9)
Q^{CT}	<u>charge-transfer</u> mechanism cross-section (p.29)
R	cylindrical probe aspect ratio = l/d (p.5)
\mathcal{R}	ion accelerator aspect ratio = D_0/s (p.27)
S_i	ion speed ratio - ratio of bulk to random speed = \bar{u}/c_i (p.5)
T_i	ion temperature
T_e	electron temperature
V_i	ion average equivalent potential (p.32)
V_p	probe to reference ground potential difference - bias (p.33)
V_f, V_s	<u>f</u> loating and <u>s</u> pace plasma measured potentials (p.31)
V_+, V_-	ion accelerator potentials - extracting grid (+) and accelerating grid (-) (p.26; Fig. II-9, Fig. III-2)
V_B, V_D	ion accelerator voltages - <u>b</u> eam, <u>d</u> ischarge (p.34; Fig. II-9)
$\Delta W, \Delta W'$	thermal energy spread of ion distributions (p.21)
X	normalized peak-shape function for end effect current (from Ref. 22; p.6)
X_0, X_1	peak-shape function truncated parts (p.6)
Z	ion charge number

Greek Symbols (first occurrence or definition)

α	electrostatic ion accelerator optical parameter (p.26)
β	ion to electron temperature ratio = T_i/T_e (p.5)
γ	ion beam divergence angle w.r.t. centre-line (p.23; Fig. III-1)
$\bar{\delta}$	dimensionless characteristic field parameter (Ref. 22) (p.4, Eq. I.9; p.12, Eq. I.39)
ϵ	probe radius to electron Debye length ratio = r_p/Λ_D (p.5)
ϵ^*	probe radius to ion characteristic drift length (p.9)
ϵ_0	permittivity constant of free space
η	dimensionless temperature sensitive parameter (Ref. 22) (p.6, Eq. I.16)
λ	mean-free-path linear dimension (p.1; App. F)
μ	complex parameter pertinent to the peak angular sensitivity to ion temperature from Ref. 22 (p.6, Eq. I.17; p.8, Eq. I.29)
ν	dummy integration variable (p.6)
σ	complex parameter pertinent to the peak amplitude sensitivity to ion temperature from Ref. 22 (p.6, Eq. I.18; p.7, Eq. I.26)
ρ_m	nondimensional radius of region effectively contributing to end effect current (p.10)
ξ	scaling parameter for peak-shape function (p.7)
ζ	azimuthal angle [cylindrical coordinates] (p.2)
π	3.141592...
τ_{ℓ}	nondimensional drift time along probe = $\ell\Omega_{pi}/\bar{u}$ (p.2, Eq. I.7)
θ	pitch angle [$\theta = 0$ probe parallel to flow] (p.2)
$\theta_{\frac{1}{2}}^{\wedge}$	peak full-width-at-half-maximum (p.7; Fig. IV-1)
$\theta_{\frac{1}{2}}$	peak full-width-at-half-maximum of current in excess of infinitely long cylinder expected value @ $\theta = 0$ (p.39; Fig. IV-1)

θ_{lim}	<u>limiting</u> angle for which analysis is valid (p.11)
ϕ	position dependent potential (p.2)
ϕ_p	potential at probe radius [$r = r_p$] (p.1)
ψ	nondimensional potential = $e\phi_p/kT_e$ (p.3)
Δ	increment or small variation of a quantity (p.46)
Γ	neutralization fraction = j_i/j_e (p.27)
Γ_+, Γ_a	ion and neutral gas flux (p.29)
Λ_D	electron Debye length = $[\epsilon_0 kT_e / e^2 n_i]^{1/2}$ (p.1)
Ω_{pi}	ion plasma frequency = $[e^2 n_i / \epsilon_0 M]^{1/2}$ (p.2)
Φ_p	nondimensional probe bias potential (p.2, Eq. I.5)

Subscripts (first occurrence or definition)

a	neutral <u>a</u> tom
e	<u>e</u> lectron
i	<u>i</u> on
l	cylindrical probe length
k	dummy index
r	radial coordinate
xyz	spatial cartesian coordinates
f	floating probe value
s	<u>s</u> pace plasma value
p	cylindrical <u>p</u> robe
B	reference to ion <u>b</u> eam
D	reference to ion source <u>d</u> ischarge
N	without slow background ions (p.48)
W	neutralizer <u>w</u> ire (p.23)
self	<u>s</u> elf-consistent scheme value (p.37)
H.S.	Hester and Sonin value
B.C.	Bettinger and Chen value

\parallel	probe parallel to flow vector ($\theta = 0$)
\perp	probe perpendicular to flow vector ($\theta = \pi/2$)
∞	reference to 'infinitely' long cylindrical probe

Miscellaneous (first occurrence)

FWHM	<u>f</u> ull- <u>w</u> idth-at- <u>h</u> alf- <u>m</u> aximum (p.8)
HWOE	<u>h</u> alf- <u>w</u> idth-at- <u>o</u> ne- <u>e</u> -fold (p.27)
H-S	<u>H</u> ester and <u>S</u> onin (p.3)
B-C	<u>B</u> ettinger and <u>C</u> hen (p.3)
F-P	<u>F</u> ournier and <u>P</u> igache (p.3)
ERF	error function standard notation (p.6)
∇	spatial derivatives - standard 3D gradient notation (p.3)
∇_v	velocity derivatives - standard 3D gradient notation (p.3)

Introductory Comments

The study of the behaviour of electrically biased metallic probes in ionized media has a considerable bearing on the simulation and on the diagnostics of space-flight environment and of laboratory plasmas of many kinds. Since the original work of Langmuir, Mott-Smith and Tonks in the mid-twenties (Refs. 1, 2) an impressive number of contributions to the literature have appeared on this subject. A prime motivation is invariably to find new analytical solutions to the fundamental problems associated with the collection of charged particles under a growing variety of conditions. In particular, the problems concerning flowing plasmas of many origins have led to the refining of numerous schemes for extracting more and more parameters directly from the characteristics of the current collection characteristics - namely, ion and electron density, electron temperature, collisional parameters, chemical and thermodynamic properties, particle distribution function and generally speaking with greater difficulty, ion temperature. These efforts have been devoted to the study of plasmas of natural sources (ionosphere, sun and stars, interplanetary space, lightning, etc.) and now more than ever to plasmas of man-made origins such as those of controlled thermonuclear fusion machines, of communication devices, those of electromagnetic propulsion devices, of laser-matter interactions and of plasma generators for large energy conversion systems.

In recent years the work of Laframboise (Ref. 3) who developed an analysis based on the related work of Bernstein and Rabinowitz (Ref. 4), has been recognized and established as a standard for two-component collisionless Maxwellian plasmas at rest; it constitutes in fact a firm basis to draw from in studies of dynamic and unsteady cases.

It has been the contention of several users of electrostatic probes, often simply called Langmuir probes, in flowing collisionless plasma streams that the flow does not significantly alter, if at all, the response of sufficiently long cylindrical probes whether the probe axis is oriented parallel or perpendicular to the flow direction (Refs. 5-13). On the basis of such arguments it is then plausible to obtain a successful interpretation of the probe response in terms of the exhaustive theories available for 'static' cases. Therefore a local observation of the main plasma parameters is available without the need for a special theory for flowing conditions. These premises have in fact enabled numerous workers to verify the 'static plasma' approach in supersonic flows with large probe radius to Debye length ratios (Refs. 14-16).

However, early experimental results reported by L. H. Brace (Ref. 16a, 1965) conducted with long cylindrical probes on-board the Explorer-17 satellite, have shown a markedly large attitude sensitivity of the current collection when the probes were nearly aligned with the satellite velocity vector. In fact a sharp ion current peak was observed about the 0° attitude whereas the so-called 'orbital limited' collection expected would have shown the slow monotonic decrease which characterizes the 'infinite' probe behaviour. Bettinger and Chen were the first to analyze these findings (Ref. 17). They explained Brace's observations in terms of an end effect of long cylindrical probes when the Debye length is large compared with the probe radius and when the flow speed is high, even though probe aspect ratios (l/d) of nearly 400 were considered.

This anomalous behaviour obviously in contradiction with the 'infinite' probe expectations was subsequently observed in a laboratory simulation of a

similar ionospheric environment by Hester and Sonin in 1969 (Refs. 18,20). They have published a qualitative assessment of this end effect based on a numerical study in order to reconcile the theory with their own observations; they also indicated a fundamental disagreement with Bettinger and Chen's explanations. Recently the work of Sanmartin (1971) has finalized the assessment of the effect in an extensive analysis (Refs. 21-23). As it was originally pointed out by Hester and Sonin the finite-probe theory unveiled a considerable interest since it affected the entire conceptual interpretation of the probe response in flowing plasmas, yet more so because the effect appeared to be sensitive to some plasma parameters under a wide range of stream conditions. In fact they alluded to the possibility of using the effect for diagnostic purposes - notably, to extract some valuable information from the strong attitude sensitivity and possibly from the ion temperature sensitivity contained in the very structure of current angular response. This last point was reiterated by Sanmartin (1972) who elaborated the foundations of a simple method to obtain the ion temperature from the ion peaks observed. Shortly after, Fournier and Pigache (Ref. 57) have published some quantitative attempts to apply Sanmartin's analytical description. More specifically they verified the end effect theory using a long cylindrical probe within a plasma stream, under simulated ionospheric conditions, and they also reported some estimates of the ion speed ratio.

The many aspects of the end effect of cylindrical probes have generated a considerable interest in the UTIAS Low Density Plasma Dynamics Group, at the onset on this research program, especially so because of the sharp attitude sensitivity it entailed. At the time, in early 1972, an experimental investigation was underway to study the exhaust characteristics of a small-scale electrostatic ion thruster. A bench prototype which was built and tested by the author in this laboratory was used to reproduce the beam characteristics of state-of-the-art ion thrusters, such as the ones proposed for station-keeping and attitude-control of synchronous satellites. The need for a very fine pointing accuracy was desirable, in particular for the study of the beam vectoring ability of flight-worthy propulsion units.

Actually the use of small ion accelerators of that type in large simulation vacuum chambers lends itself quite naturally to a number of fundamental studies involving high-speed plasma flows, such as the modelling of ionospheric sounding conditions for instance (Refs. 20,29,30). Moreover, since the end effect also showed the promising advantages of a simple diagnostic tool to measure the ion temperature in fast drifting plasmas we shifted our prime motivation and we set out to establish the basis of a systematic study of the anomalous probe response. The main research objectives which were elaborated in this respect, and which find their conclusion in the present report are summarized as follows:

1. Provide a facility to achieve collisionless-high-speed plasma conditions suitable for laboratory simulation purposes and for a variety of plasma investigations. The stream parameters should be controllable, easily monitored and systematically tailored to satisfy a wide range of experimental requirements and to allow accurate beam diagnostics (see Chapter II).
2. Verify the salient features of the end effect of cylindrical probes described in the theory proposed by J. R. Sanmartin, for a wide range of flow conditions and of probe characteristics. It is also necessary to describe and to validate the analysis of the effect using a set of nondimensional similarity parameters independent of electron temperature as opposed to the one originally

selected by Hester and Sonin. In order to complete the experimental results provided by these authors and later by Fournier and Pigache, a systematic investigation is required. In particular the reliability of the theory should be checked (Chapter I) with a drifting plasma in which the ion temperature is of the same order as the electron temperature, since only the limiting cold-ion case, $T_i/T_e \simeq 0$, has been implemented. Moreover the large-sheath regime should be studied down to values of probe radius approximately equal to electron Debye length ($r_p/\lambda_D \simeq 1$) in order to cover both weak and strong probe effects.

3. Develop a method, using Sanmartin's analysis which would demonstrate the ability of the end effect to serve as a diagnostic tool in obtaining the ion temperature by direct measurement from the probe angular response (see Chapter IV). More specifically, a flow-field model would be desirable to provide the necessary grounds for comparing the theoretical predictions with the estimates of the ion speed ratio and the ion temperature derived by direct measurement (see Chapter III).

4. Draw the appropriate conclusions concerning the range of validity of the theory and the reliability of the method to measure T_i in order to delineate some possible areas of applications.

I. THEORETICAL CONSIDERATIONS

I.1 Pertinent Theory on the End Effect

I.1.1 Statement of the Problem

The problem at hand is that of the collection of positive ions by a cylindrical probe in a high-speed, steady and collisionless plasma flow, for the regime where the sheath radius is large with respect to the probe radius. At the low densities of interest ($\lambda \gg r$) the sheath radius is basically of the same size as the electron Debye length Λ_D ; the regime which is appropriate to our problem is the one described by the hatched region in Fig. I.1. For simplicity we consider a plasma composed of a single species of singly-charged positive ions of mass M , at temperature T_i , and of electrons at temperature T_e . The flow conditions are those of a drifting mesothermal plasma ($n_e = n_i$), i.e.

$$\sqrt{\frac{kT_i}{M}} \ll \bar{u} \ll \sqrt{\frac{kT_e}{m}} \quad (\text{I.1})$$

and the probe bias ϕ_p , sufficiently negative to repel effectively all electrons, is large enough so that electron density distribution is accurately described by a Boltzmann distribution and

$$kT_e \ll |e\phi_p| \quad (\text{I.2})$$

The probe geometry is depicted in Fig. I.2 where ℓ is the probe length and d its diameter. We have the probe condition

$$\left(\frac{\Lambda_D}{r_p}\right) \gg 1 \quad (\text{I.3})$$

where the sheath radius (a) is basically given by

$$a \simeq \Lambda_D$$

Under these conditions the end effect of a cylindrical Langmuir probe is observed as a sharp increase of the ion current collected, relative to the ion current expected using the 'infinite' probe theory, when the probe is aligned with the flow. The current predicted for the 'infinitely' long cylinder under similar conditions is simply the so-called 'orbital-limited' current derived by Langmuir and Mott-Smith (Ref. 1) and which is given by

$$J_\infty(\theta) \equiv en_i \bar{u} \cdot d \cdot \ell \cdot [\sin^2\theta + \Phi_p]^{1/2} \quad (\text{I.4})$$

where in this report we choose to use a nondimensional probe bias Φ_p given by

$$\Phi_p \equiv \frac{e(\phi_p - \phi_s)}{\frac{1}{2} M \bar{u}^2} \quad (1.5)$$

i.e., we use the kinetic energy of the ion motion to nondimensionalize rather than the more conventional electron thermal energy kT_e . Therefore the current density at the parallel probe ($\theta \equiv 0$) is

$$j_\infty (\theta = 0) = \frac{en_1 \bar{u}}{\pi} \cdot \sqrt{\Phi_p} \quad (1.6)$$

The ion current to a probe of finite length in fact closely follows the 'infinite' probe description only at high angles of incidence. As the probe axis is brought into alignment with the flow a striking deviation occurs in the form of a sharp peak in the ion current, as shown in Fig. 1.3 for four arbitrary different experimental conditions.

This current peak results from the finite length of the probe, hence it is considered as an end effect. The probe is essentially infinite in terms of the flow condition if its nondimensional length, defined by τ_ℓ

$$\tau_\ell \equiv \frac{\ell}{\bar{u}} \Omega_{pi} \quad (1.7)$$

according to the work of Hester and Sonin (Ref. 18), approaches infinity. Briefly, the physical explanation of the peak is that it represents the current from those ions which enter the field of the probe through the front end of the cylindrical sheath which surrounds it, rather than through the sides as for an 'infinitely' long cylinder. With the sheath radius large compared with the probe radius and the bulk speed large compared with the ion random speed, the ion flux through the front of the sheath can be significant when the probe is aligned with the flow. However, when the probe is turned by a small angle virtually all of the ions entering the front 'scoop' have sufficient angular momentum transverse to the probe to escape the field, and hence the sharp drop in current registered toward the smaller corresponding 'infinite' probe value. It also can be seen intuitively how the end effect can be a strong function of the ion temperature, since some thermal energy may give a large fraction of the ion population entering the front of the sheath sufficient angular momentum to escape the probe, even at zero degree of incidence.

I.1.2 Analytical Description

The analysis reported in this section reproduces the relevant elements from the work of Sanmartin reported in Refs. 22 and 23. Sanmartin's approach to the problem outlined in the previous section is based on the following premises:

- (i) In order to obtain the correct description of the ion current collected by the probe, one requires to know the exact value of the electric field along the ion streamlines. However it is possible to derive an accurate expression for the electric field ($\partial\phi/\partial r$) for a limited radial region $r < r_m$ without having to solve simultaneously all three equations which in cylindrical coordinates can be written: (using r, ζ, z)

Poisson's Equation

$$\frac{1}{r} \frac{\partial}{\partial r} \left(r \frac{\partial \phi}{\partial r} \right) + \frac{1}{r^2} \left[\frac{\partial^2 \phi}{\partial \theta^2} + r^2 \frac{\partial^2 \phi}{\partial z^2} \right] = \frac{e \Delta n}{\epsilon_0}$$

Boltzmann Distribution

$$n_e = n_{e0} \exp(-\psi)$$

Vlasov's Equation (ion)

$$\frac{\partial f_i}{\partial t} + \underline{v} \cdot \nabla f_i + \left(\frac{ZeE}{M} \right) \cdot \nabla_v f_i = 0$$

where

$$\Delta n = (Zn_i - n_e)$$

and the boundary values are

$$\phi(r \rightarrow \infty) = 0; \quad \phi(r = r_p) = \phi_p$$

- (ii) Once the electric field is known at each point, the ion trajectories can be computed explicitly.
- (iii) For certain conditions relatively fulfilled for the probe potential, this steady problem can be described with satisfactory accuracy by an equivalent time-dependent problem in which time represents the flow distance along the probe measured from the tip.
- (iv) The ion current to the probe is linear in the unperturbed ion distribution function at $t = 0$ which is that of the ions just arriving at the front end of the sheath.

The extensive analytical description which we only summarize here is treated exhaustively in Ref. 23. The corner-stone of Sanmartin's arguments as described in (i) and (iii) is justified as follows. First a list of reasonable assumptions is invoked, namely, that

- the velocity of the ions parallel to the probe's axis is basically the unperturbed bulk velocity \bar{u} since $\bar{u} \gg \sqrt{2kT_i/M}$ and $e\phi_p \ll \frac{1}{2} M\bar{u}^2$,
- the front sheath effects are neglected such that the ion distribution function of the ions at $t = 0$ is a drifting Maxwellian with temperature T_i ,

- asymmetry in the sheath due to small angles of attack is neglected such that changes in the ion angular momentum and in the energy can be ignored,
- the probe is perfectly absorbing for both species, that is, the charged particles are 'annihilated' upon arrival at the probe.

Secondly, upon integrating Poisson's equation obtained from condition (i) which simply reads

$$\frac{1}{r} \frac{\partial}{\partial r} \left(r \frac{\partial \phi(t)}{\partial r} \right) \approx \frac{e \Delta n(t)}{\epsilon_0}$$

we can obtain the time-dependent electric field. If one assumes that Δn is independent of r for a small region of interest near the probe, then

$$\frac{\partial \phi(t)}{\partial r} \approx \left(\frac{r_p}{r} \right) \frac{\partial \phi(t)}{\partial r} \Big|_{r=r_p} + \frac{e \Delta n(t)}{2\epsilon_0} \left(\frac{r^2 - r_p^2}{r} \right) \quad (I.8)$$

If one defines the time-dependent field at the probe ($r=r_p$) by separating the time independent part

$$\frac{\partial \phi(t)}{\partial r} \Big|_{r=r_p} \equiv - \left(\frac{\phi_p}{r_p} \right) \cdot \delta(t) \quad (I.9)$$

and justifying the use of an average value for $\delta(t)$ and $\Delta n(t)$, $\bar{\delta}$ and $\bar{\Delta n}$ respectively (Ref. 23), within a region

$$r_p \leq r \leq r_m$$

we get

$$\frac{\partial \phi}{\partial r} \approx - \frac{\bar{\delta} \phi_p}{r} + \frac{e \bar{\Delta n}}{2\epsilon_0} \left(\frac{r^2 - r_p^2}{r} \right) \quad (I.10)$$

which is the required electric field. According to (ii) therefore, the current density $j(v_{\perp}^*)$ can be computed explicitly and since it is linear in the unperturbed Maxwellian distribution function ($z = -\infty$, $t < 0$)

$$f = f_0(v_{\perp}^*)$$

we have

$$j(t \geq 0) \equiv \int_{\text{all}} f_0(v_{\perp}^*) (j(v_{\perp}^*)) dv_{\perp}^* \quad (I.11)$$

where the * refers to the simplest form of the distribution, namely that for which all the ions have exactly the same transverse velocity v_{\perp}^* (magnitude and direction) along an arbitrary polar angle ζ . Thus the task of getting $j(t \geq 0)$, the probe current density, is reduced to that of evaluating

$$j^* = j(v_{\perp}^*)$$

i.e. using the appropriate form for f_0 , I.11 becomes

$$j(\theta) = \frac{1}{\pi} \int_0^{2\pi} d\zeta \int_0^{\infty} dv_{\perp}^* \left[\frac{v_{\perp}^*}{c_i} \exp \left\{ -\frac{1}{c_i^2} |\bar{u}_{\perp} - v_{\perp}^*|^2 \right\} j^* \right] \quad (I.12)$$

where ζ is the arbitrary angle between v_{\perp}^* and the normal to the probe and where θ is the angle between the probe and the bulk velocity \bar{u} such that

$$\bar{u}_{\perp} \equiv \bar{u} \sin \theta$$

$$c_i \equiv \sqrt{\frac{2kT_i}{M}}$$

and

$$|\bar{u}_{\perp} - v_{\perp}^*|^2 \equiv v_{\perp}^{*2} + (\bar{u} \sin \theta)^2 - 2v_{\perp}^* \bar{u} \sin \theta \cos \gamma$$

The exact analytical representation of Eq. I.12 is by no means straightforward to obtain, and was evaluated by Sanmartin in Ref. 22. Using the 'infinite' probe current value at $\theta = 0$ obtained from I.6 to nondimensionalize I.12, Sanmartin gets

$$\frac{j}{j_{\infty}} \equiv \frac{j}{j_{\infty}} (\bar{\delta}, \psi_p, \epsilon, \beta, \tau_{\ell}, Ma, \theta) \quad (I.13)$$

After a close inspection of the complete analytical expression for I.13 one can notice that the same result can be reproduced exactly by choosing to use a set of parameters more directly related to the quantities obtained in direct measurements; moreover, we find that this new set of independent parameters is not explicitly dependent on T_e . We have obtained this set which yields

$$\frac{j}{j_{\infty}} \equiv \frac{j}{j_{\infty}} (\bar{\delta}, \Phi_p, R, \tau_{\ell}, S_i, \theta) \quad (I.14)$$

This expression is equivalent to I.13, yet it exclusively involves dependences related to the probe and to ion characteristics, with the exception of $\bar{\delta}$ which is only weakly dependent on T_e . Using this appropriate conversion Sanmartin's estimate of the current to the 'finite' cylindrical probe, when subjected to the end effect, becomes

$$\frac{j}{j_{\infty}}(\theta) \equiv \frac{\pi}{2R \sqrt{\Phi_p}} \sigma^2 [X(\mu, \eta)] \quad (I.15)$$

where

$$\eta \equiv \left[\frac{2(\sigma^2 - 1)}{\ln \sigma^2} \right] \cdot \left(\frac{1}{\bar{\delta} \Phi_p s_i^2} \right) \quad (I.16)$$

$$\mu \equiv \sqrt{\frac{2(\sigma^2 - 1)}{\ln \sigma^2}} \cdot \left(\frac{\sin \theta}{\bar{\delta} \Phi_p} \right) \quad (I.17)$$

$$\sigma \cdot \text{ERF} \left(\sqrt{\ln \sigma^2} \right) \equiv 2\sqrt{\bar{\delta} \Phi_p} R \cdot \left(\pi + 0.6\tau^2 \right)^{-\frac{1}{2}} \quad (I.18)$$

We have elected to call $X(\mu, \eta)$ the peak-shape function since it exclusively describes the 'nondimensional' peak structure. The expression for the peak-shape function is given by

$$X(\mu, \eta) \equiv X_0(\mu, \eta) + \xi X_1(\mu, \eta) \quad (I.19)$$

with

$$X_0(\mu, \eta) \equiv X_0^{\mu\eta}; \quad X_1(\mu, \eta) \equiv X_1^{\mu\eta}$$

and

$$X_0^{\mu\eta} = \left(\frac{\exp(-\frac{\mu^2}{\eta})}{\eta} \right) \left\{ \int_0^1 dv \exp\left(\frac{-v}{\eta}\right) I_0\left(\frac{2\mu v^{\frac{1}{2}}}{\eta}\right) + \int_1^{\infty} dv \exp\left(\frac{-v}{\eta}\right) I_0\left(\frac{2\mu v^{\frac{1}{2}}}{\eta}\right) G(v) \right\} \quad (I.20)$$

$$X_1^{\mu\eta} = \left(\frac{\exp(-\frac{\mu^2}{\eta})}{\eta} \right) \left\{ \int_1^{\infty} dv \exp\left(\frac{-v}{\eta}\right) I_0\left(\frac{2\mu v^{\frac{1}{2}}}{\eta}\right) G'(v) \right\} \quad (I.21)$$

with

$$G(v) \equiv \frac{2}{\pi} \left[\sin^{-1} \left(\frac{1}{\sqrt{v}} \right) + \frac{\sqrt{v-1}}{v} \right]$$

$$G'(v) \equiv \frac{2}{\pi v} \left[\frac{\pi}{2} - \sin^{-1} \left(\frac{1}{\sqrt{v}} \right) - \sqrt{v-1} \right]$$

$$\xi \equiv \frac{2(\sigma^2 - 1)}{\sigma^2 \ln \sigma^2}$$

Since no general analytical solution exists for $X(\mu, \eta)$, it has to be evaluated numerically. However the trivial cases $\mu = 0$ and $\eta = 0$ yield an exact analytical form which was derived by Sanmartin (Ref. 23)

$$X(\mu = 0, \eta) = X(0, \eta) \quad (\text{I.22})$$

$$X(\mu, \eta = 0) = X(\mu, 0) \quad (\text{I.23})$$

with the following limits

$$\lim_{\eta \rightarrow 0} [X(0, \eta)] \rightarrow 1 \text{ (cold ions)} \quad (\text{I.24})$$

$$\lim_{\eta \rightarrow \infty} [X(0, \eta)] \rightarrow \left[1 - \left(\frac{\xi}{2} \right) \right] \frac{4}{\sqrt{\pi \eta}} \text{ (quasi-static)} \quad (\text{I.25})$$

I.1.3 Ion Temperature Sensitivity

The marked experimental evidence of the end effect which is exemplified with the typical traces shown in Fig. I.3, is properly described by I.13. The narrow peak region is characterized by two important peak features, namely the height of the peak given by

$$\text{height} \equiv J(\theta = 0) \equiv j_{\infty}(\theta = 0) \cdot \frac{\pi^2 d_{\perp} l}{2R\sqrt{\Phi_p}} \sigma^2 [X(\mu = 0, \eta)] \quad (\text{I.26})$$

and full-width-at-half-maximum (FWHM) defined such that

$$J \left(\theta = \left(\frac{\hat{\theta}_1}{2} \right) \right) \equiv \frac{1}{2} J(\theta = 0) \quad (\text{I.27})$$

or, in the nondimensional form

$$X(\mu = \hat{\mu}_1, \eta) \equiv \frac{1}{2} X(\mu = 0, \eta) \quad (\text{I.28})$$

such that

$$\underline{\text{FWHM}} \equiv \hat{\theta}_{\frac{1}{2}} \equiv 2 \cdot \sin^{-1} \left[\sqrt{\frac{\bar{\sigma} \Phi_p}{S_i}} \cdot \sqrt{\frac{\ln \sigma^2}{2(\sigma^2 - 1)}} \cdot \hat{\mu}_{\frac{1}{2}} \right] \quad (\text{I.29})$$

The peak-shape function $X(\mu, \eta)$ describes the current angular response by the way of the modified angle μ , and the current sensitivity to the ion temperature by way of η . The overall behaviour of $X(\mu, \eta)$ is described in Fig. I.4 for the cold-ion limit

$$\eta \rightarrow 0 \quad \text{or} \quad S_i \rightarrow \infty$$

and for three other values of η . An interesting relation can be found by observing that all the peak-shape functions merge with the cold-ion case for values of μ smaller than their half-width values $\hat{\mu}_{\frac{1}{2}}$, such that

$$X(\hat{\mu}_{\frac{1}{2}}, \eta \neq 0) = X(\hat{\mu}_{\frac{1}{2}}, \text{cold})$$

Therefore, using Eq. I.28, we have

$$X(\hat{\mu}_{\frac{1}{2}}, 0) \equiv \frac{1}{2} X(0, \eta) \quad (\text{I.30})$$

This constitutes a considerable simplification since an exact analytical expression for I.14 only exists for the two trivial cases $\mu = 0$ and $\eta = 0$. The general form of $X(\mu, \eta)$ must in fact be derived numerically.

Similarly an overall description of the peak-shape function can be given in terms of the various angular 'landmarks' which characterize the current peak. We have summarized this description in Fig. I.5.

The sharp current response obtained by the finite probe about the flow axis specifically contains the ion temperature information in both peak features. Indeed, once the physical parameters pertinent to the probe and to the ion stream are found

$$d, \ell, \bar{u}, M, n_i, \Phi_p$$

we have, from I.26 and I.29,

$$J(\theta = 0) = J(\bar{\sigma}, S_i, \Phi_p) \quad (\text{I.31})$$

$$\hat{\theta}_{\frac{1}{2}} = \hat{\theta}_{\frac{1}{2}}(\bar{\sigma}, S_i, \Phi_p) \quad (\text{I.32})$$

The sensitivity of these peak features to S_1 , the ion speed ratio, with the geometric aspect ratio as a parameter, can be developed using the master plots given in Figs. I.7 and I.8. The presentation of these plots is simplified by the fact that the nondimensional peak height is, to first approximation, directly proportional to $\bar{\delta}$ and $\sqrt{\Phi_p}$ whereas the FWHM is, to first order, independent of $\bar{\delta}$ and Φ_p .

The dependence of the end effect on S_1 can be obtained in terms of the parameter τ_ℓ , which characterizes the true finiteness of the probe in terms of the flow conditions. The nondimensional current to the parallel cylindrical probe obtained from I.26 is plotted in Fig. I.6 as a function of τ_ℓ for the range of validity

$$0 < \tau_\ell \lesssim 3$$

with ϵ^* as a parameter. This parameter describes the relative size of the probe radius in terms of a judicious ratio grouping the two nondimensional probe lengths, namely τ_ℓ and R . We get

$$\epsilon^* \equiv \frac{\sqrt{2} \tau_\ell}{2R} \quad (\text{I.33})$$

i.e.

$$\epsilon^* \equiv \frac{r_p}{\mathcal{D}} \quad (\text{I.34})$$

where

$$\mathcal{D} \equiv \sqrt{\frac{\epsilon_o \frac{1}{2} M \bar{u}^2}{e^2 n_i}} \quad (\text{I.35})$$

This last quantity is a characteristic length which is defined in the same fashion as the Debye length, only it uses the bulk ion energy instead of the electron energy since the electron Debye length is given by

$$\Lambda_D \equiv \sqrt{\frac{\epsilon_o kT_e}{e^2 n_i}}$$

Using Fig. I.7 one verifies that $J(\theta = 0)$ grows with S_1 , whereas the current peak decreases with increasing ϵ^* and therefore probe radius, under similar flow conditions. Furthermore the end effect can lead to a significant departure from the 'infinite' probe response ($J/J_\infty(0) > 10$), and more noticeably so as the non-dimensional length of the probe (τ_ℓ) is varied from small values, say 0.01 to values near unity. For values of τ_ℓ beyond 1 the effect is relatively insensitive to a change of the true probe length, that is to changes in ℓ , \bar{u} or n_i . These observations have been verified in Chapter IV where variations of n_i were accomplished by moving axially downstream of an ion source, in order to scan values of τ_ℓ smaller than 3. Beyond this point the theory reported here is not appropriate (see Fig. I.9(b)). These graphs have been prepared for arbitrary

values of $\bar{\delta}$ and Φ_p which are typical of the experimental range covered, namely 0.25 and 0.1 respectively, and for a typical flow condition for the ions yielding the scaling length $\Omega_{pi} \bar{u}^{-1}$ with a value of 0.1 cm^{-1} . Thus the current to the parallel probe can be scaled directly using a factor $\bar{\delta} \sqrt{\Phi_p}/0.25 \cdot 0.1$, whereas no adjustment is necessary on Fig. 1.8, provided these values are within a range that guarantees the validity of the analytical expressions. Considerable information is also extracted from these plots by looking at the individual performance of various probes. A series of probe aspect ratios (ℓ/d) are presented for comparison for a few standard diameters. The arrowheads simply locate the speed ratios beyond which the end effect will convey no more sensitivity to speed ratio either from the peak height or the peak width. Using Fig. 1.7 one can also obtain an idea of the performance of one probe geometry relative to another. In particular one can conclude that the smallest aspect ratio shown (i.e. 22), for example, does not lead to a significant end effect ($j/j_\infty(0) \simeq 1$) and consequently would not be a good choice as a diagnostic tool. From these plots one would conclude that a probe with the largest practical aspect ratio would perform best. However, since the interpretation of the data requires the value of the unknown quantity $\bar{\delta}$ we will show later that the comparison of the peak height and FWHM can yield a useful approximation of this value. The accurate measurement of very small angular widths then sets a practical limitation. In terms of this compromise we can conclude here that aspect ratios in the neighbourhood of 200 yield quite satisfactory results.

I.1.4 Range of Validity

In order to ascribe a limit to the validity of the scheme reported by Sanmartin one must go back to the assumption restricting the estimate of the electric field in the vicinity of the probe which was obtained in I.10. This time-dependent result was actually obtained by introducing time averages for $\bar{\delta}(t)$ and $\Delta_n(t)$ for a particular region

$$1 \leq \frac{r}{r_p} \equiv \rho \leq \frac{r_m}{r_p} \equiv \rho_m$$

Therefore if we call t_m the typical drift-time, along the probe, of ions which were at this boundary ρ_m at $t = 0$, then the estimates remain valid for the time interval

$$0 \leq t \leq t_m$$

which Sanmartin reports to be equivalent to

$$0 \leq t \lesssim 3\Omega_{pi}^{-1}$$

i.e. smaller than about three ion plasma periods. Since the drift time t is simply (steady-flow)

$$t \equiv \frac{\ell}{\bar{u}}$$

the limits to the range of validity can be expressed in terms of the nondimensional probe length τ_ℓ

$$0 \leq \tau_\ell = \left(\frac{\ell}{\bar{u}} \right) \Omega_{pi} \lesssim 3 \quad (\text{I.36})$$

Moreover as the probe is turned by an angle θ with respect to the bulk velocity direction (\bar{u}), more and more ions which would have been collected at $t < t_m$ are lost because of their increasing transverse momentum. Sanmartin demonstrates that there is a limiting angle θ_{lim} beyond which the end effect will disappear and which is given by the relation

$$\bar{u} \sin(\theta_{lim}) \simeq 2[v_\perp^2 - c_i^2]^{\frac{1}{2}}$$

where v_\perp is the radial velocity of the ion due to the 'modified' potential ($\bar{\delta}\phi_p$) i.e.

$$v_\perp \equiv \left(\frac{e \bar{\delta} \phi_p}{M} \right)^{\frac{1}{2}}$$

The limit also reads

$$\sin(\theta_{lim}) \simeq \theta_{lim} \simeq \left(\frac{2}{s_i} \right) \left[\frac{s_i^2 \bar{\delta} \phi_p}{2} - 1 \right]^{\frac{1}{2}} \quad (\text{I.37})$$

Using Sanmartin's estimate for ρ_m , which represents the region of the sheath effectively contributing to j

$$\rho_m = \frac{2R}{\tau_\ell} \sqrt{\bar{\delta} \phi_p} \quad (\text{I.38})$$

we obtain the pertinent range of validity of the end effect theory in terms of the length of the 'finite' probe and in terms of the angular span of the narrow current peak:

$$1 \leq \frac{r}{r_p} \leq \frac{2R}{\tau_\ell} \sqrt{\bar{\delta} \phi_p}$$

$$0 \leq \tau_\ell \lesssim 3$$

$$0 \leq \theta \lesssim \frac{2}{s_i} \left[\frac{s_i^2 \bar{\delta} \phi_p}{2} - 1 \right]^{\frac{1}{2}}$$

For the range $\theta_{\text{lim}} < \theta \leq \pi/2$, the probe collects the same current as if its length were part of an infinitely long cylinder or, according to I.4

$$j = j_{\infty}(\theta)$$

For probe lengths τ_{ℓ} in excess of 3 the probe current density is described accurately by Bettinger and Chen's analysis, provided the probe is parallel to \bar{u} . It is therefore important to note the considerable refinement which is brought by Sanmartin's analysis to the description of the end effect when compared with the work of Bettinger and Chen. It is reflected in the appropriate choice of an effective region of the sheath which contributes to j , instead of the whole extent of the sheath. This, we shall see, leads to the correct description of j for $\tau_{\ell} \lesssim 3$. However B-C's current at $\theta = 0$ grows indefinitely (Fig. I.9(b)). Nevertheless their result is correct for the asymptotic limit $\tau_{\ell} \rightarrow \infty$, since by definition we must have for all θ

$$\lim_{\tau_{\ell} \rightarrow \infty} \left(\frac{j}{j_{\infty}}(\theta) \right) \rightarrow 1$$

We also notice that the values of the peak half-widths disagree for $\tau_{\ell} < 3$ in Fig. I.9(a) where we show that I.32 approaches the value

$$\hat{\theta}_{\frac{1}{2}} \simeq \left(\frac{2}{S_1} \right) \text{ for } \tau_{\ell} \rightarrow \infty$$

Finally this refinement has led to the description of a modified field about the probe. This information is conveyed by $\bar{\delta}$ which is the adjusted field-scale, or characteristic field length, and which was approximated by Sanmartin:

$$\bar{\delta} \simeq \left[\ln \sqrt{\rho_m} - \frac{1}{2} \right]^{-1} \quad (\text{I.39})$$

The proper evaluation of the value of $\bar{\delta}$ has in fact proven to play a vital role in the foundations of the method to measure the ion speed ratio using the end effect. This method will be elaborated in our Chapter IV.

I.2 Some Ion Temperature Measuring Concepts

I.2.1 Brief Survey

Since this study is reporting a novel method to measure the ion temperature it was deemed necessary to give at least a schematic view of some of the various methods which were already available to probe users. However we do not intend to consider this section as an exhaustive survey of the diagnostic methods used in static or dynamic plasmas. In fact, a number of surveys have been carried out on this subject (Refs. 34-41), in particular, the most recent one conducted by Talbot et al (Ref. 33).

Most methods attempting to measure T_i were actually developed in conjunction with possible applications to the sounding of the closest natural

plasma source at hand - namely, the earth's ionosphere. Ground based schemes involving incoherent backscattering radar-sounding and spectroscopic methods have actually shown poor resolution and irregular reliability. Though in situ measuring schemes have been quite limited geographically they constitute (Refs. 34-40) the bulk of the experimental efforts attempted on-board sounding rockets, balloons, and/or satellites. Since T_i data and a fortiori comparisons between the methods are much less abundant, only a few candidates are presented here. They actually fall under three basic categories: cup analyzers, active metallic probes and stimulated interaction methods.

The cup or ion-trap analyzers have been used quite 'universally' after the theory of Whipple (1959). Though they constitute simple systems they lack the accuracy to separate multiple ion species and more so, their use is somewhat doubtful as they likely introduce serious disturbances into the plasma ahead of the probe (Ref. 41). A collimated Faraday cup system (Ref. 25) has recently been proposed as an excellent diagnostic tool to determine the ion temperature in a flowing plasma (see Appendix D), yet it represents a more refined variation of the orifice probes (kinetic-theory-probes) quite often flown on ionospheric sounding packages (Ref. 36).

Some more recent methods not developed specifically for ionospheric probing have demonstrated, at least analytically, a promising ability to obtain T_i under various plasma regimes. A hybrid design by Laframboise and Parker (Ref. 42) for orbit-limited current collection resembles in construction multi-electrode geometries studied by Medicus (Ref. 43). An AC (RF) scheme developed by Rubinstein and Laframboise (Ref. 44) to measure T_i actually presents the noteworthy advantage of being less prone to severe mechanical damage, as for instance for the diagnostics of fusion plasmas, because the probe is made repulsive for each charged species in turn and is collecting only small 'sample' currents. Another novel scheme involves probe measurements in strong magnetically confined plasmas (Ref. 45). Other studies have been undertaken to bridge the gap widened by non-collisionless flow problems: two of these T_i measuring candidates in more dense plasmas include the works by Shih and Levi (Ref. 46) and that of Chubb (MHD) (Ref. 47). Finally, the scheme reported herein, which concerns the now standard cylindrical geometry for the collisionless regime, where an anomalous end effect is brought to fruition in determining the ion temperature in a high speed plasma (Ref. 22).

As for typical proponents of the last category we can refer the reader to two methods used extensively in this laboratory for ionospheric sounding (Ref. 48). An electron-beam fluorescence probe (EBFP) is used to measure the rotational temperature of the heavy ionosphere components by analyzing the fluorescent back-scattered light stimulated locally by an electron beam. A second method is an aerospectrometer which also uses local stimulation of the neutral constituents. A nude ionization-gauge type hot filament-slit-biased collector system is made velocity selective (attitude variable) to obtain both density and speed ratio measurements of the collected species.

I.2.2 The Merits of the End Effect

It is quite noteworthy in fact to observe that direct methods to determine the ion temperature in static plasmas are inherently scarce. Furthermore there are only a few of them which are relatively successful in flow cases.

The reason for this scarceness in static plasmas is easily recognized since the region of the probe collection characteristics which is exclusively sensitive to T_i is, in most regimes, almost nonexistent. The significantly less mobile ions only produce marginal currents relative to those given by electrons unless large negative biases are used. Yet at moderately large negative biases the stable sheath which is created around the probe forces an ion to lose its autonomous temperature. In fact the ion must go through the pre-sheath region thereby accelerating, up to the hybrid speed

$$v_i \geq \sqrt{\frac{kT_e}{M}}$$

according to Bohm's criterion for a stable sheath. The current collection then becomes sensitive to electron temperature.

In flow cases the 'odds' are actually improved because the ions may already have a sufficiently large directed energy toward the sheath to satisfy Bohm's criterion, and to reach the probe. Under ideal collisionless conditions and at moderate biases they do so with basically their 'virgin' temperature. Nevertheless the sensitivity of the measuring device must allow a refinement of the measurement of T_i with a satisfactory accuracy. In most cases this last requirement inevitably calls for considerable sophistication.

The physical reason why the end effect shows a strong ion temperature sensitivity can be summarized as follows. The ions that contribute to the peak gain an easy entrance, in the thick sheath collisionless regime, through the front of the sheath when the probe is parallel to the stream. Consequently, their transverse angular momentum is largely undisturbed and since their collection strongly depends on the transverse momentum, a marked ion temperature dependence results.

The practical importance of the sensitivity of the end effect to T_i is clear. It offers a simple extension of the use of cylindrical Langmuir probes. An angular scan of the ion collection provides simultaneously the ion speed ratio and the flow direction.

II. DESCRIPTION OF EXPERIMENTAL APPARATUS

II.1 The Testing Facility

The vacuum testing facility used for the entire research program reported here is the UTIAS Low Density Plasma Tunnel (Refs. 53-54). The chamber can be operated in different pumping modes from the high mass-flows of the order of $10^4 \mu\text{l}/\text{sec}$ at pressures of the order of $10 \mu\text{Hg}$, to flows of the order of $10 \mu\text{l}/\text{sec}$ near blank-off pressure of about 5×10^{-6} torr (see Fig. II-1). The test section is about 2m in diameter and its volume is $\approx 15,000\text{l}$. The chamber was equipped with a new diffusion pump to give a higher pumping speed in the low pressure regime and LN_2 traps (1m^2 area) were used in conjunction with a pressurized LN_2 dewar filling system to minimize oil backstreaming towards the probing area and the accelerator structure. A water-cooled pyramidal trap is mounted on the centre line and can be positioned downstream to provide a collecting area for the ion beam. An angle of 30° was selected to minimize backstreaming

of ions and backsputtering of copper atoms towards the test area (Fig. II-2). A small chamber is coupled to the main chamber to enclose the entire accelerator system when it is withdrawn from the tunnel. A gate valve isolates the test chamber. An extension mechanism is used to retrieve and to extend the whole accelerator unit into the test section so the main vacuum is not broken during maintenance.

A three degree-of-freedom traverse (XYZ) coupled to position indicators allows scanning of the greater part of the test section. The flexibility of the traversing rig is greatly improved by the use of another actuator system which adds pitch ($\pm 105^\circ$) and yaw ($\pm 15^\circ$) motions. The linearity of the XYZ mechanism is within 1% and the monitor has a resolution of 1/100 of an inch. Angles can be set to within a few tenths of a degree. A special anti-backlash sprocket chain-drive mechanism is used to achieve smooth and positive motion (Fig. II-3). All actuating motors are of low voltage, synchronous type to prevent any arcing troubles, as the entire system can be engulfed in a low density plasma.

Mounting and alignment of the accelerator unit is simplified by using locating devices. A guiding rail system within the smaller chamber is completely attached to the door; the use of quick-disconnect electrical leads and a self-aligning mechanism insures trouble-free and accurate repositioning. The separately pumped chamber provides independent testing without requiring the use of the tunnel thus allowing shorter turn-around pumping times.

A testing bay (Fig. II-1) allows monitoring and operating of all functions without significant displacement. Feedthrough ports and sighting Pyrex ports also add to its flexibility. Pressure measurements are done with a Bayard-Alpert type nude ionization gauge calibrated for N_2 . A correcting factor of about 0.75 was used throughout for the reported work with argon (Refs. 55,56).

II.2 The Ion Source

II.2.1 Background

The use of ion accelerators and plasma sources in vacuum facilities of this type has been applied to various studies ranging from ionospheric simulation to plasma-flow interactions of many kinds (Refs. 19,57-59). More particularly, the type of accelerators developed in conjunction with ion propulsion technology since the mid-sixties has been a successful candidate in the majority of these cases. The ion accelerator used for this study was developed in this laboratory to serve as a bench prototype for an ion thruster program initiated in 1970-1971.

The accelerator produces a synthetic plasma of high velocity when a neutralizing electron current is injected into the positive ion beam. A schematic diagram shown in Fig. II-4 outlines the main components: the neutral gas source, the plasma source, the accelerating and beam-shaping structure and the neutralizer. The present design benefited from the various scaling relationships available from the literature (Ref. 60). Two nominal beam diameters of 2.54 and 5.08 cm were used in the experiments. The smaller diameter was obtained by masking part of the source.

II.2.2 Gas Source

The neutral gas source is controlled by a double needle-valve and the mass-flow is monitored by noting the pressure drop with time in a plenum of known volume. Various gases have been used successfully (He, N₂, Ar) with this setup. Rare gases (Ar, Xe, Ne) are of course preferred for simplicity of operation. The experiments reported here were restricted to argon because it is cheap and a wealth of background data is available. The stability of the neutral flow is excellent. The method can be very accurate and provides very low mass-flow rates down to 1.5 $\mu\text{l}/\text{sec}$ for argon. A distributor plenum is attached to the ion source just upstream of the plasma chamber to increase the homogeneity of the flow (see Appendix A).

II.2.3 Discharge Chamber

The gas enters the plasma discharge chamber evenly and is ionized by electron bombardment in a hot-cathode reflex discharge (Fig. II-7). A modest magnetic field (~ 50 Gauss) is used to improve the ionization efficiency of the hot cathode-electrons in a crossed-field configuration such that their total effective distance travelled is increased manyfold and the radial drift component minimized. The anode-cathode voltage drop is optimized to satisfy the main requirement that the discharge voltage, V_d be at least twice the value of the ionization potential (~ 15.7 eV for first ionization of argon) and is nominally set at 50 volts which corresponds to the optimum energy for argon (Ref. 79). The directly heated filament is positioned within a small cylindrical pole-piece which enhances the magnetic field near the filament to minimize electron losses to the anode. Many filament configurations were considered, namely, hairpin, coil, button, but the coiled type was preferred. A quick-access filament support with two filaments mounted at all times was used. Typical lifetimes in argon are about 30 hours (Fig. II-8) at emission densities of about 0.35 amp/cm^2 (0.008-0.010 in. tungsten and 0.007 in. tantalum). The entire internal surface of the chamber including the perforated end-plates are mirror polished to minimize heat losses. As the electron emission (Richardson-Dushman law) grows faster with temperature than pure radiative power (ideal black-body), satisfactory operation of discharges of this type normally do not require cooling of the discharge chamber walls, provided of course that the materials are carefully selected for all components. Temperatures slightly in excess of 700°K have been measured on the discharge anode structure.

II.2.4 Accelerator

The accelerating unit consists of a flat-plate electrostatic system. Two perforated match-drilled plates contain a regular pattern of holes in hexagonal symmetry (Fig. II-8). The required precision necessitated a jig production scheme. The selection of the hole sizes grid spacing and plate thickness is critical to the proper operation of the accelerator and will be dealt with under the flow-field considerations. The nominal sizes were: 1.25 mm thickness (stainless steel), 1.56 cm diameter holes and a 1.0 mm spacing. A mask with a 2.54 cm diameter opening can be inserted on the discharge side of the first grid to provide the smaller beam diameter (Fig. II-8). A proper designing of all the accelerator parts is also required for high-voltage breakdown (Paschen) protection. A small cylindrical grounded shield about twice the diameter of the accelerator,

protruding into the main vacuum chamber, was found successful in providing reduction of Paschen breakdowns. The electrical insulating materials used include Teflon, lava, Al_2O_3 , mica, mylar, Kapton, Pyrex and porcelain (ceramic) cements.

II.2.5 Neutralizer

The neutralizing scheme adopted was a directly heated filament immersed at the beam edge. Straight wires, strips and coiled wires have been tested and the latter were preferred. Early studies used a hot-filament array within the beam downstream of the source in conjunction with a screen-cage enclosing the whole beam. The method was judged too awkward since it limited access to the full test-section and precluded the probing of the entire beam envelope. The preferred neutralizer filament was mounted directly on the accelerator structure as it allowed maintenance without breaking the main chamber vacuum and provided trouble-free operation. The measured neutralizing current was usually in excess of 85% of but typically less than the emitted ion current. It is thought, as reported by other investigators that a small percentage of background electrons is injected into the positive beam from nearby ground surfaces, from secondary electron sputtering and other collision mechanisms within the beam.

II.2.6 Operating Conditions

The selection of the basic operating parameters (Figs. II-6, II-9) was made with prime concern to obtain a reliable and reproducible range of experimental conditions. The range of beam current available goes, with the nominal plate spacing, roughly from 0.6 to 12.5 mA; a standard setting of 2 mA was taken. It allowed stable operation, in conjunction with a filament current regulator, at a point minimizing neutral gas losses, allowing extended running time with minimum attention and it also provided a reference current compatible with a wide range of probe currents for beam studies. Care was also taken to operate within 'safe' boundaries with regard to excessive noise on the ion stream. The nominal discharge was operated at 50 volts (50-100 mA) with an electromagnet current of 5-6 amps. The mass-flow was typically set around 9.5 equivalent milli-amps of U.H.P. argon*.

As we shall see shortly the beam homogeneity, its stability, its symmetry along with its geometrical features in general, are of paramount importance to the study described here. The normal high-voltage configuration (Fig. II-4) was used extensively for this experiment (150-1200 eV ions). A low-voltage configuration (10-300 eV) using a single-plate extractor was also used (Fig. II-5). Some qualitative impressions can be obtained by actual beam pictures. Photographic records of beam envelopes are presented for comparison between the different modes of operation (Fig. II-10). Severe arcing is not common. However intermittent and unpredictable occurrence is usually linked to extended operation without maintenance. A shadow-shield was added to protect the insulators from neutralizer material vaporization.

An interesting feature of severely un-neutralized beams or arc-breakdown is the fanning out of the beam (180°) often accompanied by arcing at the tunnel

* 1 equivalent mA (argon) $\simeq 0.18 \mu\text{l/sec}$ or 1.5 mgm/hour.

back-plate as for the case shown in Fig. II-10(a); such occurrences only take place when the neutralizer is turned off completely, as is the case when taking photographic records, for the filament provides a natural 30 to 50 watt incandescent 'bulb'.

II.3 Langmuir Probes

II.3.1 Construction

The use of Langmuir probes in plasma studies is well documented (see Chapter I and Refs. 1-16). However, there does not seem to be a single best way for the construction and for the operational 'rules of the game' since so many various applications and requirements exist. Many practical experimental difficulties such as probe contamination are still debated. We refer to Appendix B which explicitly considers a few anomalous effects of some concern to us here. One very practical difficulty involves the construction of high aspect ratio (l/d) probes such as the ones shown in Fig. II-3. We have presented in Fig. II-11(a) a list of the various probes used in conjunction with this experimental investigation, and in Fig. II-11(b) an outline of the many experimental runs recorded with these probes, in terms of the different source parameters and probe parameters which were required. Figure II-12 shows the basic design features of the probes used for this investigation which have been standardized for ease of construction and mounting. These probes are rugged and can sustain high temperatures yet their handling and mounting requires caution, especially with the most slender ones. The mounting on the scanning rake (Fig. II-3) requires the positioning of the probe to within approximately half a diameter with respect to the centre-line. The probe dimensions are measured to within 2% of their length and 5% of their diameter.

Satisfactory straightness of the thin probes is assured by using a relatively effective straightening method which was suggested in Ref. 61. A dead weight is suspended from a length of tungsten or tantalum wire and resistive or flame-heating is used for a short length of time to provide the straightening effect. A scale is removed afterward using the electrolytic action of a NaOH cleaning solution with a 1 to 2 volts voltage difference for a few seconds. The surface is then degreased and handling is restricted. Flexures or 'kinks' of less than one diameter can be achieved with the smaller size wires (0.01 cm). However, since the natural bending of the 'cantilevered' cylindrical structure which the conducting wire constitutes can be in excess of one diameter for the long slim cases, this has been considered. Indeed, as we demonstrate in Appendix H, since the nondimensional deflection is proportional to the aspect-ratio ($R = l/d$) to the third-power, a deflection in excess of 5 diameters is expected for an ideally 'straight' horizontal wire at $R = 472$ for $d \simeq 0.01$ cm (0.004 in). This leads to an angular error at the tip of nearly 0.9° .

II.3.2 Probe Cleaning

Further probe cleaning is required after the fairly polished finish is achieved using base baths (NaOH), in order to ensure repeatable and believable probe measurements. Pure heating is insufficient and usually

impracticable at the densities involved ($n_1 \lesssim 10^8 \text{ cm}^{-3}$). Resistive heating to about 250°K for 10 minutes ($\approx 10^{-5} \text{ Kw/cm}^2$) has been reported in Ref. 62 by Pigache to be effective at densities of the order of 10^6 cm^{-3} . However, as is reported by the same author, ion-bombardment cleaning is more practical and furthermore readily available by using the ion beam from the accelerator itself. Pigache reports 2 KeV argon-ion cleaning for the same period of time to be equally effective. Though his results were for stainless steel, we estimate that for tungsten at the densities involved in this present experiment a cleaning time of ten minutes would require a 1 KeV argon current density of $80 \mu\text{A/cm}^2$ giving a heating power of $8 \times 10^{-5} \text{ kW/cm}^2$. Usually this power level was exceeded by biasing the probe by about 450 volts negative at a beam energy of 1 KeV such that 5 to 6 minutes were deemed sufficient. Indeed, a procedure of regular cleaning and keeping the probe continuously within the beam gave satisfactory results. No random current jumping or excessive slow drifting of the measurements was noted for periods in excess of 20 minutes after ion-bombardment cleaning. A simple model for probe cleaning was attempted in Appendix C.

II.4 Cup Probes

II.4.1 Button Probes

Simple flat-button probes at the bottom of insulating cups (see Figs. II-3 and II-14(b)) were constructed to measure the slow background ions present within the beam. These probes can be electrically biased. They are mounted on the same traversing-scanning rig as the cylindrical wire probes.

II.4.2 Collimated Cups

The schematic of a collimated Faraday cup given in Fig. A-2 shows the orifice geometry selected to sight the smallest area possible at the accelerator exit-plane for beamlet*resolution, yet large enough to yield a reasonable current level, typically of 1 n amp. To keep the dimensions small a compromise was arrived at of a 1.75° full-angle aperture. The orifice size is 0.08 cm and the second orifice can be biased to provide a repelling potential for the secondary electrons originating from the collimator. The collector was normally set floating and the 'grid' biased at -9 volts. An adapter is used to mount the miniature cup on the standard rake. The cups have been used to define the beam edge and to study the spreading of the beam. It also provides an interesting diagnostic method to determine the local flow velocity direction and possibly the ion speed ratio (see Chapter III, Section III.1.3 and Appendix D).

II.5 Instrumentation

II.5.1 Ancillary Equipment

The operation of the pumping facility is accomplished by a fully interlocked fail-safe control system. The XYZ traversing mechanism can be operated using a hand-held multi-function control box. The scanning mechanism (Fig. II-13(b)) provides both digital and analogue signals to be monitored at an X-Y recorder.

*see Figs. III-1 and III-2.

II.5.2 Source and Accelerator

A table shown in Fig. II-9 gives the basic requirements for the operation of the accelerator. The basic feature for the extended stable operation of the plasma source is the beam current regulating system based on a very reliable design used by the UTIAS Rocket Group for their flight-proved electron guns, in which the discharge filament current is controlled to keep the beam current constant. The circuit is protected from high-voltage (Fig. II-13(a)) surges and is current limited. The filament current is provided by a floating 12 volt automotive battery and beam current regulation can be achieved over a voltage range of about 120 volts to 1800 volts at 2 mA ion emission for extended periods (> 3 hours). A schematic diagram (Fig. II-15) describes the initial (warm-up) operation of the source before the beam is turned on. It simply involves running the regulator with an external 'dummy' calibrated current to allow the discharge to stabilize before the high-voltage is turned on.

II.5.3 High-Voltage Protection

Safe operation with positive high-voltage on the discharge supplies is allowed by the use of plexiglass to insulate the supplies and their controls and by the use of a 1-to-1 10 KV line isolating transformer. A commercial regulated power supply used for the discharge required extra care since an arc-over to ground from the positive high-voltage supply would put a transient voltage spike on its output stage and destroy it. The integrity of this supply was preserved during the whole extent of this study by the use of a simple and inexpensive surge-limiter circuit (Fig. II-16). A bank of gas-filled surge limiters ($V \approx 70$ -90 volts) is also put across the output terminals to limit any surges beyond the typical operating level (50 volt) with a response of better than 5 KV/ μ sec.

II.5.4 Probe Circuitry

The single-Langmuir probe circuit is a standard balanced bridge design (Fig. II-17) with a slow manual voltage sweep (X-axis). The measuring leg (Y-axis) is recording better than 99% of the probe current signal at 10 K Ω . This circuit, however, contains an important refinement in practice to provide the ability to re-trim the bridge frequently when low currents are obtained (typically $\lesssim 10^{-6}$ amp). Indeed, as the input impedance of the Y preamp on the chart recorder can vary slightly with scale factor and since large bias voltages are utilized, small imbalances can then be readily corrected to avoid significant offset errors. The frequency response of this entire circuit is limited at 1 KHz. A 5 μ F capacitor across the Y-axis terminals of the recorder was occasionally necessary to reduce noise at low levels.

For measurements at constant voltage a sensitive current-to-voltage converter was preferred. It allowed the measurement of currents of 10^{-9} to 10^{-3} Amp at 1 volt full-scale output with negligible drift for extended periods. The circuit response is kept below 100 Hz (typically 30 Hz) to minimize high-frequency noise when used in conjunction with the probe pitch and yaw scans (Fig. II-14(a)). This frequency response is quite sufficient to monitor the signals since the $\pm 105^\circ$ scanning is accomplished in a relatively long period - typically a few seconds.

Standard current and voltage monitoring meters are used with accuracies of better than 3% full-scale, throughout. The XY recorder is a series 7001A Hewlett-Packard (metric) unit and the re-calibration procedures were performed regularly.

III. FLOW-FIELD CHARACTERISTICS

III.1 Ion Temperature Simulation

III.1.1 Ion Velocity Distribution

The correct simulation of an ideal thermal-ion stream with drifting velocity (bulk velocity) \bar{u} relative to some object to be tested requires that the flow be described, in the drifting frame of reference, by a standard Maxwellian distribution function giving the phase-space density

$$d^3N_{v_x v_y v_z} = N \left(\frac{M}{2\pi kT_i} \right)^{3/2} \exp \left[- \frac{M}{2kT_i} (v_x^2 + v_y^2 + v_z^2) \right] dv_x dv_y dv_z \quad (\text{III.1})$$

In the laboratory reference system (primed) therefore, we can express the resulting velocity

$$v'_z = \bar{u} + v_z \quad (\text{III.2})$$

such that the 'longitudinal' thermalized population can be described by

$$dN_{v'_z} = N \left(\frac{M}{2kT_i} \right)^{1/2} \exp \left[- \frac{M}{2kT_i} (v'_z - \bar{u})^2 \right] dv'_z \quad (\text{III.3})$$

or using the energy relation $E_0 \equiv 1/2 M\bar{u}^2$ and $E'_z = 1/2 Mv'^2_z$

$$dN_{E'_z} = N \left(\frac{M}{2\pi kT_i} \right)^{1/2} \exp \left[\frac{1}{kT_i} \left\{ (E'_z)^{1/2} - (E_0)^{1/2} \right\}^2 \right] \frac{dE'_z}{(2ME'_z)^{1/2}} \quad (\text{III.4})$$

This longitudinal distribution is characterized by a thermal energy spread which is roughly described by the points at which

$$(E'_z)^{1/2} - (E_0)^{1/2} \equiv (kT_i)^{1/2} \quad (\text{III.5})$$

If we assume that $E_0 \gg kT_i$, i.e. since $S_i \gg 1$, then we obtain an approximation for this full width between the $(1/e)$ points ($e \equiv \exp[0.1]$)

$$\Delta W'_L \equiv 2 |E'_z - E_0| \quad (\text{III.6})$$

or

$$\Delta W'_l \simeq \Delta W \cdot 2 \sqrt{\frac{E_o}{kT_i}} \quad (\text{III.7})$$

where ΔW is the natural width of the distribution in the fixed laboratory frame ($2kT_i$).

The perfect simulation of the ion temperature for the transverse component however is simplified since there is no dependence on the translation motion. Thus it implies that

$$dN_{v_r} \equiv dN_{v'_r} = N \left(\frac{M}{kT_i} \right) v_r \exp \left[- \frac{M v_r^2}{2kT_i} \right] dv_r \quad (\text{III.8})$$

$$dN_{E_r} = \frac{N}{kT_i} \exp \left[- \frac{E_r}{kT_i} \right] dE_r \quad (\text{III.9})$$

and a full width identical to the natural energy spread

$$\Delta W'_t = \Delta W \equiv 2kT_i \quad (\text{III.10})$$

Therefore the longitudinal simulation requires a considerably broader energy width than the transverse case since in most applications $E_o \gg kT_i$ in Eq. (III.7). For instance, to simulate the correct motion of a vehicle at satellite velocity (~ 10 km/sec) through a nitrogen plasma at about 1200°K (0.1 eV) the N_2^+ stream in the test tunnel should show an energy width of nearly 5 eV centred about a main energy of 15 eV for the longitudinal component, and a width of only 0.2 eV for the transverse thermal component.

III.1.2 Plasma Stream Model

The relative motion between a probe and the ions and electrons of a streaming plasma is the result of the directed, or bulk velocity, and the thermal velocity of the particles as we have seen above. More specifically the plasmas of interest to this report satisfy the mesothermal condition

$$\langle v_e \rangle \gg \bar{u} \gg \langle v_i \rangle \quad (\text{III.11})$$

which applies to a great number of natural and laboratory plasmas and in particular to the ionosphere. It indicates that the relative velocity between the probe and the ions is essentially \bar{u} with a small random thermal component $\langle v_i \rangle$ added to it whereas the probe-electron relative velocity is totally randomized in direction and has a magnitude given by $\langle v_e \rangle$. This also means that, in order to achieve an accurate simulation, the small random velocities represent a refinement which may be omitted in many cases, yet it cannot be disregarded in the study of the beam

structure or, as is the case here, in the description of a probe effect which is very sensitive to exactly this transverse random velocity component.

However, the particular difficulties associated with the generation of an extended plasma beam with ideal Maxwellian features, at drifting velocities approaching satellite values, are such that a situation short of the ideal has to be accepted for experimental purposes.

The beam produced by an electron-bombardment-type ion thruster (Chapter II) actually meets most of the requirements of simplicity in that respect, and the distribution function can be modelled satisfactorily in most aspects. The electrons of the well defined plasma stream are essentially totally randomized at a temperature close to the neutralizing wire temperature (see Section III.2.2)

$$\langle v_e \rangle \simeq T_W \simeq \frac{1}{3} \text{ eV}$$

A significant part of the longitudinal ion energy spread comes from the fact that the ions are extracted non-ideally through a complex sheath geometry in a region of the accelerator where large potential gradients exist. Furthermore, this spread is affected by a complex interaction or cross-coupling between the mass-flow and the source discharge characteristics. It can be estimated (Ref. 28) that this longitudinal spread is typically less than about 5% of the main accelerator voltage or about ± 10 eV for an accelerator potential of 500 volts. According to Eq. III.7 this would be just about sufficient to properly simulate an ion temperature of 0.1 eV at a beam energy of 500 eV (e.g. 50 km/sec argon). However no attempt was made to purposely tailor this longitudinal spread, as it is expected to be of little consequence in this investigation, where only the transverse spread is of paramount importance.

An exact description of the physical mechanisms involved in the generation of the natural transverse energy spread of this same beam is considerably complex.

The main beam can be depicted by a superposition of a series of small discrete beamlets extracted by each individual circular aperture as shown in Fig. III-2. The small beamlets are expanding with a limiting divergence angle 2γ and are merging smoothly into a well defined beam which is contained within an angle 2γ .

The ion contribution to a point on axis at large distances downstream is defined in Fig. III-1 for a circular aperture Δs_k located at the maximum source radius r_0 . The transverse component of the velocity, for an ion released from Δs_k and collected at an axial distance z is given by

$$v_{k\perp} = u_k \sin\theta \quad (\text{III.12})$$

provided one assumes collisionless and field-free conditions within the beam. The very nature of a cylindrically symmetric source of finite extent actually provides a maximum transverse velocity component for an ion arriving at a position $(z,0)$ under these conditions, namely

$$v_{\perp \text{ max}} \simeq \text{Min}[\bar{u}\sin\theta, \bar{u}\sin\gamma] \quad (\text{III.13})$$

where \bar{u} is some average directed velocity for the ions.

It is also reasonable to assume that every one of the closely packed apertures contributes to the main beam as a separate source and that since only small angles are involved, one can expect that an ion collected at a large axial distance (in terms of the source radius r_0) can originate from the separate source with an equal probability. We can also assume that the velocity distribution from each beamlet will be zero beyond the maximum value given by III.13. Therefore, following Hester and Sonin (Ref. 18) we can represent the distribution for the magnitude for the transverse velocity in the x-direction (by analogy the same treatment holds for the y-direction) by

$$f(c_x)dc_x = \frac{2}{\pi} \left(1 - \left(\frac{c_x}{c_{\max}} \right)^2 \right) d \left(\frac{c_x}{c_{\max}} \right) \quad (\text{III.14})$$

To relate this to an equivalent Maxwellian, we make the observation that the average magnitude of a velocity component equals half the mean random speed, i.e.

$$\overline{c_x} = \frac{1}{2} \bar{c}$$

therefore calling this average transverse velocity $\langle v_{\perp} \rangle$ we have

$$\bar{c} = \langle v_{\perp} \rangle = 2 \overline{c_x}$$

and

$$c_{\max} = v_{\perp \max}$$

where

$$v_{\perp \max} = \bar{u} \frac{r_0}{(r_0^2 + z^2)^{1/2}} \approx \bar{u} \frac{r_0}{z}$$

We get the average transverse velocity of the ions arriving at z

$$\langle v_{\perp} \rangle \approx \frac{8}{3\pi} \left(\frac{r_0}{z} \right) \bar{u} \quad (\text{III.16})$$

An effective ion temperature is then defined assuming that a synthetic thermalization of the ion population is satisfactorily achieved. The Maxwellian average is then equaled to the average found

$$\bar{c}_i \equiv \sqrt{\frac{2kT_{i\perp}}{M}} = \langle v_r \rangle$$

which yields

$$T_{i\perp} \approx \frac{32M}{9k\pi^2} \cdot \left(\frac{r_o}{z} \bar{u} \right)^2 \quad (\text{III.17})$$

Similarly a synthetic ion speed ratio is defined using the geometrical model with the expression

$$S_{i\text{geo}} \equiv \frac{\bar{u}}{\bar{c}_i} = \frac{3\pi}{8} \left(\frac{z}{r_o} \right) \quad (\text{III.18})$$

For example, a 1 KeV singly-ionized argon beam would simulate a speed ratio of about 80 at an axial distance $z/r_o \approx 40$. An ion temperature of about 0.5 eV would be simulated in the transverse plane according to III.17.

III.1.3 Verification of the Source-Flow Model

In order to summarize the assumptions underlying the beam model, they can be listed briefly as follows:

1. The flow conditions satisfy the collisionless criteria (see Fig. I-1 and Appendix E).
2. The charged species are streaming in field-free space away from the extractor, assuming that no residual fields are present and that neutralization is complete.
3. The beam density is approximated using a conical expansion model with a divergence angle γ and falls off roughly as the inverse of the axial distance $(z/r_o)^{-2}$.
4. The geometrical centre-line is preserved throughout (no misalignment and/or vectoring) such that the current density and the divergence at any given radius from the centre-line are axially symmetrical.
5. The angular density at a given radius from the centre-line is symmetrical around a contributing solid angle $\sin\theta d\theta$.
6. The area contributing to the probe current is large enough to average out single-hole effects.
7. The test area at the probe is small enough that changes in current density across it average out to a value representative of the value at the centre.

The conditions to validate the first assumption is chosen by design since the collisionless flow conditions are pertinent to this study. These conditions satisfy the criteria discussed in our Appendix E. The restrictions listed under numbers 4 to 7 follow from the symmetry and from the physical dimensions of the source relative to the probe. They are for all intents and purposes straightforward. Assumptions 2 and 3, however, imply a considerable combination of physical mechanisms; they are the ones we intend to discuss more specifically in this section.

An ideal description of the beam structure is depicted in Fig. III-2. The formation of the beam involves the interaction of the large field gradients responsible for the electrostatic lens action of the apertures, along with the space-charge spreading of the ion beamlets which are shaped and extracted by these fields in the immediate vicinity of the grids. Further away, the ion beam is neutralized by a colony of thermal electrons emitted by an incandescent wire in a region where residual fields within the beam are small.

The divergence angle γ can be approximated by the simplified model of Davisson-Calwick (Ref. 77) for a pair of circular grids of diameter B , and where h and s are the sheath thickness and the acceleration distance, respectively

$$\gamma \approx \theta_h - \tan^{-1} \left[\frac{B}{2} \cdot \left(\frac{\frac{2\alpha-1}{\alpha} \cdot \frac{h}{s} + \frac{4}{3}}{2h} \right) \right] \quad (\text{III.19})$$

The angle θ_h is the angle at which the ions are assumed to be released from the sheath, with basically zero energy. The parameter α represents an important ratio which sets the optical property of the lens in terms of the value of the voltages V_+ and V_- on each grid

$$\alpha \equiv \frac{V_+}{V_+ + |V_-|}$$

Typically we have

$$B \approx \frac{s}{2}$$

$$\alpha \approx 0.7$$

$$\gamma \approx 10^\circ - 14^\circ$$

which implies a value of $h/s \approx 0.04$ if we assume a plane sheath ($\theta_h = 0^\circ$). Using some nominal source estimates of the Debye length from values for the electron temperature and density within the source ($T_e \sim 3$ eV and $n_i \approx 10^{10} \text{ cm}^{-3}$) we obtain a value of $h/s \approx 0.03$ for $s \approx 4$ mm. This result suggests that the divergence model is reasonably accurate.

In general, the real beam shape only approximates the beam geometry described in Fig. III-2. For instance, Fig. II-10(e),(f) shows that the beam edge is not truly conical. In fact the beam waist is slightly constricted near the grids and gradually expands. This is resulting from the convergent-divergent action of the two metal grids and of a virtual electrode situated near the neutralizing point. Only a marginal space-charge effect is believed to be present beyond that point because of imperfect neutralization. This can be demonstrated using a fairly accurate model for the space-charge spreading of an ideal parallel ion beam. The variable of interest is a product of the beam aspect ratio \mathcal{R} ,

D_0/s the ratio of source diameter and acceleration distance, and the neutralization fraction Γ (Ref. 69)

$$R \sqrt{1 - \Gamma} \quad (\text{III.20})$$

Typically, since $R \simeq 20$ and the measured divergence angle γ is roughly $10^\circ - 14^\circ$, as indicated in Fig. III-3, the corresponding neutralization would be about 99.8% complete if it alone were to account for this divergence. This is of course beyond our measuring accuracy; nevertheless it makes it plausible that the actual curvature of the beam, as it leaves the accelerator, is caused by these straightforward mechanisms.

The true shape of the beam envelope and of the ion streamlines can be revealed by inspecting a set of radial density profiles scanned at various axial positions. Such radial scans have been obtained using cylindrical probes as shown on Fig. III-4, and also using small collimated Faraday cups as reproduced from experimental traces in Fig. III-5. Only marginal misalignments of the source with respect to the tunnel centre-line are observed, as indicated in Fig. III-4, and are typically less than 1.5° . The slight distortions which could have been introduced on the radial profiles by keeping the probes parallel to the centre-line, rather than following an arc to preserve the true distance from the source, are not believed to be significant because of the small corrections involved. The small envelope irregularities are more easily observed with the Faraday cups as shown in Fig. III-5 and are more pronounced at the extreme edge of the beam.* One can use these profiles to obtain an idea of the departure of the ion streamlines from the straight lines assumed by the conical model. This is accomplished by taking the width of the profile at one e-fold from its maximum ($\sim 37\%$) since the beam structure is found to have the familiar bell-shape feature of a Gaussian model. The widths are obtained directly from the normalized ion density profiles which are measured experimentally, as depicted in Fig. III-6. The various radial positions are normalized with the corresponding ideal source-flow values of the beam radius r_B at an axial position z , that is

$$r_B \equiv r_0 + z \tan \gamma \quad (\text{III.21})$$

The half-width-at-one-e-fold (HWOE) measurements can be plotted against the non-dimensional position z/r_0 for a number of beam conditions as shown in Fig. III-7. The results clearly indicate the gradual bending of the ion streamlines up to axial distances of the order of 30 for the large beam diameter, and of roughly $z/r_0 \simeq 60$ in the case of the small beam diameter. The expansions become basically straight or conical beyond these points and follow closely the measured spreading angles γ in each case. The fact that the various beam conditions do not lead to a unique result, as would be expected, required some explanation. This fact was already observed in the normalized profiles presented in Fig. II-6 where the two solid curves represent an attempt to average the three z/r_0 cases for both the small and the large beam diameter configurations. The answer to this observation rests in the experimental traces themselves. The small beam exit diameter will generally lead to relatively flatter profiles because the beam feeds from a smaller,

*These anomalies could be responsible for a somewhat irregular probe behaviour reported in Section IV.4.2.

more uniform portion of the discharge. The plasma density is also considerably smaller and it is therefore more difficult to extract the signal from the traces, as indicated by the larger spread of the solid symbols in Fig. III-6, especially for the larger axial distances where the signal level is lowest. Furthermore, a small background contribution of slow ions has not been subtracted from these traces; it constitutes a relatively larger contribution to the lower signal. Finally, a further contribution to the deviation can be due to the fact that the density profiles are not perfectly similar in shape. Here we have treated them as ideal Gaussians, according to the standard representation

$$n(r) = n(o) \exp \left[- \left(\frac{r}{r_B} \right)^2 \right] \quad (\text{III.22})$$

A final check of the beam density model is provided by a series of axial scans obtained with a group of cylindrical probes perpendicular to the flow at roughly the same beam energy. The density was measured using the perpendicular probe relation obtained in Chapter I

$$J \left(\frac{\pi}{2} \right) \equiv en_i \cdot d \ell \cdot \sqrt{1 + \Phi_p} \quad (\text{III.23})$$

where Φ_p is the nondimensional probe bias and after the contribution of the slow ions is subtracted from the measured current according to a method outlined in Section IV.1.1. The results are presented in Fig. III-8 where n_i is plotted against z/r_o and is normalized with respect to the value at $z/r_o = 20$ and 40 for the large and the small beam diameter cases, respectively. The conical model lines which satisfy the ideal source-flow relation

$$n_i = n_o \left(\frac{z_o}{z + z_o} \right)^{-2} \sim \left(\frac{z}{r_o} \right)^{-2} \quad (\text{III.24})$$

are drawn to provide a direct comparison. The trend indicated corroborates the previous experimental observations, namely that the ion streamlines bend slightly outward. This suggests the existence of an axial beam density fall-off which should be slightly faster than $(z/r_o)^{-2}$ at the larger distances, as indicated in Fig. III-8.

In summary then, we have observed that the ideal source-flow model is somewhat distorted due to the slight curvature of the ion streamlines within the beam envelope. This is also reflected by an ion density which decreases slightly faster than $(z/r_o)^{-2}$ at large axial distances. The immediate consequences for the geometrical model used to describe the simulation of the transverse temperature are difficult to delineate quantitatively. However, since $S_{i_{\text{geo}}}$ is intimately related to the assumed model for the beam formation and depends on γ , \bar{u} , z/r_o and θ according to Eq. III.13 and Eq. III-16, we can expect that the speed ratio simulated will be somewhat perturbed by any significant modification of the actual values of γ and \bar{u} . For instance, the value of the divergence angle γ is decreased at small z/r_o because of the existence of a beam waist. Therefore the limiting transverse velocity defined by III.13 could be decreased at some z/r_o , thus the synthetic speed ratio would consequently increase. Finally, at large z/r_o , larger transverse velocities are expected because the ion streamlines are

curved outward. This effect would lead to speed ratios slightly overestimated by the ideal conical expansion, as discussed in Chapter IV, Section IV.3.1.

III.2 Pertinent Plasma Features

III.2.1 Background Ions

The high-energy ions constitute a fraction g of the total gas flux from the accelerator. The remaining portion comes from the non-ionized neutral parent-gas such that

$$g \equiv \frac{\Gamma_+}{\Gamma_{\text{tot}}} = \frac{\Gamma_+}{\Gamma_+ + \Gamma_a} \quad (\text{III.25})$$

where the neutral flux is roughly given by the one-dimensional Maxwellian gas relation

$$\Gamma_a \propto \sqrt{\frac{kT_{\text{anode}}}{2\pi M}} \quad (\text{III.26})$$

and

$$\Gamma_+ \equiv \frac{j_+}{e} \simeq n_i \bar{u} \quad (\text{III.27})$$

A background of slow ions is produced by the charge-transfer mechanism schematically represented by the relation



This mechanism is responsible, in the low-density plasma facilities of large dimensions, for the creation of an annoying fraction of slow randomized ions whereby an energetic ion loses its charge to a slow neutral atom, indicated by the symbol $\tilde{\cdot}$, following a rate process governed by a cross-section Q_{cT} such that

$$\frac{\tilde{n}_i}{n_i} = 1 - \exp[-Q_{cT} n_a z] \simeq Q_{cT} n_a z \quad (\text{III.29})$$

The axial distance travelled z can be significant for extended test-sections. Thus, many authors (Refs. 19,24,30) have reported relative values for slow-ion densities

$$0 \lesssim \frac{\tilde{n}_i}{n_i} \lesssim 20\%$$

for facilities using an ion accelerator similar to the one used here. Using a method obtained from the work of Clayden and Hurdle (Ref. 29) we have monitored

the slow-ion contribution within the beam using small flat cups (Section II.4). These measurements have shown that the maximum relative slow-ion density within the beam favours the higher figure reported above, when the small cups were looking back on axis within the beam, whereas we get

$$\frac{\tilde{n}_i}{n_i} < 15\%$$

with the cups looking across the beam. The measured values also indicate that the relative background density scales roughly as

$$\frac{\tilde{n}_i}{n_i} \propto \bar{u}$$

and

$$\frac{\tilde{n}_i}{n_i} \propto \left(\frac{z}{r_o} \right)^{-1}$$

which agrees with the first order estimate obtained from Eqs. III.23, 25, 27 and the conical density relation given in III.24, i.e.

$$\frac{\tilde{n}_i}{n_i} \propto Q_{cT} \left(\frac{1-g}{g} \right) \bar{u} \left(\frac{z}{r_o} \right)^{-1} \quad (\text{III.30})$$

since Q_{cT} is not varying much (Ref. 72).

In order to evaluate the importance of the slow-ions which introduce an offset current independent of probe orientation on our probe traces (Fig. IV-1) we have obtained a background pressure dependence by introducing a controlled back-fill of neutral argon in the test chamber. This was judged preferable rather than feeding the gas through the ion source, as it should be, so that the operating conditions of the accelerator would not be altered. Typical results are presented in Fig. III-9 where the background flow ion current is displayed in arbitrary units. If we assume quite reasonably that only a marginal partial pressure of foreign gases is present in the test section during normal operation, we can see that, according to the ideal gas law and to Eq. III.29 we should have

$$\frac{\tilde{n}_i}{n_i} \propto n_a \propto P$$

where P is the background pressure. This is verified in Fig. III-9 except for values of test section pressures near 8×10^{-5} torr beyond which back-ingestion into the source produces severe beam instability. By directly extrapolating this linear region we estimate that the residual slow-ion contribution would become negligible at about 8×10^{-6} torr which is somewhat lower than our minimum operating point.

The background ion current is superposed on any measurement obtained by the cylindrical probes. This very fact has led us to use another simple method to estimate the operating pressure at which the stray contribution of randomized slow ions would be negligible. This is done by looking at the current collected by the perpendicular probes ($\theta = \pi/2$). The absolute current to the probe in the ideal situation, that is without any slow ions, is given by the following relation obtained from I.7

$$J_{\infty} \left(\frac{\pi}{2}, \Phi_p \right) \equiv J_{\infty} \left(\frac{\pi}{2}, 0 \right) \cdot (1 + \Phi_p)^{\frac{1}{2}}$$

where

$$J_{\infty} \left(\frac{\pi}{2}, \Phi_p = 0 \right) = en_i \bar{u} \cdot d \cdot l$$

Therefore, by plotting the ratio of the measured value and the one given above versus background pressure, one obtains an estimate of the spurious contribution. A group of 5 experimental cases are presented in Fig. III-10 for 2 probes, at about the same beam energy value and for three axial positions. The pressure excursion was achieved as before using a backfill of neutral argon. A simple extrapolation yields about 1×10^{-5} torr for the pressure for negligible slow ion contributions which is quite close to the pressure estimated with III.30. By inspection we can then verify that the relative importance of the stray contribution does not exceed 20% at the typical operating conditions.

III.2.2 Plasma Potential

Clayden (Ref. 29) has obtained the dynamic equivalent to Chen's 'static' relation for the estimate of the floating potential in a plasma (Ref. 73). These relations yield basically identical results for a dynamic plasma with $T_e \sim 1/3$ eV and with a directed ion energy of 500 eV, that is

$$\text{(Chen-static)} \quad \phi_f = V_f - V_s = T_e \ln \left(\frac{\pi m}{2M} \right)^{\frac{1}{2}} \simeq -1.9V \quad (\text{III.31})$$

$$\text{(Clayden)} \quad \phi_f = V_f - V_s = T_e \ln \left(\frac{8\bar{u}}{\pi \bar{c}_e} \right) \simeq -1.5V \quad (\text{III.32})$$

where

$$\bar{c}_e = \langle v_e \rangle = \sqrt{\frac{8kT_e}{\pi m}}$$

This has led us to consider the value of V_f measured with respect to reference ground as an approximated value of the local plasma potential, since V_f is typically close to 50 volts. Therefore, with an accuracy of about 2%, one can obtain the nondimensional probe bias

$$\Phi_p \equiv \frac{\phi_p - \phi_s}{\frac{1}{2} M \bar{u}^2}$$

by using the following approximations

$$\phi_p - \phi_s \simeq \phi_p - \phi_f$$

and

$$\frac{1}{2} m u^2 \equiv e V_i \equiv e(V_B - V_s) \simeq e(V_+ + V_D - V_f)$$

We measure V_f by taking the reading of the bias at which the probe collects no current when placed within the plasma. The characteristic values of the floating potential are shown in Fig. III-11 as a function of beam energy, for number of probes. The relatively large values of floating potential (with respect to reference ground) which are achieved are typical for the operation of ion accelerators of this type when the neutralizer wire is withdrawn from the beam (Ref. 65). In fact, in these experiments the neutralizer was placed outside the nominal beam diameter. In the low-voltage configuration, indicated by solid circles in the figure, the beam fans out prohibitively at the lower beam-forming voltages. This has basically the same effect as that of re-inserting the neutralizer within the beam thereby decreasing the coupling voltage between it (or reference ground) and the plasma.

III.2.3 Electron Temperature

Although the absolute value of the electron temperature is not used specifically in the analysis of the probe response which is pertinent to this report, an order of magnitude estimate of that value was judged essential to have a 'complete' picture of the plasma. Three different probe geometries were used. Basically all three methods were applied while assuming static conditions. The standard procedures obtained from the literature were followed for the single-probe, the loop-probe and for the double-probe - namely, using the slope of a semi-log plot of current versus voltage (Refs. 5,36,73). An approximated tangent method described in Appendix E was also used. Although no attempt is made in order to favour one method over another, one can say that the loop has the distinctive advantage of being the only self-cleaning (ohmic) candidate of interest. A table shown in Fig. III-12 summarizes the various results which are presented in Fig. III-13. Only a marginal dependence on axial position is detected by all probes. The results are basically independent of probe position (perpendicular or parallel). The loop-probe results are slightly higher than the neutralizer wire temperature

$$T_e (\text{loop}) \simeq 0.35 \text{ eV}$$

$$T_w \simeq 0.27 \text{ eV}$$

The loop geometry is judged more compatible with the 'static' plasma approach as the cylindrical single-probe features are more liable to be distorted by dynamic effects, such as the end effect outlined in this report (see Appendix J). The

results obtained with the single-probe are systematically about 100% higher than T_e (loop). The approximation scheme mentioned in Fig. III-13 refers to a description reported in Appendix K. At any rate, a value of about 1/3 eV is taken as representative of the electron temperature for the standard beam conditions reported here.

IV. EXPERIMENTAL RESULTS AND DISCUSSIONS

IV.1 Experimental Procedures

IV.1.1 Experimental Probe Response

After regular and systematic probe cleaning (see Ch. II.3, Appendix C) the cylindrical probes were positioned by adjusting the X and Y coordinates until a peak reading of the ion current was achieved with the probe parallel to the flow geometric centre-line. The sensitive pitch and yaw adjustment actuators were then used to further optimize the peak. This procedure effectively yielded the local direction of the ion velocity because of the probe attitude sensitivity, and at this point the recording of the various flow and probe parameters was initiated.

The salient features of the ion current versus pitch-angle curve are exemplified in Fig. IV-1. The solid line represents the actual finite probe current response for values of θ from 0° to 90° . As the theory suggests, the ion current collection is expected to depart significantly from the 'infinite' probe behaviour for small angles only. The dotted line thus represents the current extrapolated at $\theta = 0^\circ$ which this length of probe would have collected, under the same conditions, if it would have been part of an infinitely long cylinder. This extrapolation is achieved by fitting a flexible curve tracer or spline to the curve for pitch angles between about $\pm 45^\circ$ about the peak and by smoothly joining the two sides of the narrow peak. The values of the 'infinite' probe current at $\theta = 0$, $J_\infty(0)$ estimated this way were found to be very close to the calculated values from Eq. I.4 where the current at $\theta = 90^\circ$, $J_\infty(\pi/2)$ is basically the 'infinite' probe result. This simple method was therefore used with confidence on all the experimental traces. Since the current peak is determined by the fast beam-ions only, the true base-line for the given experimental conditions shown dotted here is obtained when the slow-ion background contribution \bar{J} is subtracted uniformly for all angles, as discussed later. The full-width-at-half-maximum (FWHM) $\theta_{1/2}$ is obtained by measuring the angular width of the peak at half its height measured from the true base-line. Another half-width $\theta_{1/2}$, defined this time by the full width at the half distance between the peak maximum $J(0)$ and the 'infinite' probe extrapolation $J_\infty(0)$, was used to compare the results with the analysis of Hester and Sonin (Ref. 18). Typical traces for four values of probe voltage are shown on Fig. I-3 together with an angle template which was drawn as an overlay for convenience.

The basic flow conditions together with the probe response features described above were measured systematically on the experimental traces and recorded on perforated cards for data reduction using a computer code.

As was explained earlier in Chapter III.2.2, the local plasma potential can be estimated by using the floating (zero-current) potential V_f as shown on Fig. IV-2 to yield the nondimensional probe bias with respect to system ground

$$\phi_p \equiv \frac{e(V_p - V_{space})}{\frac{1}{2} M \bar{u}^2} \approx \frac{V_p - V_f}{V_B - V_f}$$

where V_B is the effective accelerator voltage

$$V_B = V_+ + V_D$$

where V_D is the discharge potential and V_+ and V_- the voltage on the extracting and the accelerating grid, respectively. A slight difference of about 4 volts is typically found between V_f for the perpendicular and the parallel probe orientations, and an average value is satisfactory in view of the relatively large probe biases.

The background (slow-ion) ion current \tilde{J} can be estimated and subtracted from the trace as follows. We make the reasonable assumption that the slow-ion spurious current is collected by the probe without any attitude sensitivity, as if it were in a static plasma. Thus, using

$$\frac{J_\infty(\frac{\pi}{2})}{J_\infty(0)} \equiv \frac{1 + \Phi_p}{\Phi_p} = K \text{ (no slow-ions)}$$

we get

$$\tilde{J} = \left[\frac{\text{measured} \quad \text{extrapolated}}{(J_\infty(\frac{\pi}{2}) + \tilde{J}) - (J_\infty(0) + \tilde{J}) \cdot K} \right]$$

where $J_\infty(0)$ is the 'infinite-probe' current at $\theta = 0$ obtained by extrapolation. Each experimental probe record is treated in this systematic way to acquire the peak features and the flow-field characteristics. To minimize the effect of varying parameters not directly pertinent to the experiment, a set of standard source conditions were rigorously followed through the extent of this study.

IV.1.2 Range of Parameters

As the theory has suggested, the characteristics of the end effect depend on a significant number of parameters which have to be accounted for to be able to measure the ion speed ratio or the ion temperature using this effect. The most pertinent parameters of interest are those of the plasma stream itself, namely the ion density, the ion bulk velocity, the ion speed ratio and the electron temperature and those related to the presence of the probe, that is, the probe bias, the probe aspect ratio (ℓ/d) and the nondimensional probe length τ_ℓ which is the major probe parameter when characterizing the finite-length effect.

Following our discussions in Section III we can attempt to tailor the ion speed ratio by using a simple model developed for a conical beam geometry. The concept of synthetic temperature introduced in Section III suggests that the ion speed ratio would scale directly with the nondimensionalized axial distance z/r_0 and would depend only on z/r_0 . Therefore both the axial distance z and the exit beam radius r_0 were varied to cover a range of speed ratios from about

10 to 100. Ion beam directed energies between 60 eV and 1200 eV were considered. Since the end effect is not expected to have any first order sensitivity to the electron temperature, no attempt was made to vary this parameter within the plasma flow.

The probe parameters discussed in our theoretical considerations (Chapter I) are basically dictated by the range of validity of the analysis for the end effect. In order to cover the widest range possible for the probe bias, Φ_p was varied from about 0.03 to 1. For the nominal operating regime of the plasma source the conical beam ion density varies roughly as $(z/r_o)^{-2}$. Probe diameters of 0.01 to 0.05 cm were used to test the sensitivity of the effect to the probe radius to Debye length ratio, ϵ , within a range of about 0.01 to 0.5. Finally, since the finite length effect is most noticeable for values of τ_ℓ ,

$$\tau_\ell \equiv \frac{\ell}{u} \sqrt{\frac{e^2 n_i}{\epsilon_o M}}$$

smaller than about 1.5 (Ch. I), this requirement dictated the use of probe ℓ/d ratios from about 20-500, such that we eventually covered τ_ℓ values from 0.01 to 1.5. Figure II-11(b) gives all the experimental runs according to the various ranges outlined above.

IV.2 Verification of the Finite-Probe Theory

IV.2.1 Behaviour of the Main Peak Features

A first basic inspection of Sanmartin's theory can be made by the determination of the dependence of the probe current response on probe bias. The two main features of interest concerning the peak are undoubtedly its height and its width since they both convey valuable ion temperature information. The analysis indicates that the peak height should grow, to first order, as

$$J(\theta = 0) \propto \Phi_p \quad (\text{IV.1})$$

and that the width at half-maximum should basically be independent of Φ_p .

A typical example of this dependence is shown on Fig. IV.3 where a series of traces are superposed to show the peak growth with varying probe bias. The peak is vanishingly small for values of probe voltage near floating potential. A slight asymmetry which can be seen on the extrapolation at $\theta = 0$ is ascribed to not quite ideal alignment of the probe on the centre-line. Once the slow-ion contribution is properly subtracted, the linear growth of the peak value with absolute probe bias can be verified, as shown on Fig. IV-4 for a number of probes. One notices, in particular, the extent of probe bias covered which indicates that the linear relationship is preserved for very large voltages. The peak half-width was found to be independent of the bias in accordance with the theory, for nondimensional probe bias values as high as 1/2 as shown on Fig. IV-5 for 6 different experiments. In addition, the product

$$\frac{J}{J_\infty} (\theta = 0) \cdot \hat{\theta}_{\frac{1}{2}} \propto \sqrt{\Phi_p} \quad (\text{IV.2})$$

is found to scale according to the theory, confirming the proportionality of $J_{\infty}(\theta = 0)$ with $\sqrt{\Phi_p}$.

IV.2.2 Comparison With Previous Experiments

The dependence of the current to the finite parallel cylindrical probe on the nondimensional probe length τ_l , as first proposed by Hester and Sonin (Ref. 18), was corroborated by these authors themselves with a series of experiments conducted with three probes in an argon beam. The ion accelerator they used was an electron-bombardment ion thruster very similar to the one used here. Hester and Sonin report the following experimental conditions:

$$d = 0.013 \text{ cm}, \quad \frac{l}{d} = 75,135,225$$

$$\psi_p \leq -15$$

$$5 < Ma < 40$$

$$4000^\circ\text{K} < T_e < 60,000^\circ\text{K} \text{ and } \frac{T_i}{T_e} \ll 1$$

$$0.2 \lesssim \tau_l < 4$$

As a matter of comparison these results and the analytical curves pertinent to the range of parameters studied by Hester and Sonin are reproduced from Sanmartin (Ref. 22) on Fig. IV-6, as a function of probe length and the ratio of probe radius to Debye length. Two curves obtained by Sanmartin for small temperature ratios T_i/T_e are shown along with the curves of Hester and Sonin which are for zero values of this ratio. The results agree relatively well with the theoretical predictions.

In order to produce some comparison with the Hester and Sonin numerical solutions (Ref. 18) we have shown on Fig. IV-7 two groups of experimental results obtained in the current investigation for a range of temperature ratio significantly larger than the ones reported previously,

$$0.5 < \beta < 3.5 \quad (\text{this report})$$

$$\beta < 2 \times 10^{-2} \quad (\text{Hester-Sonin})$$

together with 3 theoretical curves obtained from Hester and Sonin (Ref. 18). The experiments were sorted into two groups, which are distinguished by different ranges for the β ratios. Since the experimental results within each group were obtained for a relatively wide range of experimental conditions, they are not expected to belong to a single β - ϵ curve, however we wish to indicate that the Hester-Sonin predictions are relatively well compatible with the experimental results obtained for the high β values reported here.

Both the numerical computations provided by Hester and Sonin and Sanmartin's more elaborate analytical description demonstrate that the end effect would not display any first order sensitivity to electron temperature. A graphical representation such as the one on Figs. IV-6 and IV-7 however may seem a bit confusing to the reader. The experimental curves shown dotted on Fig. IV-6 for the two values of temperature ratio (β) of 10^{-2} and 10^{-3} appear to demonstrate a sensitivity to electron temperature which could be significant for the smaller values of ϵ , that is, for the range where the sheath radius or the Debye length are much larger than the probe radius. In fact, we know that Hester and Sonin have varied the absolute value of T_e from about 0.3 to 5 eV. The apparent effects of β and ϵ are deceptive since a change in T_e varies the values of β , ϵ and ψ_p simultaneously in such a way as to keep $j/j_\infty(0)$ nearly constant. Therefore we feel that the graphical representation adopted is not ideal. The contention that the ion current peak structure is not influenced significantly by the electron temperature is corroborated more clearly by the more appropriate choice of parameters we have introduced in Chapter I. The dependence on T_e cancels out except by the way of $\bar{\delta}$ which only involves a weak logarithmic dependence (Appendix K). One can, in fact, account for the correct description of the end effect by using a set of nondimensionalizing parameters which do not depend on T_e , as we will see in the next sections (Figs. IV-10, IV-11).

IV.2.3 Self-Consistent Measurement of the Speed Ratio

The method we have derived from Sanmartin's analysis to determine the ion speed ratio using the end effect stems from the speed sensitivity of both the peak height and the peak width. This means that a measurement of the current peak height at $\theta = 0$ and of the angular width at half the peak height can reinforce one another in determining the ion speed ratio. This is accomplished by using both measurements obtained from a single trace to determine the value of the parameter $\bar{\delta}$, which is the key to obtain S_i as was indicated in Section I.1.3. The interdependence of peak height and width with the various parameters and a schematic representation of the interpretation procedure is given in Fig. IV-8. A value of $\bar{\delta}$ is determined by iteration locating the intersection of two functions, as demonstrated on Fig. IV-9 for two experimental cases.

The procedure starts with the measured quantities (which determine the value of the peak-shape function X obtained by two explicit relations involving the unknown value of $\bar{\delta}$:

$$\begin{aligned} X &\equiv X(J(0), \bar{\delta}, \Phi_p, R, \tau_\ell) = X_1(\bar{\delta}) \\ X &\equiv X(\hat{\theta}_{\frac{1}{2}}, \bar{\delta}, \Phi_p, R, \tau_\ell) = X_2(\bar{\delta}) \end{aligned} \tag{IV.3}$$

Therefore, there must exist a $\bar{\delta}$ hereafter called the self-consistent $\bar{\delta}$ such that

$$X_1(\bar{\delta}_{\text{self}}) = X_2(\bar{\delta}_{\text{self}})$$

Upon finding the solution, both $\bar{\phi}$ and X are known and the value of S_i is obtained from the analytical expressions (Ch. I, Eqs. I.15 to I.18). Since $X(\theta = 0)$ depends on the parameter η , this latter parameter can in turn be determined from Eq. I.19 which has the general form

$$\eta \equiv \eta(\bar{\phi}_{\text{self}}, \Phi_p, R, \tau_\ell, S_i)$$

and has to be solved numerically. A simple iterative computer program was used to determine S_i using the set of data points obtained from all the recorded traces using this scheme.

IV.2.4 Sensitivity of the Peak Features to Speed Ratio

In order to demonstrate the ability to describe the end effect completely using the proposed set of parameters which are readily available from measurement,

$$\Phi_p, R, \tau_\ell, S_i, \bar{\phi}$$

we have presented on Figs. IV-10 and IV-11 the solution for the peak height and the peak width in terms of these parameters. As a global indication of experimental behaviour, data points for a large number of experiments are shown sorted into four speed ratio ranges. These experiments all correspond to about the same value of the parameter ϵ^* . This is not a parameter containing extra information as we have seen, since it represents the ratio of the two nondimensional probe lengths R and τ_ℓ

$$\epsilon^* \equiv \frac{\tau_\ell}{\sqrt{2} R}$$

This ratio in fact conveys the information about the relative size of the probe radius in terms of the length-scale defined in a fashion akin to the electron Debye length but containing the directed ion energy instead of the electron thermal energy, i.e.

$$\epsilon^* \equiv \frac{r_p}{D} \quad \text{and} \quad D \equiv \sqrt{\frac{\epsilon_0 (\frac{1}{2} M \bar{u}^2)}{e^2 n_i}}$$

The theoretical curves in Figs. IV-10 and IV-11 are drawn for convenience with the following set of values

$$\epsilon^* = 0.001$$

$$\Phi_p = 0.10$$

$$\bar{\phi} = 0.25$$

and the nondimensional peak current results are scaled according to the relationship we have verified previously

$$\frac{J}{J_{\infty}} (\theta = 0) \propto \bar{\delta} \sqrt{\Phi_p}$$

and plotted with the theory whereas the peak width results also obtained for the range of probe bias

$$0.03 \lesssim \Phi_p < 0.5$$

were plotted directly since they were found to be independent of both $\bar{\delta}$ and Φ_p . The four groups of data points include measured speed ratios near five nominal values, namely

$$S_i = 20, 30, 40, 60, 80$$

obtained for various probe lengths and diameters. The agreement is excellent for $0.03 \lesssim \tau_l < 1$. The experimental range of τ_l was selected for values smaller than about 1.5 for reasons evident in Figs. IV-10 and IV-11. In fact, the peak width levels off for values of τ_l smaller than 1, in general, whereas the peak height reaches a maximum at about 1 and decreases slowly thereafter. This region of interest is fortunately well suited for the range of operation of the ion source we used.

Finally, in order to conclude this verification of Sanmartin's theory concerning the dependence of the peak features on S_i and τ_l we can compare the peak half-width measured from the traces with the half-width predicted by Bettinger and Chen's theory (Ref. 17). Using the measurements of T_e (Fig. III-13) and the estimates of the ion temperature we are simulating, using the synthetic temperature model developed in Chapter III, the temperature ratio T_i/T_e pertinent to this investigation, is found to be of order of unity. The value of $\theta_{1/2}$ obtained from the end effect theory of Bettinger and Chen can therefore be evaluated:

$$\text{At } \beta \equiv \frac{T_i}{T_e} = 1$$

$$\theta_{1/2BC} \approx \frac{7.5\epsilon^*}{\Phi_p^4 S_i^{1/2}} \quad (\text{IV.5})$$

An estimate of the trend can be obtained from Fig. IV-12 on which we have plotted the ratio of the experimentally measured half-width and the half-width from Eq. IV.5:

$$\hat{\theta}_{1/2} \text{ (measured)} / \theta_{1/2BC}$$

We have added the dotted lines for three probe ℓ/d (R) values as a matter of comparison using the analytical expression of $\theta_1^{\frac{1}{2}}$ obtained from Sanmartin with $\Phi_p = 0.1$ and $\delta = 0.25$. The overall behaviour indicates that in this range of values for τ_ℓ the peak half-widths are not correctly predicted by Bettinger and Chen's analysis. At large τ_ℓ the ratio levels off to values significantly larger than unity, in contrast with the results obtained for ion to electron temperature ratios near zero, reported previously (Ref. 18). This result for T_i/T_e values near unity is consistent with the theoretical values predicted by Sanmartin, as was the one reported by Hester and Sonin, and shows that for an ion speed ratio (S_i) of 10 with a typical $\epsilon^* \simeq 0.005$, then for large τ_ℓ and $T_i/T_e \simeq 1$,

$$\frac{\theta_1^{\frac{1}{2}}}{\theta_1^{\frac{1}{2}}_{BC}} \simeq 10$$

IV.3 Discussion of Experimental Results

IV.3.1 Verification of the Geometrical Speed Ratio Model

In order to assess the merit of the method developed to measure the ion speed ratio using the end effect of cylindrical probes, we have to confront the results with the model predictions. A group of experimental results representative of the range of parameters studied are presented on Fig. IV-13 to exemplify the comparison between the self-consistent values of S_i with the model-line which is drawn according to the simple relation

$$S_{i \text{ geo}} = \frac{3\pi}{8} \left(\frac{z}{r_o} \right)$$

The trend seems to favour a power law which is slower than $(z/r_o)^{+1}$. The overall behaviour therefore indicates that the measured speed ratios are higher than the model suggests, whereas at the high z/r_o the values of S_i measured fall short of the model. The results obtained with the very short probe (open diamonds) suggest that the probe behaviour for small aspect ratios differs appreciably from the theoretical predictions. Specific conclusions in this regard are difficult because the sensitivity of such short probes to speed ratios is predicted to be low for values of S_i above about 30 as shown in Figs. I-7 and I-8.

This general departure from the geometrical model can be explained in terms of real flow-field effects rather than probe effects. The arguments which justify the synthetic ion temperature simulation are based on the simplified geometry of an ideal conical beam. In fact, both the radial scans and the photographic records have led to observations indicating that the beam was somewhat distorted from the conical model (see Figs. II-10 and III-10) as is fairly typical of ion streams emitted from small-size ion thrusters (see Refs. 27-30 on the subject). A complex combination of plasma-electrostatic field couplings in the vicinity of the beam shaping grids is responsible for the definition and the stability of the many beamlets which rapidly merge into a well defined beam.* A careful observation of the beam structure reveals that the waist of the beam is fairly constant near the downstream face of the accelerator and for a few

* See on this subject Refs. 26, 27, 65, 68, 71.

diameters away, and that the ion stream-lines bend slightly outward to reach a fairly constant expansion. Therefore, the virtual origin of the conical envelope is shifted forward while the actual stream-lines are slightly curved rather than ideally straight. Closer in, therefore, the model would overestimate the maximum transverse velocity component accessible to the ions and thus, according to the synthetic temperature scheme, the speed ratio simulated would be underestimated as indicated by the measurements. The model is recovered at about $z/r_0 \simeq 30$. Conversely because of the curvature of the ion stream-lines the transverse velocity components would be underestimated beyond this station, thus leading to an over-estimation of the speed ratio which is also observed. At large axial distances, however ($z/r_0 \gtrsim 90$), the speed ratios measured using the finite probe effect seem to level off. This also is believed to be a real flow-field effect rather than a lack of refinement of the method. It is typically expected for speed ratios larger than roughly 100, for probes with an aspect ratio (l/d) greater than about 100, as indicated on Figs. I-7 and I-8 where the nondimensional probe length τ_l is near unity. Such an indication was also suggested by an experimental investigation reported in the literature (Ref. 78) which showed that the ion Mach number measured by scanning cup-analyzers levelled off to a 'saturated' value for large axial distances downstream. The ion source was similar in conception to the one used for this experiment. The weight of evidence at this stage is to ascribe the measured results to a non-perfect flow model rather than to a defect in the probe theory. To shed more light on this we will present a more complete correlation of the results.

IV.3.2 Reliability of the Method to Measure the Speed Ratio

(a) Ion Source Effects

In order to account for any spurious effect originating in the ion source itself which could perturb the probe signal, we have grouped a set of data points obtained for a value of z/r_0 of 40 for different beam energies. The ion speed ratios which are obtained from the self-consistent solution at a given ion beam energy are normalized for convenience with respect to the speed ratio measured at a reference beam energy of 700 volts. Such a correlation of the results is presented in Fig. IV-14. The choice of $z/r_0 = 40$ provides an overlapping of the results obtained with the two grid sets which were used to cover a wider range of z/r_0 by merely doubling the beam diameter:

$$2r_0 = 2.54 \text{ cm}; \quad \gamma \simeq 10^\circ$$

$$2r_0 = 5.08 \text{ cm}; \quad \gamma \simeq 14^\circ$$

A slight variation of the beam divergence angle γ has not been thought to introduce any significant variation in the measured values of S_i for the two beam sizes. It is, however, evident from the trend of S_i that the ion source does introduce a spurious beam energy dependence for energies lower than about 300 eV. Such an artificial dependence of S_i on beam energy must therefore be kept in mind when attempting to properly scale the ion temperature in the flow-field, especially for simulation purposes. For beam energies larger than 300 eV, the results are nevertheless consistent with one another within about 15% up to the maximum value of beam energy we have used (1200 eV).

When one considers the relatively complex mechanisms responsible for the emission of the ions into a well defined beam (see Section III.1.2), it is not surprising to obtain a certain modification of the beam structure for the lower part of the accelerator voltage range. In fact, it is well known from experience with ion engines that the beam formation becomes imperfect in the lower extraction voltages. This behaviour can be demonstrated further when the low-voltage accelerator configuration is used. In this mode the optics of the beam forming apertures are less constrained because there is only a single extraction grid (Fig. II-5). The ion speed ratios measured under these conditions are presented in Fig. IV-15 where the probes were again positioned at a z/r_0 value of 40. A stronger net beam voltage dependence is shown in this configuration.

(b) Probe Bias Effects

We can further estimate the reliability of the method to measure S_i by noting the effect of a substantial variation of the probe bias on the values of S_i obtained from the probe response. Three sets of data points are presented on Fig. IV-16 which show that the probe bias does not affect the speed ratios generated by the method significantly. No systematic influence is observed for a probe bias range which covers in excess of one order of magnitude change in Φ_p

$$0.03 < \Phi_p \lesssim 0.5$$

We have added three experimental points obtained from Ref. 57 for comparison, in which Fournier and Pigache report some attempts to verify Sanmartin's finite probe theory. These quantitative attempts, though limited in number were made to obtain an estimate of the ion speed ratio according to Sanmartin's analytical description. The authors did not use a self-consistent scheme but actually estimated the value of $\bar{\phi}$ which they introduced in the analytical expressions. The significant dependence on Φ_p displayed in Fig. IV-16 by their data points could possibly be tied to an incorrect choice for $\bar{\phi}$ (see Section IV.4.2).

(c) Probe Aspect Ratio Dependence

To complete our test of the degree of refinement obtained by the method proposed to determine the ion speed ratio using the end effect, we must verify the correlation between the values of S_i determined by the use of significantly different probe aspect ratios. This information was already available in Fig. IV-13. The variations between the values of S_i measured by six different probe l/d ratios are repeated in Fig. IV-17. These values of S_i are obtained at a fixed z/r_0 which is equivalent, according to our geometrical model, to keeping S_i constant. These typical results indicate that the values of S_i determined by direct measurement of the probe angular response are consistent within about 20% for a probe aspect ratio greater than about 70. The anomalous behaviour for the very low aspect ratio probe is again quite different.

Using the same group of data points we can also illustrate the fact that the method leads to a reasonable agreement between the values of S_i detected by different probe sizes. Figure IV-18 which compares measurements at two different stations (or nominal speed ratio values) suggests that the absolute probe diameter does not introduce any systematic dependence on the measurement of S_i , at least for the range studied here. In particular, the group of points at 4, 8

and 10 mils which correspond to probes with roughly the same probe aspect ratio ($l/d \approx 170$) was purposely selected to corroborate this fact. The data points shown at 20 mils correspond to the anomalous $R \approx 22$ case, therefore no conclusion about the influence of the probe diameter on the integrity of the method can be drawn from this particular probe. Since the importance of the end effect decreases with increasing probe diameter, at a given set of stream conditions, one can expect the sensitivity of the finite probe to S_1 to decrease accordingly (see Fig. I-8). However, we can estimate that a 20 mil-diameter probe with a value of l/d of 170 would not have yielded a measurement of S_1 significantly different from the ones obtained with the probes used here.

IV.3.3 Reconstruction of the Probe Response

In order to implement Sanmartin's theoretical analysis of the end effect and to demonstrate the overall ability of the self-consistent method which we developed to obtain the ion speed ratio from the angular response of cylindrical probes, we have generated a simple computer code which reconstructs the entire probe response. It requires the values of the beam and of the probe parameters, together with the values of $\bar{\delta}$ and of S_1 obtained by the self-consistent procedure. Thus, by using the following features measured from the experimental traces,

$$J(\theta = 0), J_{\infty}(\theta = 0), J(\theta = \pi/2), \hat{\theta}_{\frac{1}{2}}$$

the entire current angular response, i.e. over the entire angular range,

$$0^\circ \leq \theta \leq 90^\circ$$

can be reproduced as shown in Fig. IV-19. The computer plots are scaled according to the real current scale such that the normalizing value of $J_{\infty}(\theta = 0)$ corresponds to unity. Two curves are plotted for each comparison. First the peak structure is traced for

$$0 \leq \theta \lesssim 30^\circ$$

and then the 'infinite' probe response is superposed on the graph for

$$0^\circ \leq \theta \leq 90^\circ$$

in order to check the extrapolated region as shown on the lab trace. A scale amplification factor of 4 is also used for the angle axis to compare the theory with the experimental traces which were also taken with an identical angular sensitivity ($\times 4$) in order to measure the behaviour at small angles more accurately.

A set of 12 cases were selected for comparison. This set covers the complete range of the parameters studied and is listed in Fig. IV-20 with the

corresponding parameters. The direct comparisons are shown on Figs. IV-21(a) to (e) where the theoretical curves are matched to the measured traces. Some extra features are added such as a thick vertical bar on the angle-axis locating the predicted value for the limit to the range of validity of the theory and a thin horizontal line locating the half-widths according to the nomenclature introduced in Fig. IV-1. The open symbols superposed on the theoretical curves are discrete measurements of the current response. In each case the actual experimental curve is shown for one half of the complete angular range from -90° to $+90^\circ$. To obtain a clear exposition the other half of the angular range shows the theoretical result as a solid curve, with superposed discrete experimental measurements. Each case includes the normal and the X^4 blow-up, for both theory and measurement. After inspection we can conclude that, in general, the agreement is excellent.

We can see that the theory indicates that the peak current approaches zero for large angles and thus it fails to describe the peak structure correctly for values of pitch angle which are beyond about two half-widths from the maximum ($\theta = 0$). If we take the more natural definition for the limit to the validity of the theory as the angle at which the peak prediction equals the 'infinite' probe value, we make the following observation from the 12 typical cases depicted in Fig. IV-21 - namely, that the theoretical limit obtained by Sanmartin,

$$\theta_{\text{lim}} \approx \sqrt{2\bar{\delta} \Phi_p - \left(\frac{2}{S_i}\right)^2} \quad (\text{IV.6})$$

as indicated by the thick vertical bar, systematically overestimates the intersecting points of the two calculated curves. In fact we have obtained the corresponding intersection experimentally by smoothly extrapolating both the decrease in peak current and the 'infinite' probe current on each lab trace. The comparisons for the location of this intersection are shown in Fig. IV-22 where the full and the open symbols are the intercepts obtained for the measured and the calculated cases, respectively. Since in the expression for θ_{lim} the leading term, proportional to $\bar{\delta}$, dominates for values of $S_i > 20$, this curve appears to favour values of $\bar{\delta}$ smaller than those calculated using Sanmartin's approximation (Eq. I.39) by about 40%. A similar conclusion results from a direct comparison of the values of $\bar{\delta}$ obtained from the self-consistent calculational process with the values from Sanmartin's approximation.

A relation between the nondimensional probe bias Φ_p and $\bar{\delta}$ can be obtained using Eq. I.39.

$$\Phi_p \approx \exp \left[2\bar{\delta}^{-1} - \ln \bar{\delta} + 0.307 - 2 \ln \left(\frac{1}{\epsilon^*} \right) \right] \quad (\text{IV.7})$$

This relation is plotted in Fig. IV-23, with ϵ^* as a parameter, together with a number of experimental values of Φ_p , $\bar{\delta}_{\text{self}}$ and ϵ^* . These data points are referring to the self-consistent values for $\bar{\delta}$ obtained using our regular procedure. A direct comparison using the full circles for instance, shows that for any of the given Φ_p reported here for an $\epsilon^* \approx .01$ the value of the self-consistent $\bar{\delta}$ which is obtained is smaller than the corresponding approximated value derived from the curve by about 30%. This disagreement is believed to be due to a readjustment necessitated by the fact that the real flow field deviates from the assumed conical cum Maxwellian models and thus requires that the theoretical value be slightly modified.

IV.3.4 Non-Maxwellian Effects

An effect which is not accounted for by the theory is materialized in the occurrence of side-peaks on the probe response. These peaks have a much smaller amplitude than the main peak. They actually could only be detected with the long slender cylindrical probe (Fig. IV-24) or with the small collimated Faraday cups (Fig. A-5). Such secondary peaks were also observed by Fournier and Pigache (Ref. 57) on the current angular response of their small cups. In order to reconcile large discrepancies between the speed ratios they estimated by a method briefly outlined in our Appendix D, and some rough estimates they obtained using Sanmartin's analysis, they first alluded to the possibility of non-Maxwellian effects. Indeed, Sanmartin's analysis was based on the assumption of an ideal thermal ion population (drifting Maxwellian) far ahead of the probe. The concept of thermalization introduced in our stream model, however, rests on an artificial basis. The synthetic ion population obtained from the model we have adopted is likely to be described with a distribution which is different from a Maxwellian distribution. The effect introduced is relatively small. Thus we are led to believe that, since the results are not basically in error, the deviation from ideal Maxwellian does not lead to serious complications and furthermore that the use of the self-consistent method appears to provide some of the required adjustments automatically.

The fact that two very much different probe structures would detect the secondary peaks in a similar fashion is not so surprising. Indeed, both ion collection schemes are sensitive to the transverse component of the ion population. Therefore, these observations must reflect some anomaly occurring in the flow itself since they are not restricted to a particular probe type.

Although only limited quantitative arguments can be invoked, we can attempt to elucidate the question of the origin of the secondary peaks by locating at what angles the measured side-peak features are occurring on the traces. These angles are indicated in Figs. IV-24 and A-5. We notice that they are located at angular positions which are beyond the angular width of the source exit diameter D_0 as sighted at the given probe location (typically 2° to 5°). These positions of the side-peaks correspond to angles which are close to the spreading angle γ of the source in all the cases reported here. We have also reported in the table below some results obtained from Ref. 57 which also show secondary peaks although under quite different experimental conditions. These results are summarized in the following table:

Long Cylindrical Probe (Fig. IV-24)

z/r_0	Secondary Peak Location	Source Divergence Angle
52	$\sim 9.2^\circ$ ($V_B = 500V$)	$\gamma \simeq 10^\circ$ ($D_0 = 2.5$ cm)
25	$\sim 12.8^\circ$ ($V_B = 300-500V$)	$\gamma \simeq 14^\circ$ ($D_0 = 5.0$ cm)
35	$\sim 15.7^\circ$ ($V_B = 300V$)	$\gamma \simeq 14^\circ$ ($D_0 = 5.0$ cm)

Collimated Faraday-Cup Probe (Fig. A-5)

31	$\sim 8.2^\circ$ ($V_B = 500V$)	$\gamma \simeq 10^\circ$ ($D_0 = 2.5$ cm)
42	$\sim 9.2^\circ$ ($V_B = 500V$)	$\gamma \simeq 10^\circ$ ($D_0 = 2.5$ cm)
182 (Ref.57)	$\sim 3.5-4^\circ$ ($V_B \simeq 20V$)	$\gamma \simeq 10^\circ$ ($D_0 = 10$ cm)

We notice finally that the side-peaks are vanishingly small for the larger beam energies as shown in Fig. IV-24. This effect likely originates at the accelerator grids. Although no photographic records have supported this possibility, it is conceivable that a small sub-beam, fringing symmetrically outward within the main beam is produced because of a fortuitous inhomogeneous ion density at the grid and that the effect is compounded at lower beam energies (see Section IV.3.4a). In final analysis, however, the observation of these small secondary features is an indication of the capability to resolve fine structure with the probe effect.

IV.3.5 Estimate of Errors

Our confidence in the ion speed ratios measured using the ion temperature sensitivity of the finite cylindrical probe is supported by the fact that the results were found to be consistent within our conservative estimate of the margin of error even though some departure from our simplified model was found to be significant for the larger values of S_1 .

In order to get this estimate of the margin of error, we can refer to the schematic representation of the method we have used to obtain both the characteristic field length $\bar{\phi}$, and the ion speed ratio S_1 , according to a self-consistent scheme as shown in Figs. IV-8 and IV-9. The arguments leading to this estimate are thus intimately related to this direct formulation of the solution. One can see that the iterative procedure yielding the self-consistent values for $\bar{\phi}$ and S_1 is hinged firstly, on the extrapolation of the 'infinite' probe current value at $\theta = 0$, secondly on the evaluation of the slow-ion offset which by the same token sets the true half-height and thereby locates the corresponding peak half-width, and thirdly on the agreement between the peak-shape functions X_1 and X_2 . After a closer inspection of Fig. IV-9 one notes that the determination of the peak-shape function X_2 obtained by the relation involving the measured half-width $\theta_{\frac{1}{2}}$ and given by

$$X_2 \sim \frac{1}{\mu_{\frac{1}{2}}} \sim \frac{1}{\theta_{\frac{1}{2}}} \quad (\text{IV.8})$$

is not strongly dependent on $\bar{\phi}$ for the range of interest, $\bar{\phi} > 0.1$, whereas X_1 obtained via the peak maximum ($\theta = 0$) using Eq. I.26 is more sensitive to $\bar{\phi}$. This is reflected in the expression generated in order to represent the relative error in both X_1 and X_2 using the analytical representations provided by I.26, I.29 and IV.8. We get

$$\frac{\Delta X_1}{X_1} \simeq \frac{\Delta R}{R} + \frac{1}{2} \left(\frac{\Delta \Phi_R}{\Phi_p} \right) + \frac{\Delta \left(\frac{J}{J_\infty}(0) \right)}{\left(\frac{J}{J_\infty}(0) \right)} + \frac{\Delta \bar{\phi}}{\bar{\phi}} + \tilde{O} \quad (\text{IV.9})$$

$$\frac{\Delta X_2}{X_2} \simeq \frac{\Delta R}{R} + \frac{\Delta(\theta_{\frac{1}{2}})}{\theta_{\frac{1}{2}}} + \tilde{O} \quad (\text{IV.10})$$

where the symbol \tilde{O} indicates an error of second order. Now since the iterative sequence is generated by comparing X_1 and X_2 in turn, it is thus reasonable to use Eqs. IV.9 and IV.10 to yield an effective relative error on $\bar{\delta}$ by putting

$$\frac{\Delta \bar{\delta}}{\bar{\delta}} \approx \frac{\Delta(\hat{\theta}_{1/2})}{\hat{\theta}_{1/2}} + \frac{1}{2} \left(\frac{\Delta \Phi_p}{\Phi_p} \right) + \frac{\Delta \left(\frac{J}{J_\infty}(0) \right)}{\left(\frac{J}{J_\infty}(0) \right)} + 2\tilde{O} \quad (\text{IV.11})$$

The relative error on R is, in fact, not likely to introduce a significant contribution in $(\Delta \bar{\delta}/\bar{\delta})$ since it would simply account for a variation acting in the 'same direction' in both X_1 and X_2 whereas the residual error \tilde{O} could be contributing in 'opposite directions' and thus the worst case is chosen.

Similarly an expression for the relative error in S_i can be arrived at. First we rearrange Eq. I.28, i.e., we get

$$S_i \equiv \frac{1}{\sqrt{\eta}} \cdot 2R \cdot \left[\frac{2}{(\pi + 0.6\tau_\ell^2)\ell n \sigma^2} \right]^{\frac{1}{2}}$$

Moreover for the experimental range considered here we can estimate, using the analysis provided in Section I.1.2, that

$$X \propto \eta^{-\frac{1}{2}} \quad (\text{IV.12})$$

Therefore the relative error in X can be assessed directly since it will contribute to the error in S_i via the final calculation of S_i , as shown in the flow-chart depicted in Fig. IV-8, i.e.,

$$\frac{\Delta X}{X} \approx \frac{1}{2} \frac{\Delta \eta}{\eta} + \tilde{O}$$

which means, using the expression obtained above for $S_i(\eta)$, for the range of interest $\tau_\ell < 1$, we have

$$\frac{\Delta S_i}{S_i} \approx \frac{1}{2} \left(\frac{\Delta \eta}{\eta} \right) + \frac{\Delta R}{R} + \tilde{O}$$

i.e.,

$$\frac{\Delta S_i}{S_i} \approx \frac{\Delta X}{X} + \frac{\Delta R}{R} + \tilde{O}$$

Once the value of $\bar{\delta}_{\text{self}}$ has been established by iteration, it follows that a conservative assessment of the relative error in S_i can be attempted using the

expression,

$$\frac{\Delta S_i}{S_i} \approx \frac{\Delta R}{R} + \frac{1}{2} \left(\frac{\Delta \Phi_p}{\Phi_p} \right) + \frac{\Delta(\hat{\theta}_{\frac{1}{2}})}{\hat{\theta}_{\frac{1}{2}}} + \frac{\Delta \left(\frac{J}{J_\infty} (0) \right)}{\left(\frac{J}{J_\infty} (0) \right)} + \tilde{O} \quad (\text{IV.13})$$

Finally, we can obtain an estimate of the relative error in each of the parameters contributing to $\Delta \bar{\delta}/\bar{\delta}$ and $\Delta S_i/S_i$:

- (1) The residual error contained in \tilde{O} is not expected to exceed 4%, according to the analytical treatment, and is averaged at about 2%.
- (2) Using systematic measurements of the various cylindrical probes the average error on the probe aspect ratio is evaluated using

$$\frac{\Delta R}{R} = \frac{\Delta \ell}{\ell} + \frac{\Delta d}{d} \lesssim 3\%$$

- (3) The relative error in the determination of the probe bias can be calculated from the relation we obtained in Chapter III, i.e.,

$$\Phi_p \approx \frac{V_p - V_f}{V_+ + V_D - V_f}$$

Since we use $V_p \approx 0$, and moreover we have

$$|V_D - V_f| \ll V_+$$

then

$$\frac{\Delta \Phi_p}{\Phi_p} \approx \frac{\Delta V_f}{V_f} + \frac{\Delta V_+}{V_+} \lesssim 6\%$$

upon using the standard meter reading accuracies.

- (4) The current peak angular accuracy was evaluated at less than about 4% which corresponds to an average absolute error of less than 0.3° ; thus

$$\frac{\Delta \hat{\theta}_{\frac{1}{2}}}{\hat{\theta}_{\frac{1}{2}}} \lesssim 4\%$$

- (5) The relative error in the nondimensional current peak height $J/J_\infty (\theta = 0)$ is evaluated using the relation which was obtained for the determination of the background slow-ion contribution

$$\left[\frac{J}{J_\infty} (0) \right]_N \equiv \frac{(J(0) - \tilde{J})}{(J_\infty(0) - \tilde{J})} \quad (\text{IV.14})$$

where the subscript (N) refers to the ideal conditions prevailing when no background offset is present. A conservative estimate using our systematic treatment of the current traces and typical conditions was obtained and yields

$$\frac{\Delta \left(\frac{J}{J_{\infty}}(0) \right)}{\frac{J}{J_{\infty}}(0)} \lesssim 20\%$$

This relatively large value is due to the fact that this quantity is obtained by direct extrapolation on the trace, and that the slow-ion offset must be estimated using this extrapolated value of $J_{\infty}(0)$. The situation is complicated in cases where $J_{\infty}(0)$ is a relatively small value, comparable say to \tilde{J} , such that the relative error

$$\frac{\Delta[J_{\infty}(0) - \tilde{J}]}{J_{\infty}(0) - \tilde{J}}$$

can be large. In such cases multiple readings are obtained to improve the situation.

In conclusion the net relative error on the estimate of S_i using our method can be set at less than about 32%. Consequently the method is expected to yield ion temperatures with an accuracy in the neighbourhood of 60%. This is not such a prohibitively large error when one considers that the end effect could very well be the only, if not the simplest probe characteristic response from which the ion temperature can be directly extracted. In fact the weight of the evidence presented in the various discussions carried out in this last section shows that the measured values of S_i were, in general, consistent with one another with an accuracy better than 20%. This indication is supported by the fact that the conservative error estimates considered here were 'worst case' estimates in the sense that no statistics were introduced in the discussions. This is especially true for the measurement of the peak features as described in Section IV.1.1. As indicated for the various typical cases presented in Figs. IV-21(a) to (e), we have obtained the extrapolated value of $J_{\infty}(\theta = 0)$ and the half-width $\theta_{\frac{1}{2}}$ from both the 'standard' trace and from the 'blown-up' trace in each case, and from repeated traces in a number of cases, in order to improve the sampling of the measurements.

It can also be expected that the level of confidence in the measurement of $\bar{\phi}$, which is also allowed by our method, could be somewhat higher than the estimate suggests, such that the determination of this important field parameter could be obtained with an accuracy comparable with the one suggested by the experimental results, namely 20%. Finally it was found that the operation of the ion source in a testing facility with as low as possible a 'background' ion content would be highly desirable in order to conduct a diagnostic of the kind reported here. In final analysis we have seen that the bulk of the uncertainty in S_i is introduced when an offset current due to charge-transfer mechanisms is superposed on the sampled fast-ion current to the probes. Nevertheless one could obtain a reasonably simple scheme to account for this offset, and to estimate it off the experimental traces, without jeopardizing the overall reliability of a diagnostic method, such as the one we have adopted in this investigation to measure S_i .

CONCLUSIONS

An experimental facility providing a flexible range of high-speed, low-density plasma conditions has been designed and constructed for a number of applications ranging from the simulation of flight in the ionospheric environment to the proving of diagnostic techniques for various laboratory and industrial plasmas. The operation of the plasma source is reliable and requires only limited ancillary instrumentation.

The end effect theory proposed by J. R. Sanmartin has been validated and the various parametric dependences have been determined experimentally. A wide range of flow conditions and of probe dimensions were considered. In particular, this experimental verification was obtained over a considerably wider range of probe aspect ratios (l/d) and of ion speed ratios than was previously investigated. Moreover the effect was studied for significantly warmer ions ($T_i/T_e \simeq 1$) whereas all the cases reported until now had been obtained for basically cold ions ($T_i/T_e \simeq 0$). Sanmartin's theory was described in this report in terms of a new set of parameters more readily accessible from direct physical measurements, and which demonstrates explicitly the relatively weak sensitivity of the effect to the electron temperature. The limits to the range of validity of the theory have been outlined using this new set of parameters.

A method to measure the ion temperature, directly from the angular response of a cylindrical probe, in a collisionless plasma stream, has been demonstrated. The height and the half-width of the ion peak, which are both sensitive to the ion speed ratio, are used simultaneously to ascertain that value in a self-consistent way. The experimental results were checked against a simple geometrical model. This has led us to conclude that the flow-field model proposed was not correct as the ion streamlines were found to bend slightly downstream of the source, while the model assumed a simple conical expansion. This evidence was further corroborated after inspection of a series of radial beam profiles. However, a cross-correlation of the results indicated that the measurements of the ion speed ratio, obtained by various probes and under many flow conditions, were consistent with each other within an acceptable margin of about 20%. In fact the usefulness of the probe would be expected to be substantially improved under the ionospheric conditions for instance, since the measurements would not suffer from the inherent contribution of spurious slow-ions on the current collection, as it is the case with extended testing tunnels. Moreover the successful theoretical reproduction of the entire structure of the probe angular response, which has been derived for a number of typical cases, epitomized the overall reliability of the method. Finally we have observed that the long slender probes were able to detect interesting 'fine-structure' aspects of the drifting ion population; indeed the small secondary ion peaks detected on the probe angular response suggested that non-Maxwellian effects were introduced in the beam prior to the current collection.

Some areas of applications of the end effect can therefore be outlined. As a typical case, the method can be extended to multiple gas species in order to determine the ion temperature of the heavy constituents of the ionosphere for altitudes higher than about 300 km (H^+ , He^+ , N^+ , O^+ ...). This could have a significant advantage since the strong attitude-sensitivity, easily identified by the sharp ion peaks, could be proved useful as a sensing-and-control feature in order to obtain the fine-pointing accuracy required by sophisticated instrument

packages. This sensitivity to attitude and to random motion within the plasma stream can also be useful to the development of sources such as ion thrusters. In fact, these devices which had been developed exclusively for propulsion missions in the mid-sixties (Refs. 26,27) are now recognized as outstanding candidates for a number of industrial applications requiring an advanced quality control, such as etching and thin-film deposition techniques (Ref. 87), or even as large-scale plasma injectors for fusion machines (Refs. 85,86).

It is suggested here that a number of interesting aspects of the observation of non-Maxwellian effects on 'standard' probe characteristics could be elucidated by introducing a non-Maxwellian treatment in Sanmartin's analysis. This could eventually lead to the correct description of other probe 'distortions' under non-ideal mass-motion conditions. Finally, as an interesting and stimulating extension of this report, the experimental validation of Sanmartin's analysis reported in Ref. 23 should be carried out for the case of a quiescent collisionless plasma. Indeed, the analytical description of the ion temperature sensitivity of the end effect allows the conceptual equivalence between the steady-flow problem and the one dimensional time-dependent problem wherein an 'infinitely' long negatively biased cylinder is immersed instantaneously in an unperturbed plasma at rest and the now familiar ion current overshoots are observed.

REFERENCES

1. H. M. Mott-Smith
I. Langmuir The Theory of Collectors in Gaseous Discharges.
Phys. Rev., Vol. 28, 1926.
2. L. Tonks
I. Langmuir A General Theory of the Plasma of an Arc. Phys.
Rev., Vol. 34, 1929.
3. J. G. Laframboise Theory of Spherical and Cylindrical Langmuir Probes
in a Collisionless Maxwellian Plasma at Rest. UTIAS
Rep. No. 100, 1966.
4. I. B. Bernstein
I. N. Rabinowitz Theory of Electrostatic Probes in a Low-Density Plasma.
Phys. of Fluids, Vol. 2, No. 2, 1959.
5. J. H. deLeeuw Electrostatic Plasma Probes. Fifth Biennial Gas
Dynamics Symposium, 1963.
6. K. A. Graf
J. H. deLeeuw J. App. Phys., Vol. 38, 4466, 1967.
7. J. B. French Langmuir Probes in a Flowing Low Density Plasma.
UTIAS Rep. No. 79, 1961.
8. S. Lederman
M. H. Bloom
G. F. Widhopf Experiments on Cylindrical Electrostatic Probes in a
Slightly Ionized Hypersonic Flow. AIAA J., Vol. 6,
No. 11, 1968.
9. M. Kanal Theory of Current Collection of Moving Cylindrical
Probes. J. App. Phys., Vol. 35, No. 6, 1964.
10. E. W. Peterson
L. Talbot Collisionless Electrostatic Single-Probe and Double-
Probe Measurements. AIAA J., Vol. 8, No. 12, 1970.
11. C. L. Brundin Inst. of Engineering Research, Berkely, Rep. No.
AS-64-9, 1964.
12. M. G. Dunn
J. A. Lordi Cornell Aeronautical Laboratory, Rep. No. AI-2187-A-14,
1969.
13. A. A. Sonin The Behaviour of Free Molecule Cylindrical Langmuir
Probes in Supersonic Flows, and Their Application to
the Study of the Blunt Body Stagnation Layer. UTIAS
Rep. No. 109, 1965.
14. R. C. Tseng
L. Talbot AIAA J., No. 9, 1365, 1971.
15. M. G. Dunn
J. A. Lordi AIAA J., No. 8, 1077, 1970.
16. R. H. Kirchhoff
E. W. Peterson
L. Talbot AIAA J., No. 9, 1686, 1971.

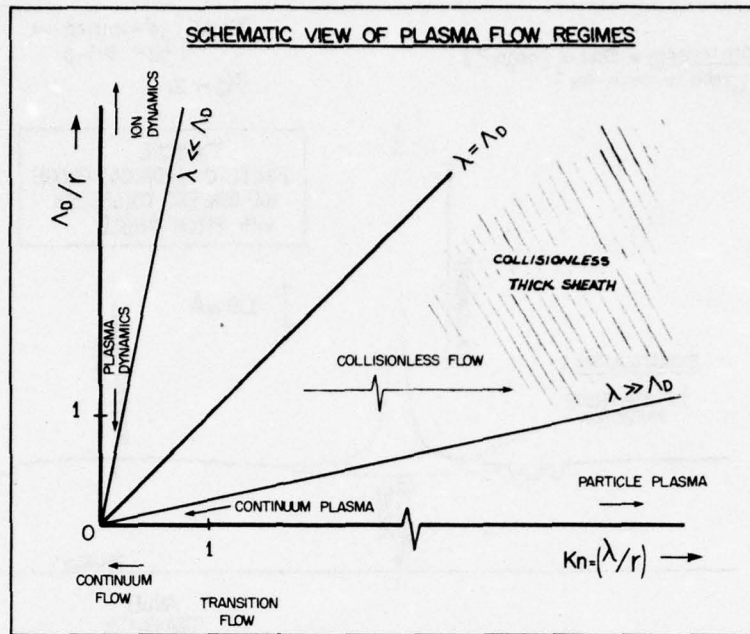
- 16a. L. H. Brace Plan. Space Sci., Vol. 13, 647, 1965.
17. R. T. Bettinger An End Effect Associated with Cylindrical Langmuir
A. A. Chen Probes Moving at Satellite Velocities. J. Geophys.
Res., Space Phys., Vol. 73, No. 7, 1968.
18. S. D. Hester An Ion Temperature Sensitive End Effect in Cylindrical
A. A. Sonin Langmuir Probe Response at Ionospheric Satellite
Conditions. Fluid Mechanics Lab., M.I.T., No. 69-9,
1969.
19. S. D. Hester A Laboratory Study of the Wakes of Ionospheric
A. A. Sonin Satellites. AIAA J., Vol. 8, No. 6, 1970.
20. S. D. Hester Some Results from a Laboratory Study of Satellite
A. A. Sonin Wake Structure and Probe Response in Collisionless
Plasma Flows. Dept. Mechanical Engineering, M.I.T.,
Rarefied Gas Dynamics, Vol. II, 1659, 1966.
21. J. R. Sanmartin End Effect in Langmuir Probe Response Under Ionospheric
Satellite Conditions. Phys. of Fluids, Vol. 15, No.
6, 1972.
22. J. R. Sanmartin End Effect in Langmuir Probe Response Under Ionospheric
Satellite Conditions. Fluid Mechanics Lab., M.I.T.,
No. 71-8, 1971.
23. J. R. Sanmartin Ion-Temperature-Sensitive Effect in Transient Langmuir
Probe Response. Phys. of Fluids, Vol. 15, No. 3, 1972.
24. J. Taillet Behavior of a Positive Probe in High-Speed Collision-
A. Brunet Free Plasma Flow. ONERA, Rapport No. 1000, France,
G. Fournier 1971.
25. G. Fournier Principle of a Simple Measure of Ion Temperature in
the Ionosphere. J. Geophys. Res., Vol. 76, No. 13,
1971.
26. F. E. Marble Physics and Technology of Ion Motors. Gordon and
J. Surugue Breach Ed., New York, 1966.
27. G. R. Brewer Ion Propulsion, Technology and Applications. Gordon
and Breach Ed., New York, 1970.
28. J. F. Wasserbauer A 5-Centimeter-Diameter Electron-Bombardment Thruster
with Permanent Magnets. NASA TN D-3628, 1966.
29. W. A. Clayden An Experimental Study of Plasma-Vehicle Interaction.
C. V. Hurdle Rarefied Gas Dynamics, Suppl. 4, Vol. II, 1966.
30. W. A. Clayden Diagnosis of a Plasma Beam Extracted from an Electron-
C. V. Hurdle Bombardment Ion Source. RARDE, England.
31. H. L. Langhaar Dimension Analysis and Theory of Models. J. Wiley
and Sons Ed., 1951.

32. S. B. Segall
D. W. Koopman Application of Cylindrical Langmuir Probes to Streaming Plasma Diagnostics. Phys. of Fluids, Vol. 16, No. 7, 1973.
33. L. Talbot A Review of Electrostatic Probe Response in a Flowing, Low Density Plasma. Rarefied Gas Dynamics, Academic Press, 1972.
- Also:
P. M. Chung Electric Probes in Stationary and Flowing Plasmas, Theory and Applications. App. Phys. & Eng. Vol. 11, 1974.
L. Talbot
34. S. H. Schwartz A Survey of Classical Langmuir Probe Theory with Applications to Flowing Ionized Gases. NASA Gr. No. NSG-409, 1964.
35. L. G. Smith Langmuir Probes in the Ionosphere. Small Rocket Instrumentation Techniques, North-Holland Publ. Co., Amsterdam, 1969.
36. W. Pfister Critical Survey of Electron and Ion Temperatures Measured with Probes. Space Res. XII, Akademie-Verlag, Berlin, 1972.
37. H. C. Carlson
J. Sayers J. Geophys. Res., Vol. 75, 4883, 1970.
38. J. V. Evans Solar Terrestrial Phys., Acad. Press, Ch. IX, 1967.
39. J. L. Donley et al Proc. Inst. Elect. Electron. Engrs., Vol. 57, 1078, 1969.
40. K. I. Gringauz Solar Terrestrial Phys., Acad. Press, Ch. X, 1967.
41. J. R. Sanmartin The Determination of Ionospheric Charged Particle Temperatures from In Situ Measurements. Space Res. XIII, Akademie-Verlag, Berlin, 1973.
42. J. G. Laframboise
L. W. Parker Probe Design for Orbit-Limited Current Collection. Phys. of Fluids, Vol. 16, No. 5, 1973.
43. G. Medicus Tech. Rep. No. AFAL-TR-71-101, 1971.
44. J. Rubinstein
J. G. Laframboise Ion Temperature Diagnostic Using a High Power Alternating Current Probe. Phys. of Fluids, Vol. 15, No. 7, 1972.
45. M. Sato Capped Probe for Ion Temperature Diagnostic in a Magnetized Plasma. Phys. of Fluids, Vol. 17, No. 10, 1974.
46. C. H. Shih
E. Levi Determination of the Collision Parameters by Means of Langmuir Probes. AIAA J., Vol. 9, No. 12, 1971.

47. D. L. Chubb Double Electrostatic Probe for Measuring Density, Temperature and Velocity of a Flowing Plasma. NASA TN D-7223, 1973.
48. J. H. deLeeuw
W.E.R. Davies Simultaneous Measurement of Temperature and Density by an Electron Beam Luminescence Technique. Small Rocket Instrumentation Techniques, North-Holland Publ. Co., Amsterdam, 1969.
49. H.S.M. Massey
E.H.S. Burhop Electronic and Ionic Impact Phenomena. Oxford at the Clarendon Press, London, 1952.
50. J. L. Delcroix Introduction à la Théorie des Gaz Ionisés. Dunod, Paris, 1958.
51. L. Spitzer, Jr. Physics of Fully Ionized Gases. Interscience Publ. Inc., New York, 1956.
52. R. T. Bettinger
E. H. Walker Relationship for Plasma Sheaths About Langmuir Probes. Phys. of Fluids, Vol. 8, No. 4, 1965.
53. J. C. Lafrance A Study of a Neon Cycle Cryogenic Pumping System for a Low Density Plasma Tunnel. UTIAS Rep. No. 116, 1966.
54. W. F. Payne Diagnostics of an Argon Free Jet Expanding from a High Pressure Inductive ARC Source. UTIAS Rep. No. 165, 1971.
55. C. M. van Atta Vacuum Science and Engineering, McGraw-Hill, 1965.
56. S. Dushman Scientific Foundations of Vacuum Technique. J. M. Lafferty Ed., New York, 1962.
57. G. Fournier
D. Pigache Transverse Ion Temperature in an Ionospheric Wind Tunnel. J. Appl. Phys., Vol. 43, No. 11, 1972.
58. N. H. Stone
W. K. Rehmann The Simulation of Ionospheric Conditions for Space Vehicles. NASA TN D-5894, 1970.
59. H. S. Ogawa
R. K. Cole
J. M. Sellen, Jr. Factors in the Electrostatic Equilibration Between a Plasma Thrust Beam and the Ambient Space Plasma. AIAA 8th Electric Propulsion Conference, AIAA No. 70-1142, 1970.
60. A. R. Martin Scaling Laws in Electron-Bombardment Ion Engines. J. British Interplanetary Soc., Vol. 25, 1972.
61. F. Rosebury Handbook of Electron Tube and Vacuum Techniques. Addison-Wesley Publ. Co. Inc., Mass., 1965.
62. D. Pigache A Laboratory Simulation of the Ionospheric Plasma. AIAA J., Vol. 11, No. 2, 1973.

63. M. Kaminsky Atomic and Ionic Impact Phenomena on Metal Surfaces. Academic Press Inc. Publ., New York, 1965.
64. G. C. Marshall Present Status of the Beam Neutralization Problem. ARS Electrostatic Propulsion Conference, Calif., 1960.
R. N. Seitz
65. J. Sellen, Jr. Study of Electron Propulsion Space Plasma and Field Interaction. NASA TM-X-52093, NASA CR-110912, 1972.
66. A. von Engel Ionized Gases. Oxford, London, 1965.
67. W. H. Wells Release No. 34-118, JPL, Calif., 1960.
68. A. Septier Focussing of Charged Particles, Vols. I and II. Academic Press, 1967.
69. J. R. Pierce Theory and Design of Electron Beams. D. van Nostrand, 1954.
70. K. R. Spangenberg Vacuum Tubes. McGraw-Hill Book Co. Inc., New York, 1948.
71. E. R. Harrison J. App. Phys., Vol. 29, No. 6, 1958.
72. J. D. Rapp J. Chem. Phys., Vol. 37, No. 1, 1962.
W. L. Francis
73. F. F. Chen Plasma Diagnostic Techniques. Huddleston and Leonard Ed., 1966.
74. A. R. Martin Numerical Solutions to the Problem of Charged Particle Flow Around an Ionospheric Spacecraft. Planet. Space Sci., Vol. 22, 1974.
75. G. E. McMichael Electron Beam Densitometer Investigation of Diffusive Separation in Front of a Blunt Body in Low Density Helium-Argon. UTIAS Rep. No. 167, 1971.
76. J. F. Bonnal Etude d'une Source d'Ions à Forte Intensité et à Rendement Elevé. Nuclear Instr. and Methods, Vol. 34, No. 3, 1965.
J. Giacomini
G. Mainfray
C. Manus
J. Morellec
77. V. Hamza Numerical Evaluation of Ion-Thruster Optics. NASA TN D-1665, 1963.
E. A. Richley
78. S. G. Alikhanov Expansion of a Plasma in Vacuum and Flow of a Collisionless Plasma Around a Plate. Soviet Phys. JETP, Vol. 32, No. 6, 1971.
V. G. Belan
G. N. Kichigin
P. Z. Chebotaev
79. S. C. Brown Basic Data of Plasma Physics. J. Wiley and Sons Inc., 1959.

80. T. L. Thomas
E. L. Battle Effects of Contamination on Langmuir Probe Measurements in Glow Discharge Plasmas. J. Appl. Phys., Vol. 41, No. 8, 1970.
81. P. A. Redhead et al The Physics of Ultrahigh Vacuum. Chapman and Hall, 1968.
82. T. A. Vanderslice Ultrahigh Vacuum and Its Applications. Prentice-Hall Ed., 1963.
83. E. P. Popov Mechanics of Materials. Prentice-Hall Ed., 1952.
84. M. Sajben
P.H.Y. Lee Inverse Problem for Electrostatic Plasma Probes. J. Appl. Phys., Vol. 41, No. 8, 1970.
85. R. C. Davis
T. C. Jernigan
O. B. Morgan
L. D. Stewart
W. L. Stirling DuoPIGatron II Ion Source. Rev. Sci. Instrum., Vol. 46, No. 5, 1975.
86. K. W. Ehlers
W. R. Baker
et al Design and Operation of an Intense Neutral Beam Source. J. Vac. Sci. Technol., Vol. 10, No. 6, 1973.
87. W. Laznovsky Advances in Low-Energy Ion Beam Technology. Vacuum Technology, 1975.



λ : mean-free-path ($\lambda_{00}, \lambda_{0\pm}, \lambda_{\pm 0}, \lambda_{\pm\mp}, \lambda_{\pm\pm}$)

FIGURE I-1

SCHEMATIC OF CYLINDRICAL PROBE & THICK SHEATH GEOMETRY
(Parallel & Perpendicular cases)

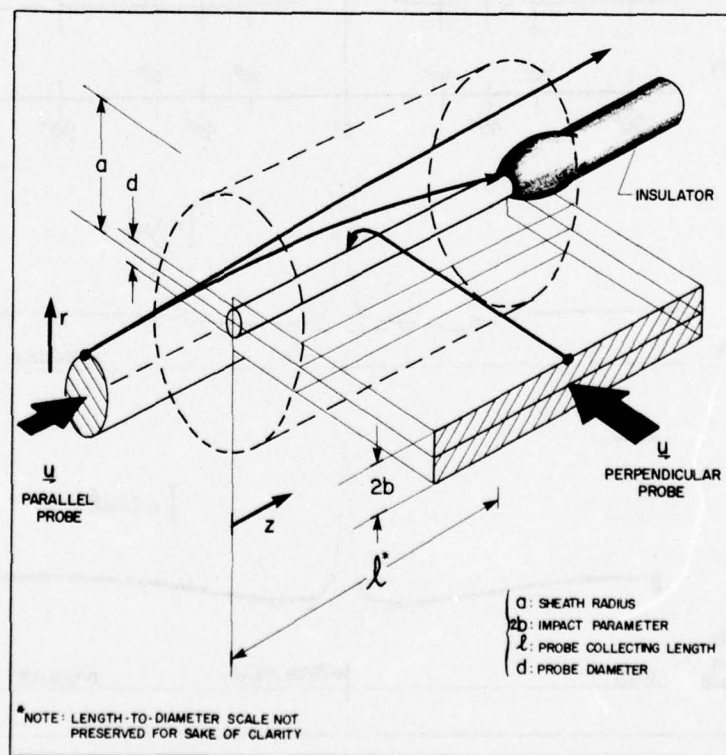


FIGURE I-2

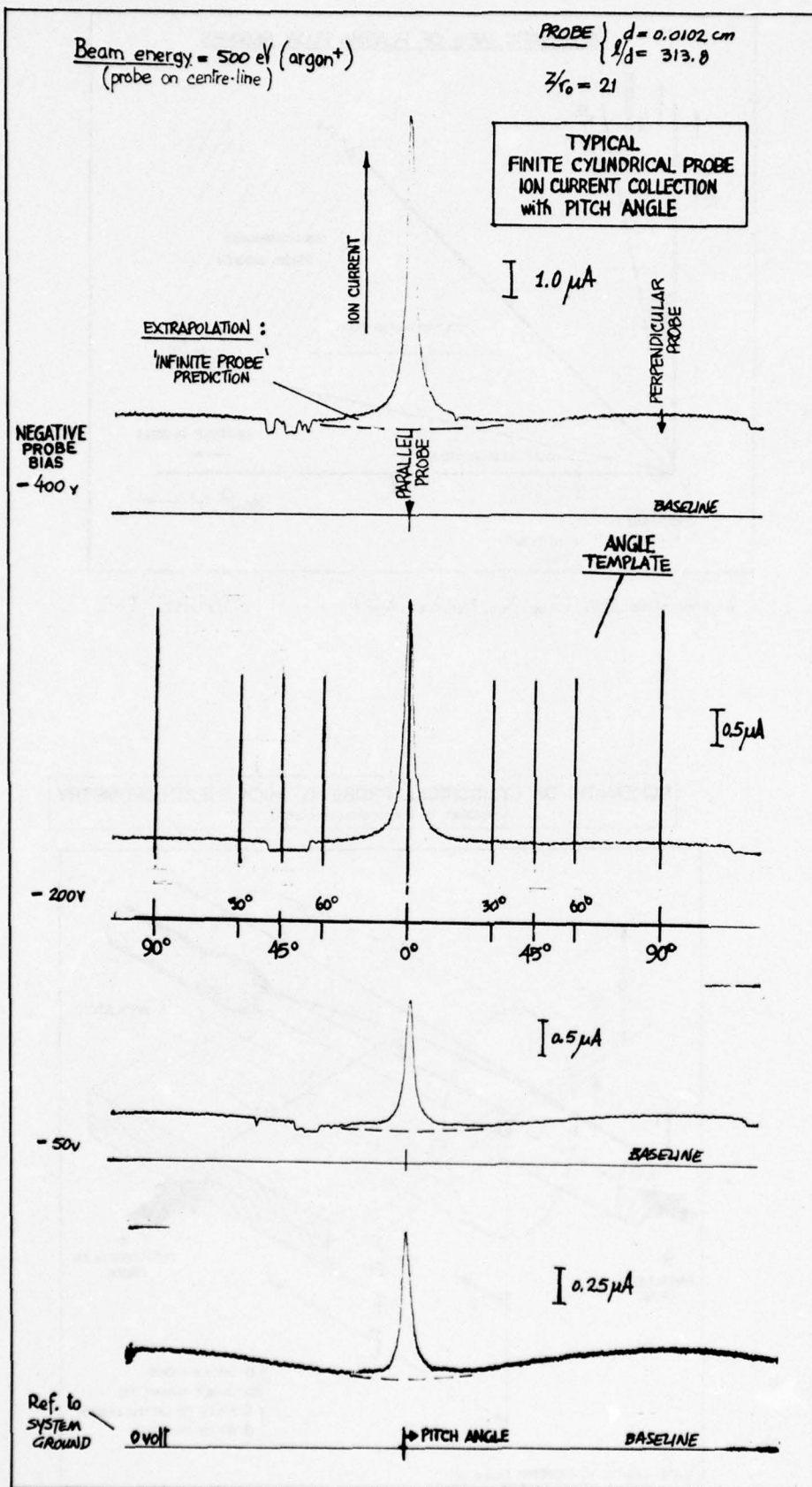


FIGURE I-3

NON-DIM. PEAK SHAPE FUNCTION: X

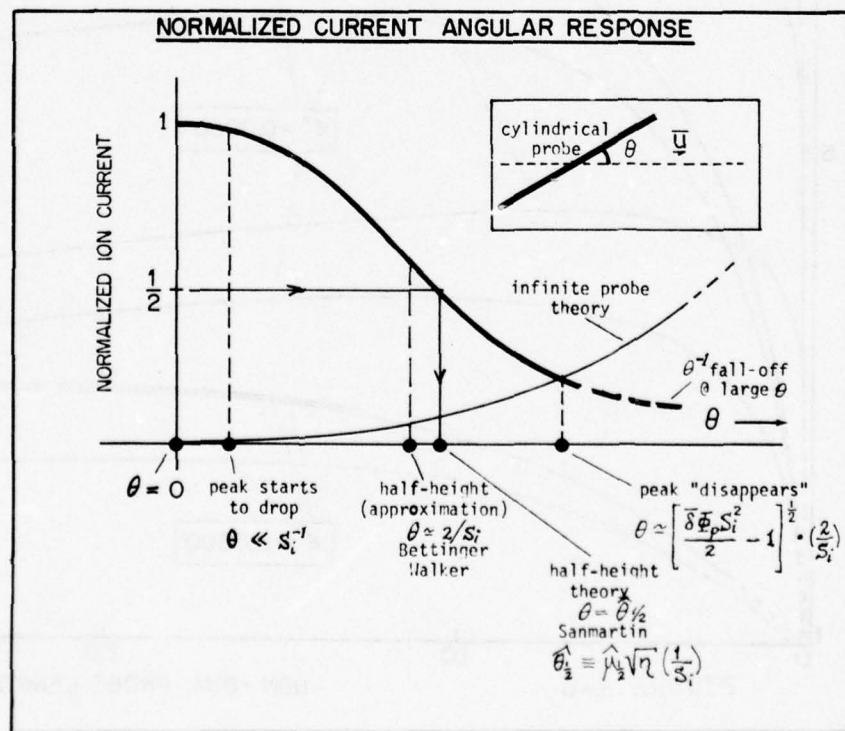
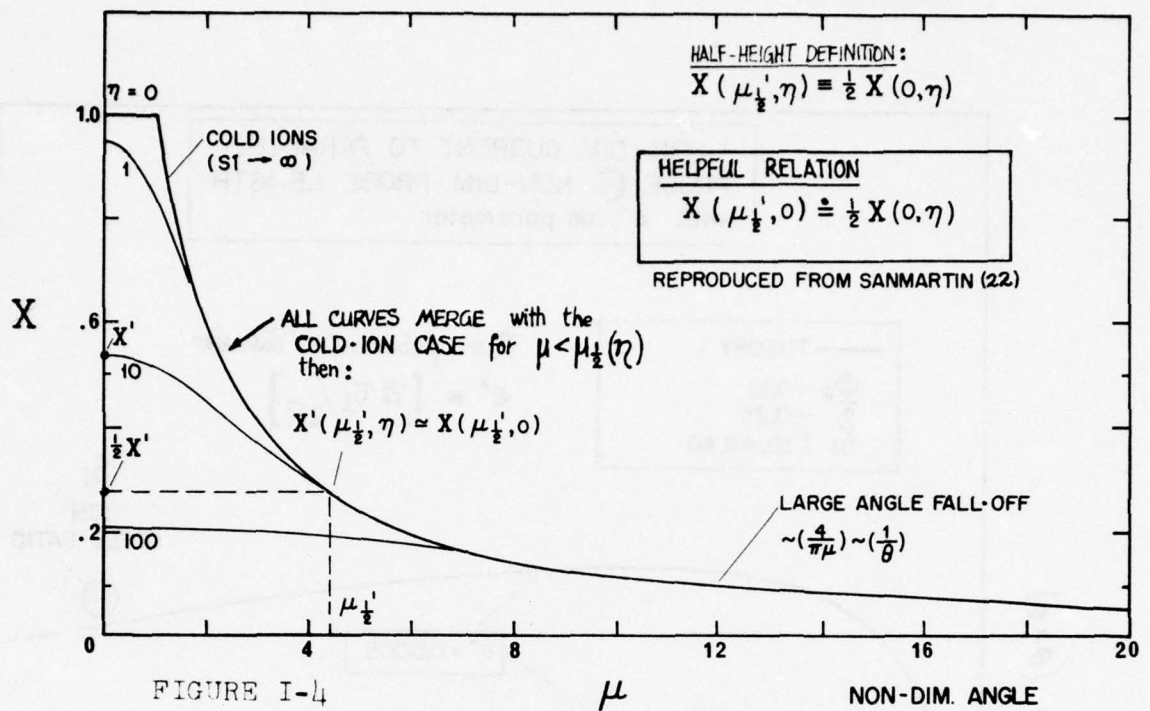
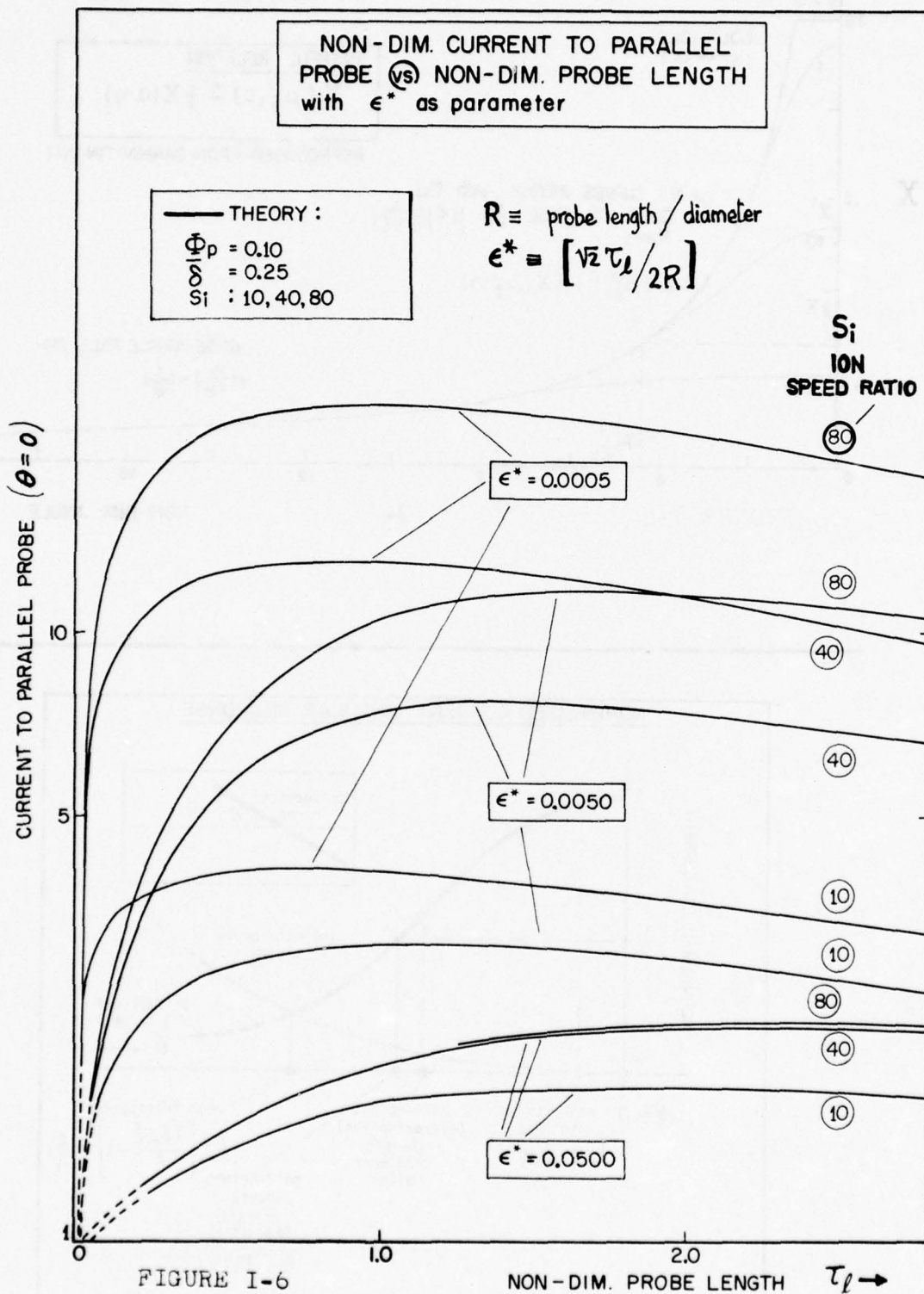


FIGURE I-5



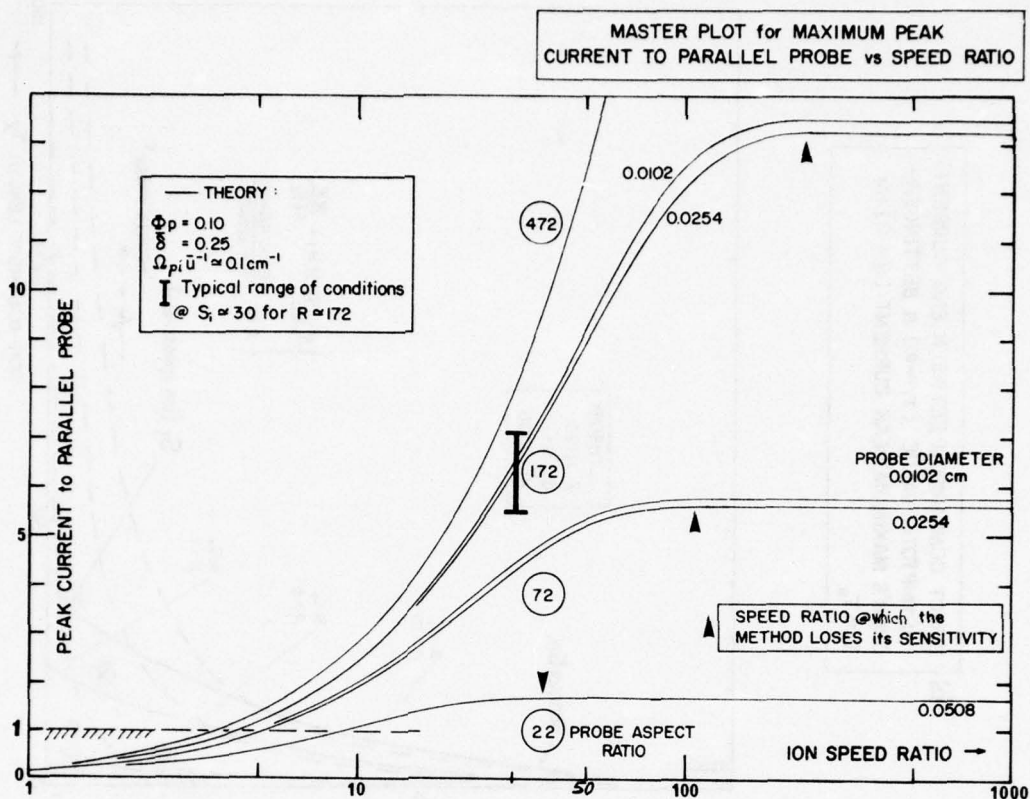


FIGURE I-7

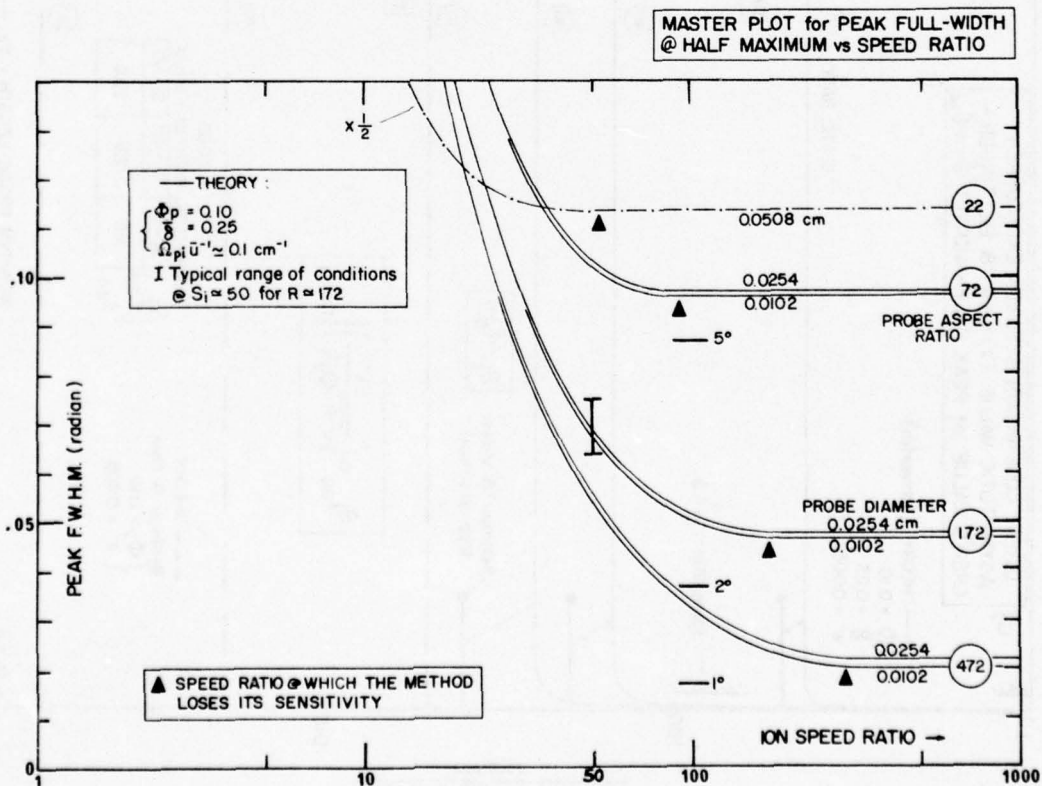


FIGURE I-8

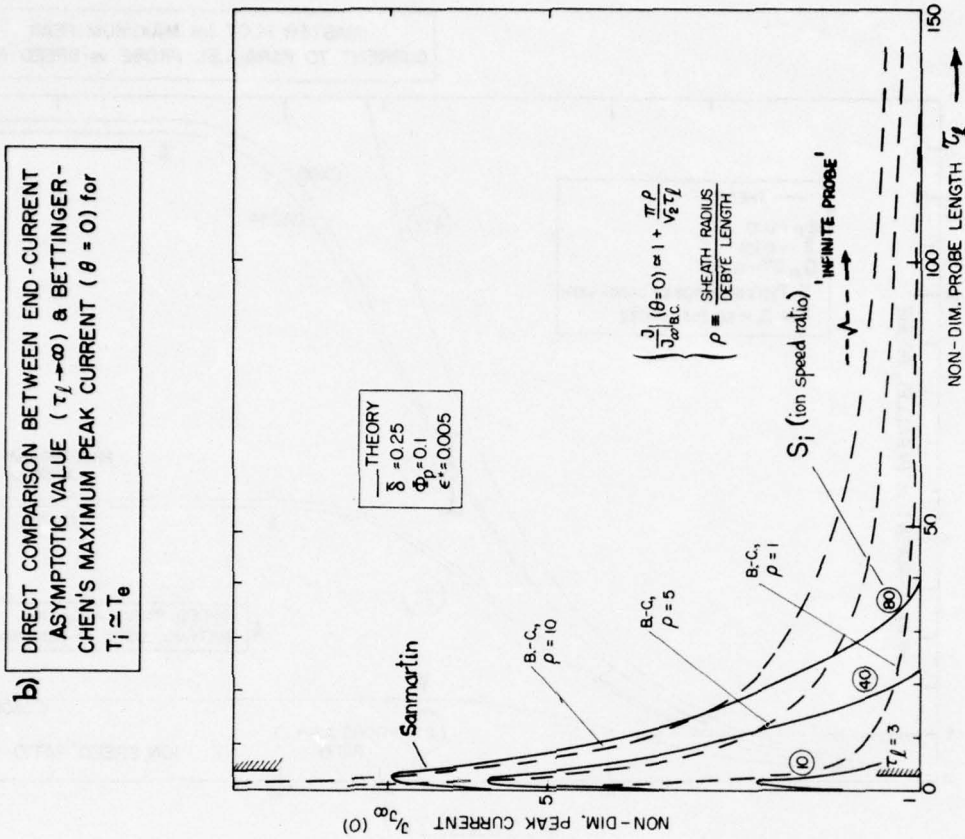
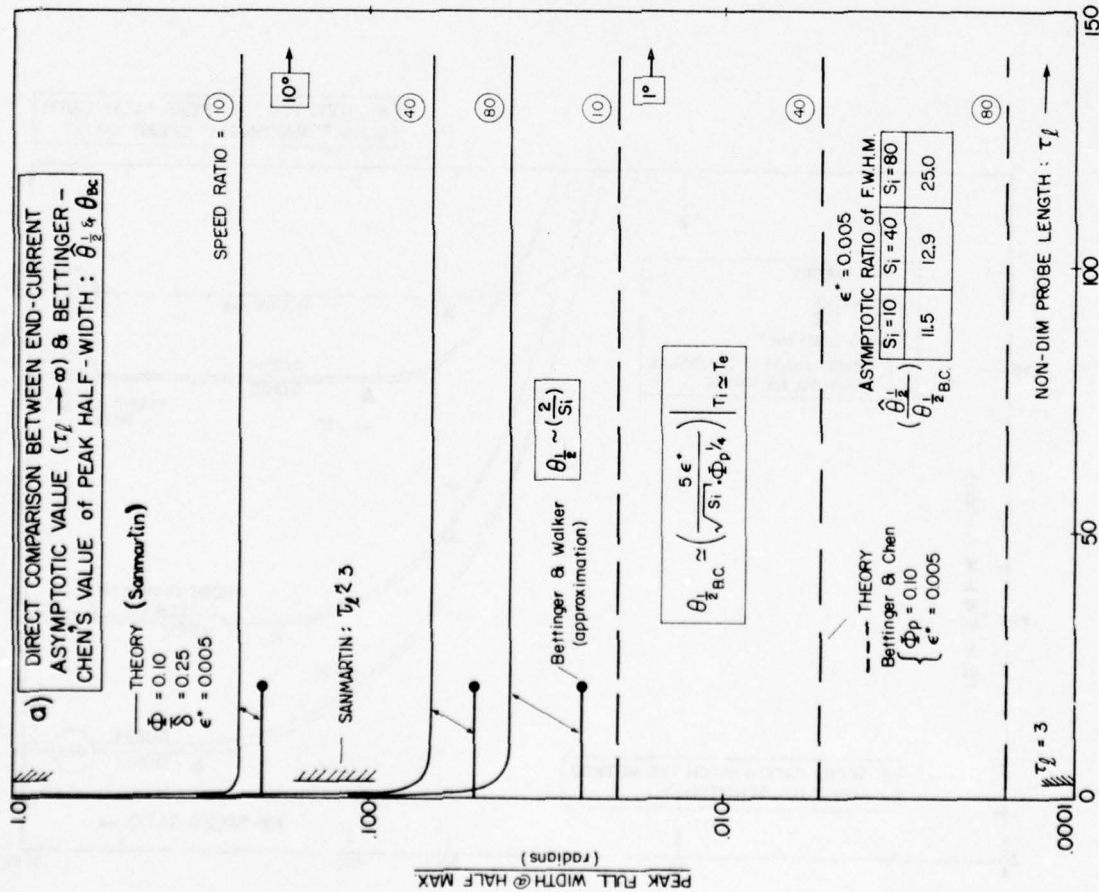
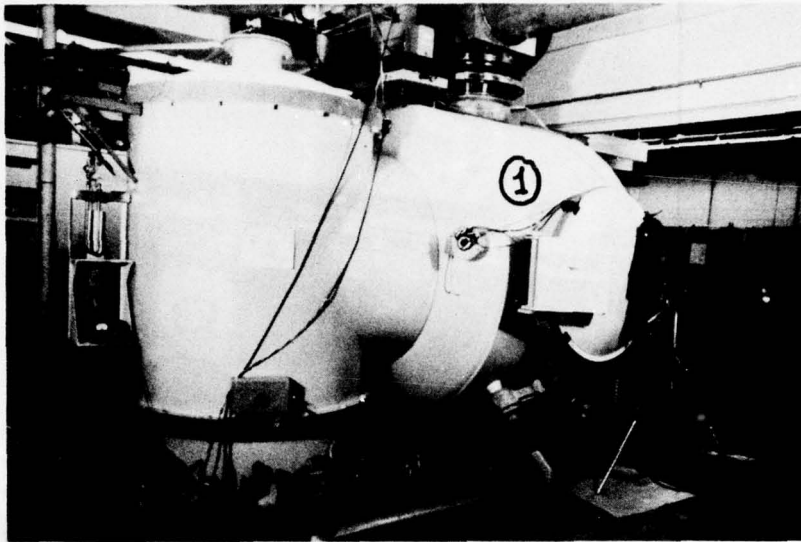


FIGURE I-9a), b)

EXPERIMENTAL SET-UP :



- ① TEST SECTION (2.13 m dia.)
- ② SOURCE ISOLATION CHAMBER

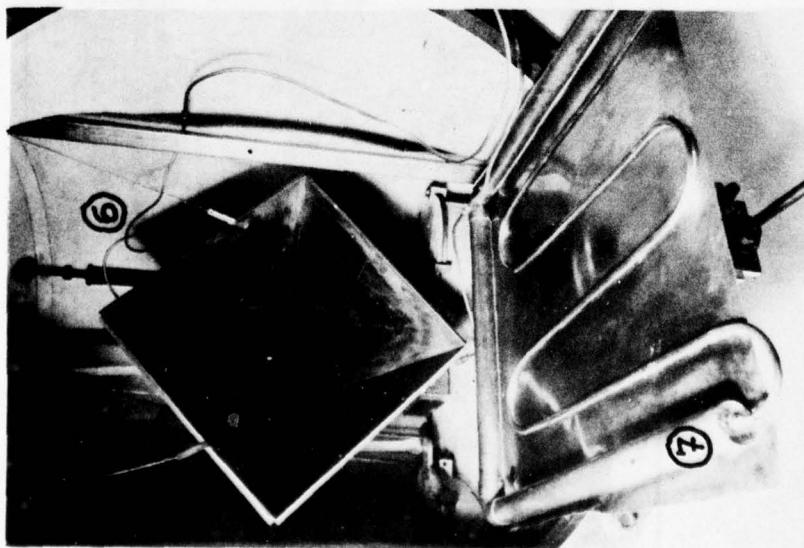


- ③ Actuator & PROBE CIRCUITRY
- ④ ION ACCELERATOR CONTROLS

FIGURE II-1

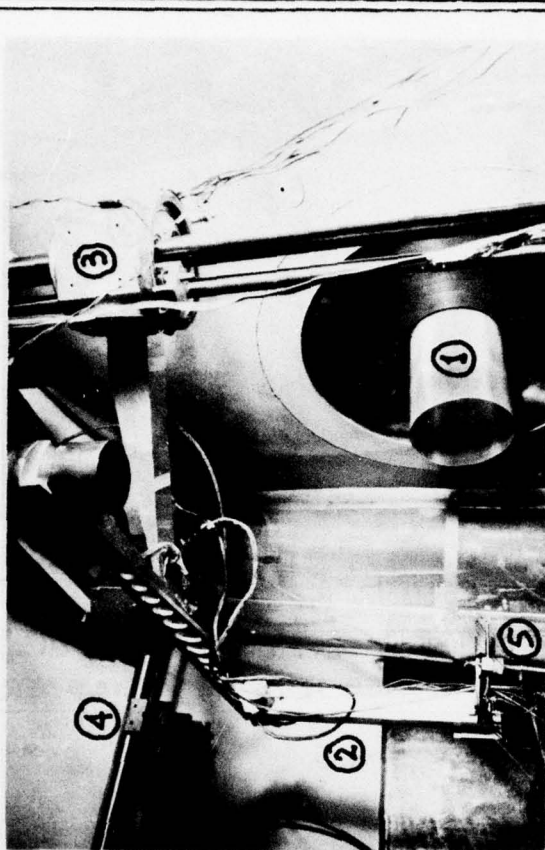
TEST SECTION HARDWARE

DOWNSTREAM



- ⑥ WATER-COOLED PYRAMIDAL BEAM COLLECTOR @ ~ 2m DOWNSTREAM
- ⑦ LN₂ COOLED BAFFLE (1m²)

UPSTREAM



- ① ION ACCELERATOR 'SHADOW' SHIELD
- ② PITCH & YAW PROBE ACTUATOR UNIT
- ③ XY TRAVERSING UNIT
- ④ Z TRAVERSING RAIL
- ⑤ PROBE RAKE ON ϕ

FIGURE II-2

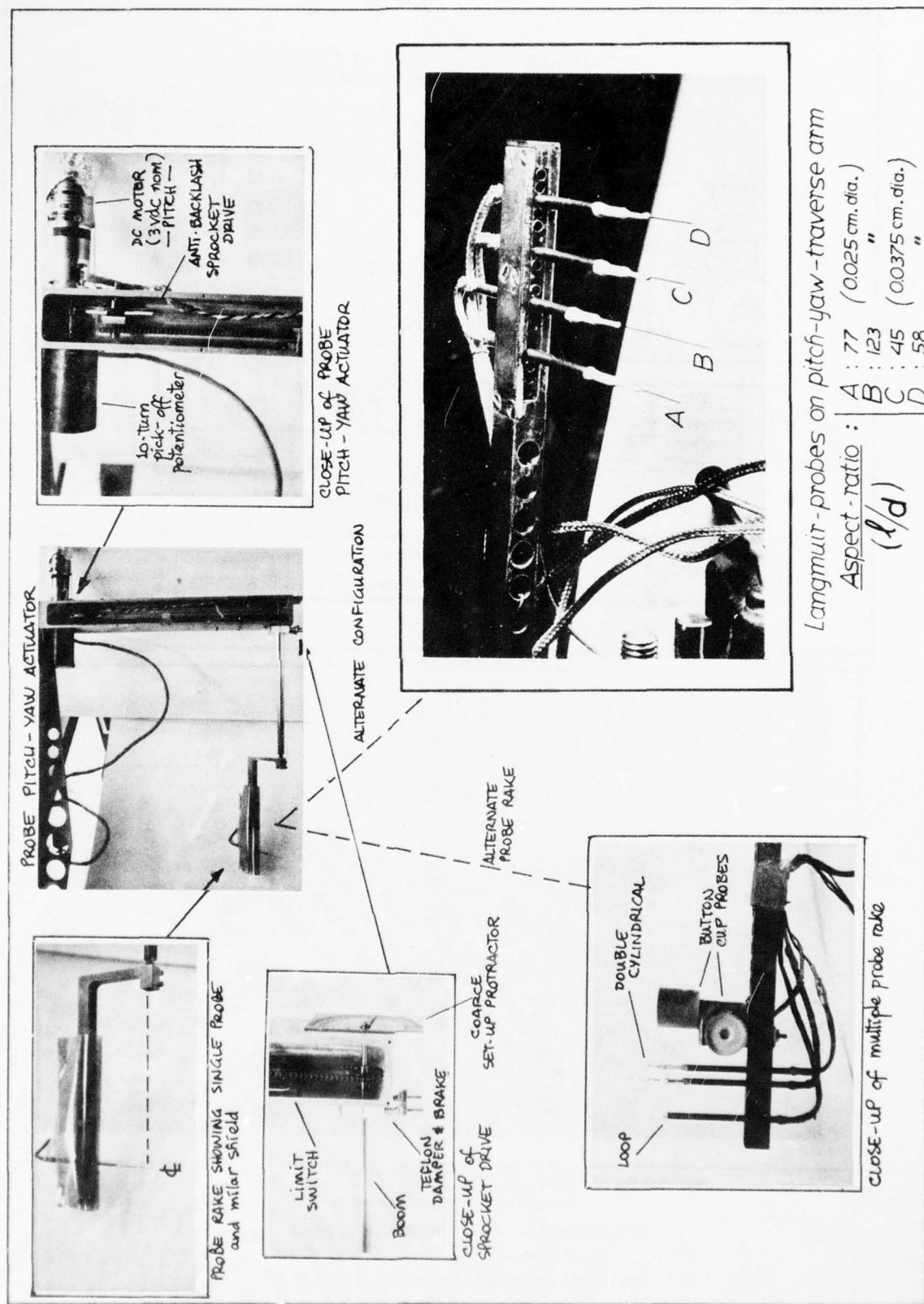
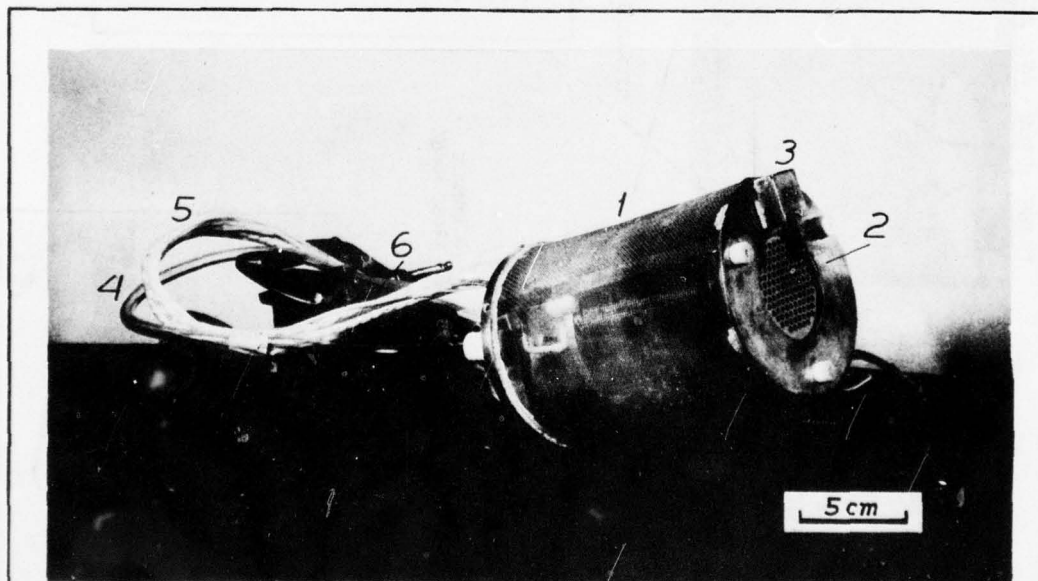
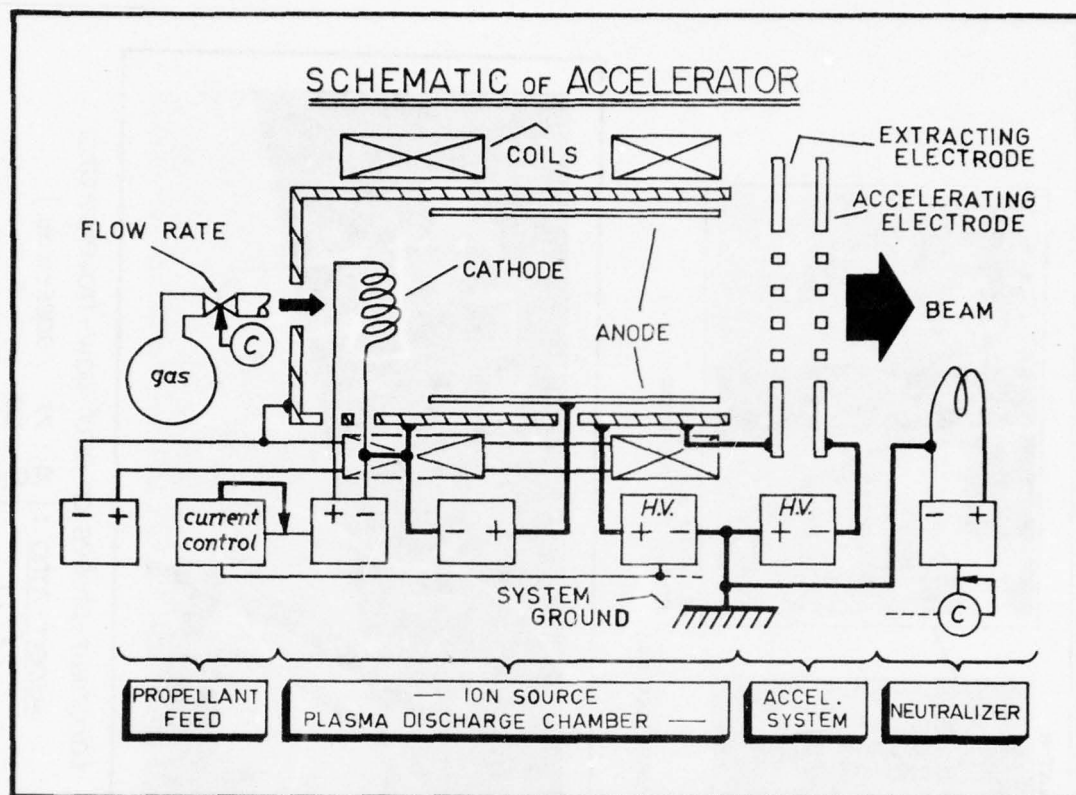


FIGURE II-3



ION ACCELERATOR:

- 1: body-shield — 2: accelerator plate —
- 3: neutralizer — 4: gas feed —
- 5: electrical connections — 6: mounting arm —

FIGURE II-4

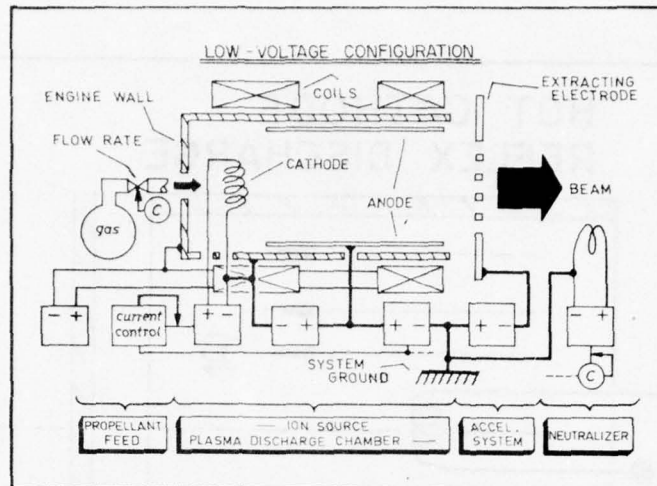


FIGURE II-5

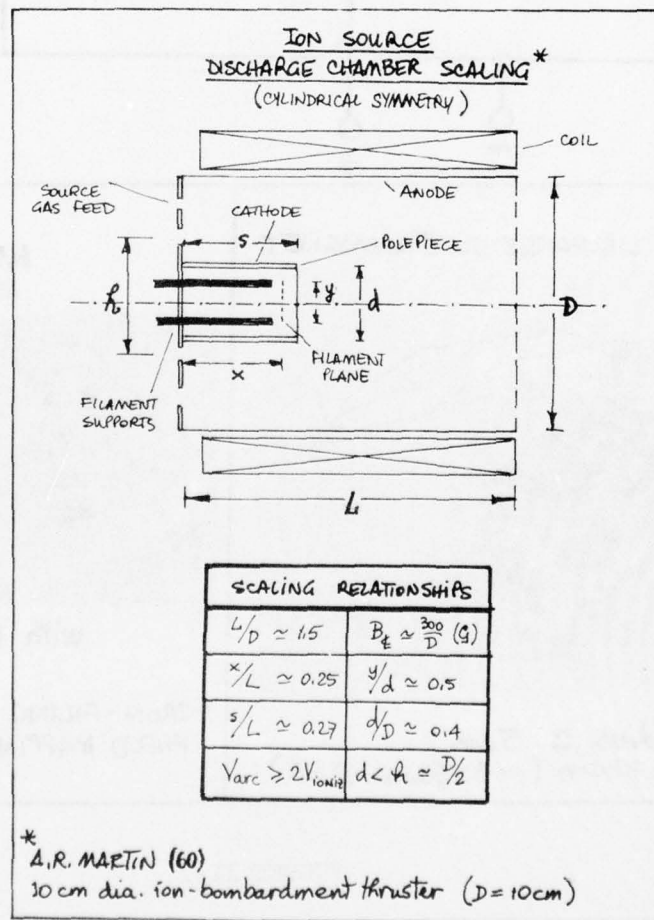
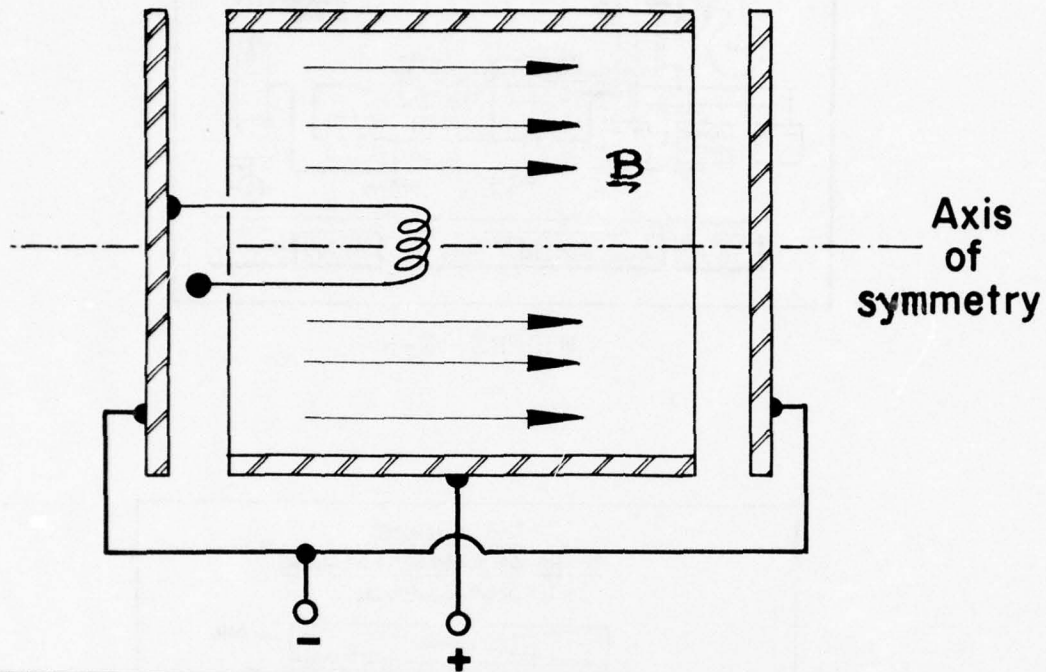
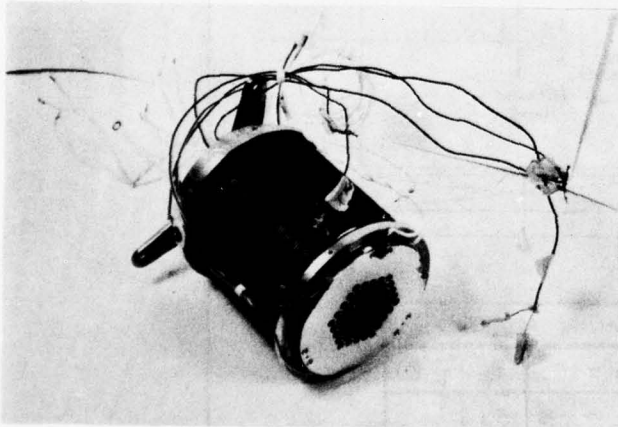


FIGURE II-6

HOT CATHODE REFLEX DISCHARGE

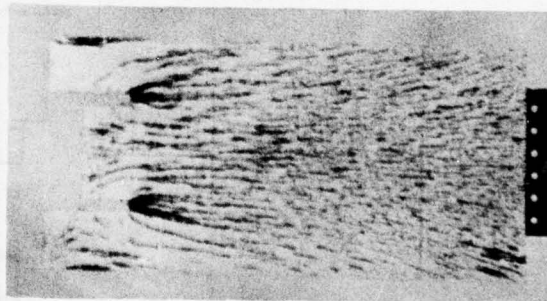


ION SOURCE DISCHARGE ELECTROMAGNET



coil mean radius ≈ 5 cm
coil length ≈ 10 cm (~ 30 Gauss @ 6A)

6.5A @ ~ 6 V
magnet

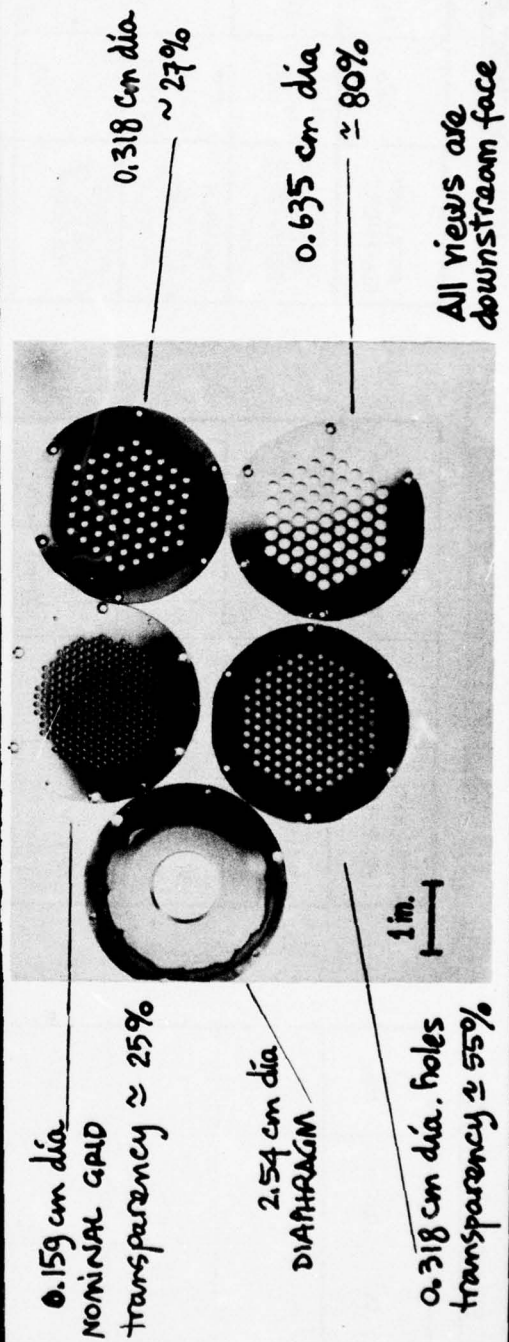
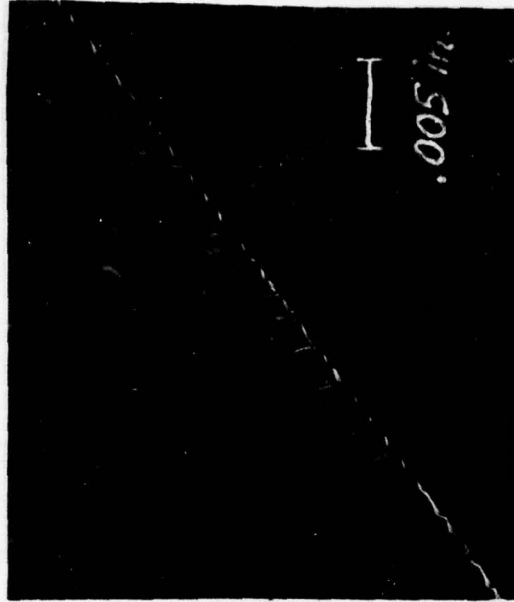
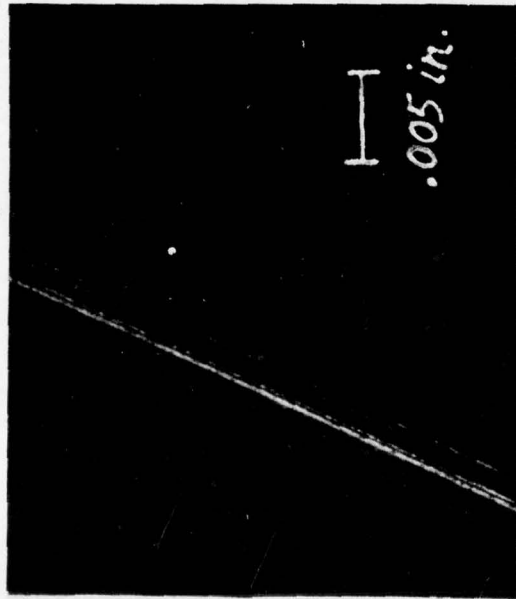


with POLE PIECE

IRON-FILING
FIELD MAPPING

FIGURE II-7

MICROSCOPE VIEW SHOWING SOURCE CATHODE FILAMENT DEGRADATION
 ~12 hours in Argon discharge; 0.008 in. W_g wire nominal



ACCELERATOR GRID GEOMETRY

PLASMA SOURCE FEATURES

PLASMA SOURCE FEATURES	Min	Typical	Max
DISCHARGE VOLTAGE V_D (volts)		50	
DISCHARGE CURRENT I_D (mA)	50	100	
BEAM CURRENT I_B (mA)	0.6	2	12.5
SOURCE FILAMENT LIFETIME (hours)		~30	
ENERGY COST per beam ion eV/ion	6000 (opt. 150)		41,000 (opt. 450)
BEAM TO DISCHARGE CURRENT RATIO		0.02	~0.08
BEAM TO FEED FLUX RATIO Γ_f/Γ_0		0.21	0.56 (stable)
NEUTRAL MASS FLOW IN (equivalent mA)	7.6 11.5mg/hr (IMP, Arnon)	9.5 (1.3uA/sec)	
SOURCE MAGNETIC FLUX DENSITY (gauss)		30-50	

ION ACCELERATOR FEATURES

ACCELERATOR FEATURES	Min	Typical	Max
BEAM ENERGY eV_B (eV)	60 low voltage mode		1800 high volt. mode
BEAM EXIT DIAMETER D_0 (cm)	2.5		5.0
ION MASS (Atomic #)		40 (Arnon)	
ACCELERATOR RATIO $\alpha = \frac{V_+}{V_+ + V_{-1}}$	0.5 (low volt.) (high volt.)	.70-.75	
BEAM SPREADING ANGLE γ (measured)	~10° small grid	14° large grid	
ACCELERATOR EXIT OPEN AREA	14%	~50%	
% MULTIPLE CHARGE IONS $++/+$		<5 (Ar ⁺⁺)	
NEUTRALIZER POWER SURFACE TEMP. (watt & °C)	2500°K	25-35	3300°K
TEMPERATURE ON ACCEL. COMPONENTS (°C)			700°K (anode)

TEST EQUIPMENT FEATURES

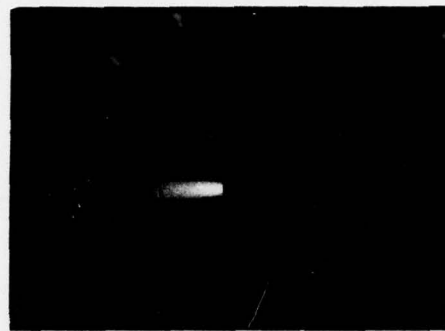
ANCILLARY EQUIPMENT	Min	Typical	Max
TEST SECTION PRESSURE P_0 (torr)	~2x10 ⁻⁶ (1m ² H ₂ trap)	2x10 ⁻⁵	8.5x10 ⁻⁵ max. operating time press.
CHAMBER operating PUMP SPEED (liter/sec)	(Arnon) ~1500 0.10 ⁻⁶ torr		(air) ~7000 0.35 ulin
PROBING DEGREES OF FREEDOM	3 (XYZ)	5 (XYZ) (pitch-vaw)	
PROBE RAKE SCANNING ANGLE	±15° (yaw)		±105° (pitch)
TEST SECTION (meters)	0	0.2-1.3	~3
DC POWER SUPPLY	15mA 0-2keV 1mA 0-11eV		10A 0-12V (3)
CIRCUITRY FREQUENCY RESPONSE (Hz)	10	30	~1000
SIGNAL PROCESSING SENSITIVITY		50mV/cm (±1%) (XY chart)	.05mV (±3%) (1-V converter)
*	—	—	—

FIGURE 11-9



NOTE 90° BURST-WINGS
due to severe arcing
and operation with no
neutralizer

(a)



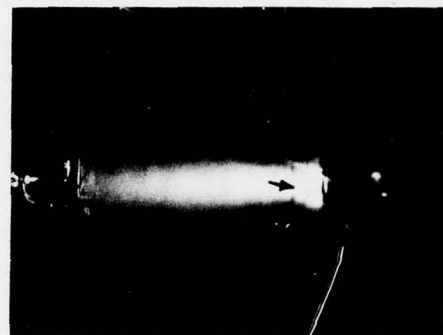
NOTE BEAMLET SEPARATION
@ EXIT PLANE
($d_{\text{HOLE}} \approx 0.318 \text{ cm}$)

(b)



LOW VOLTAGE CONFIGURATION
large grid (spreading angle $\approx 0^\circ$)
100 V @ 5 mA beam
 $5 \times 10^{-5} \text{ torr}$

(c)



Severe arcing @ exit
large grids
1000 V @ 2 mA beam
test section $\approx 7.5 \times 10^{-5} \text{ torr}$

(d)



small grids (2.54 cm exit dia)
1000 V @ 2 mA NOMINAL CONFIGURATION
spreading angle $\approx 10^\circ$ (half-angle)
 $3 \times 10^{-5} \text{ torr}$

(e)



large grids (5.08 cm exit dia)
1000 V @ 2 mA NOMINAL CONFIGURATION
spreading angle $\approx 14^\circ$ (half-angle)
 $3 \times 10^{-5} \text{ torr}$
BUTTON PROBES

(f)

FIGURE II-10

REPERTORY OF CYLINDRICAL PROBES *

PROBE DIAMETER (cm)	0.010	0.0127 #	0.020	0.0254	0.0381	0.0508
NOMINAL PROBE LENGTH (cm)	R +	R	R	R	R	R
0.75	72.0					
1.0	115.5					
1.5			76.2		44.2	21.6
2.0	172.5			76.7	57.3	
2.5	221.3		124.6			
3.0		2.46				
3.5			174.8			
4.0				164.0		
4.5			219.5	172.4		
5.0	472.5					

+ MEASURED PROBE ASPECT RATIO (l/d)
 * TUNGSTEN UNLESS OTHERWISE MENTIONED
 # TANTALUM

FIGURE II-11a)

LOG OF RUNS

EXIT BEAM DIAMETER: $2r_0 = 2.54\text{cm}$
AXIAL POSITION: $Z/r_0 = 40 - 90$

BEAM ENERGY (current)	PROBE DIAMETER (in/cm)				PROBE ASPECT RATIO
	0.0102 (0.004)	0.0204 (0.008)	0.0254 (0.010)	0.0508 (0.020)	
50-150 (current) + 300 (20mA) 150-450 (variable) +					
	Λ0L-1/Λ0L-2				172
500 (20mA)				Λ37-V	22
	Λ0L-2				172
500 (20mA)	*				22
	Λ09	Λ17/Λ17-V	Λ20		175
700 (20mA)	Λ03-2				472
				Λ33-1	22
700 (20mA)	Λ09-2	Λ16/Λ16-V	Λ24		175
	Λ02 *				472
1000 (300-1200) (20mA)					
	Λ03-1 *	Λ19	Λ22		175
	Λ03-1				472

★ R = 172
R = 164
+ LOW VOLTAGE MODE

FIGURE II-11b)

CONSTRUCTION SCHEMATIC OF
LARGE ASPECT-RATIO (l/d)
CYLINDRICAL LANGMUIR PROBE

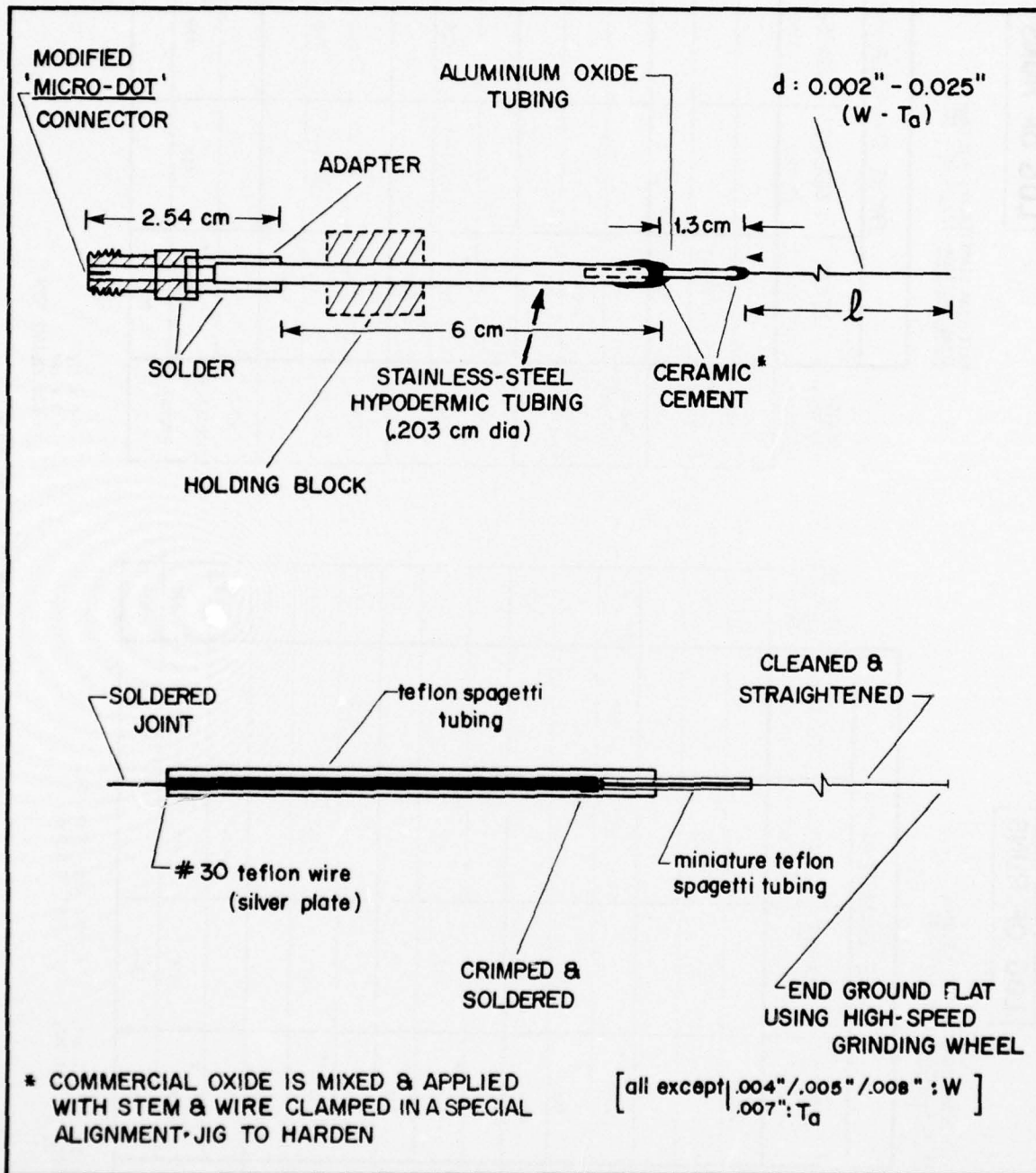
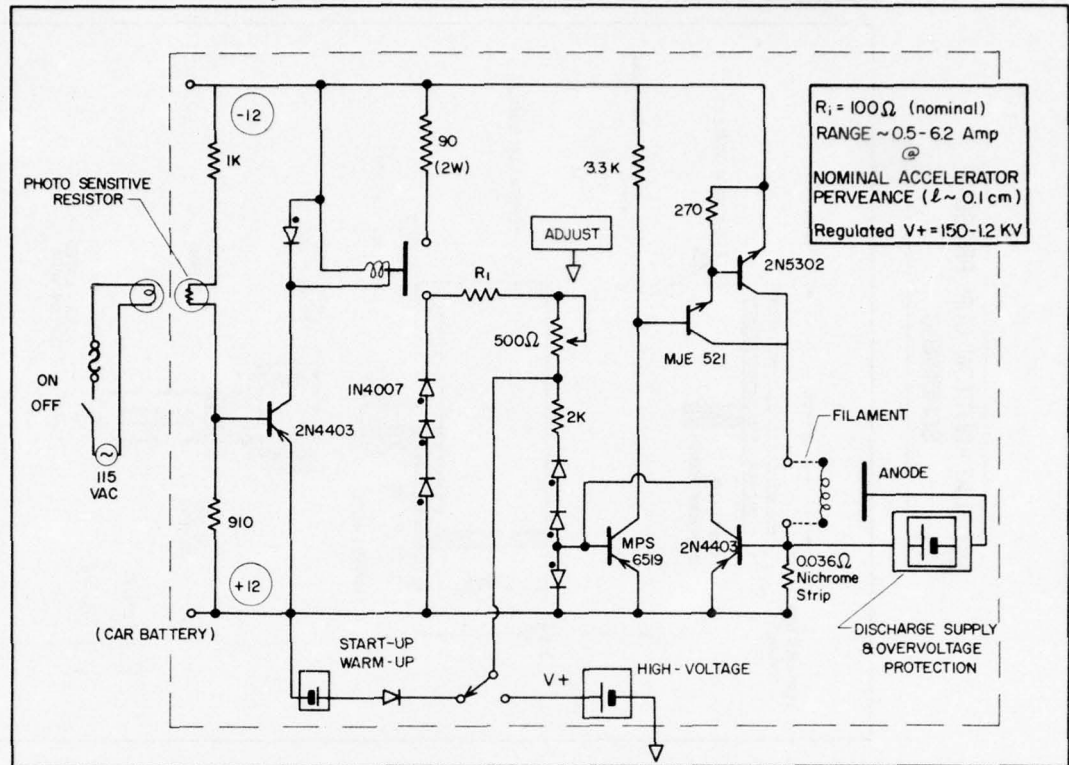


FIGURE II-12

a) SOURCE-FILAMENT CURRENT REGULATOR



b) PITCH & YAW ANALOG PROBE SCAN CIRCUITRY

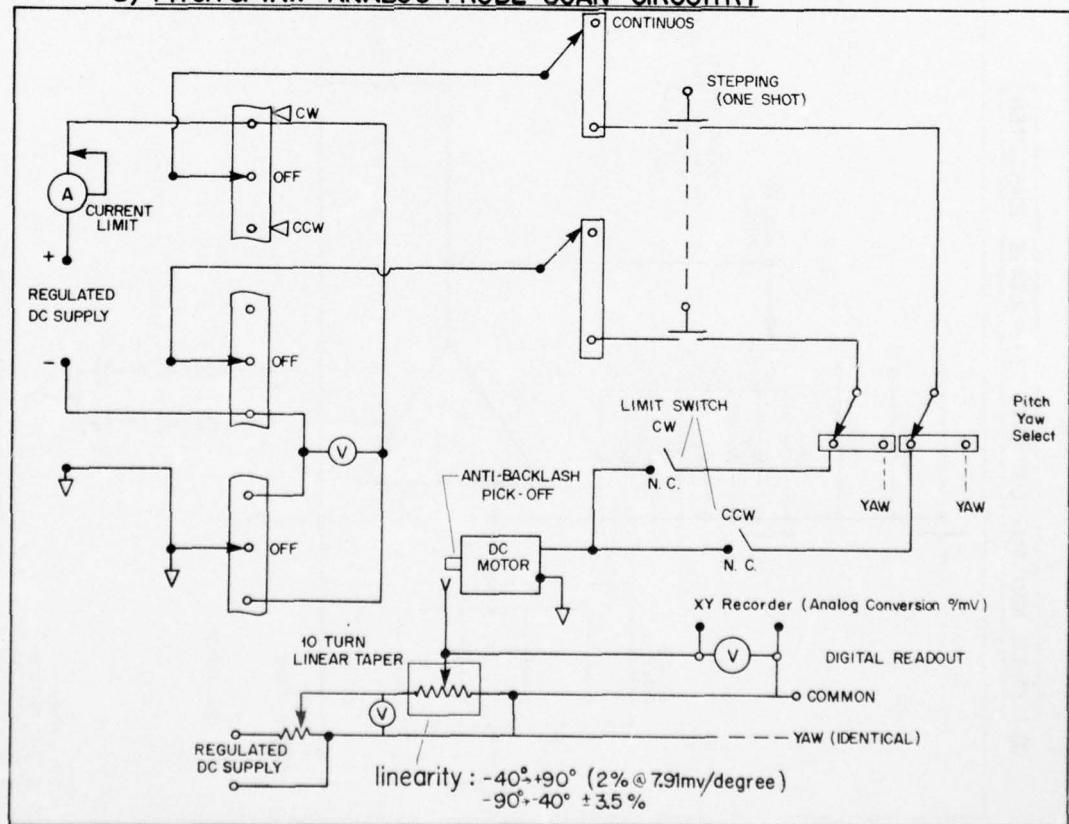


FIGURE II-13a), b)

1%
10%
100%

1mA

1uA

1nA

RAISE SWITCH

1M Ω (select)
@ 1 volt out full-scale
 $\pm 1.5\%$ F.S.
 ± 0.5 @ 10^{-5} A, $1/10$ F.S.

OP-27
AMP

trim

1M Ω
(typical)

o/n

9V

0.5 μ F

REF. GROUND

BIAS (floating)

0
-9
-18
+9

$C_S = 300\text{pF}$

1% resistor
0.5 μ F resistor
FREQUENCY RESPONSE: $(2\pi RC_C)^{-1} = 1.3\text{GHz}$ (typ)
PHILDORCK 1023: low drift; temperature stability $\pm 1.0\%$ $^{\circ}\text{C}$ $^{-1}$

Technical drawing of a flat-button probe assembly, showing a side view and a cross-sectional view.

Side View (Left):

- Probe length: 2.54 cm
- Probe diameter: 1.27 cm
- Connector soldering point is indicated.
- View angle: 60°

Cross-sectional View (Right):

- Probe diameter: 1.27 cm
- Probe length: 2.54 cm
- Internal components: Teflon cup-shield, mounting surface, pumping hole, mounting thread & nut, shrinkable tubing, Teflon sleeve, silver plated Teflon wire.
- View angle: 45°

Legend:

- TEFLON (hatched pattern)
- COPPER (cross-hatched pattern)

FIGURE II-14a), b)

AD-A033 836

TORONTO UNIV (ONTARIO) INST FOR AEROSPACE STUDIES

F/6 20/9

ION TEMPERATURE MEASUREMENT IN A FLOWING COLLISIONLESS PLASMA U--ETC(U)

JUL 76 H P MERCURE

AF-AFOSR-2091-71

UNCLASSIFIED

UTIAS-202

AFOSR-TR-76-1411

NL

2 OF 2

AD
A033836



END

DATE
FILMED

2-77

ION BEAM GEOMETRICAL MODEL
SYNTHETIC TEMPERATURE CONCEPT

The diagram illustrates the geometry of an ion beam and the concept of synthetic temperature. Key components and labels include:

- IDEAL SOURCE-FLOW VIRTUAL ORIGIN**: The point from which the beam appears to originate.
- Z**: The axial coordinate along the beam's path.
- BEAM EDGE**: The outer boundary of the ion beam.
- BEAM RADIUS**: The radius of the beam at a given distance.
- GEOMETRIC CENTRE - LINE**: The central axis of the beam.
- DIVERGENCE ANGLE**: The angle γ between the beam edge and the central axis.
- BEAM EXIT PLANE**: The plane where the beam enters the probe region.
- DISCRETE BEAMLET EMITTING SOURCES**: Small sources ΔS_k within the beam.
- (CYLINDRICAL SYMMETRY)**: The assumption of symmetry around the central axis.
- PROBE ORIENTATION @ $(Z+Z_0)$** : A circular inset showing the probe's orientation at a distance $Z+Z_0$ from the virtual origin. The probe is a rectangular plate of length l and width ϵ , oriented at an angle θ to the central axis.
- PROBE**: The detector used to measure the beam's properties.
- TRANSVERSE VELOCITY**: The velocity component $V_k = U_k \sin \theta$ perpendicular to the beam's path.
- SYNTHETIC SPEED RATIO**: The ratio $S_{i_{geo}} \sim \frac{Z}{l_0}$, where l_0 is the probe length.

FIGURE III-1

FIGURE III-2

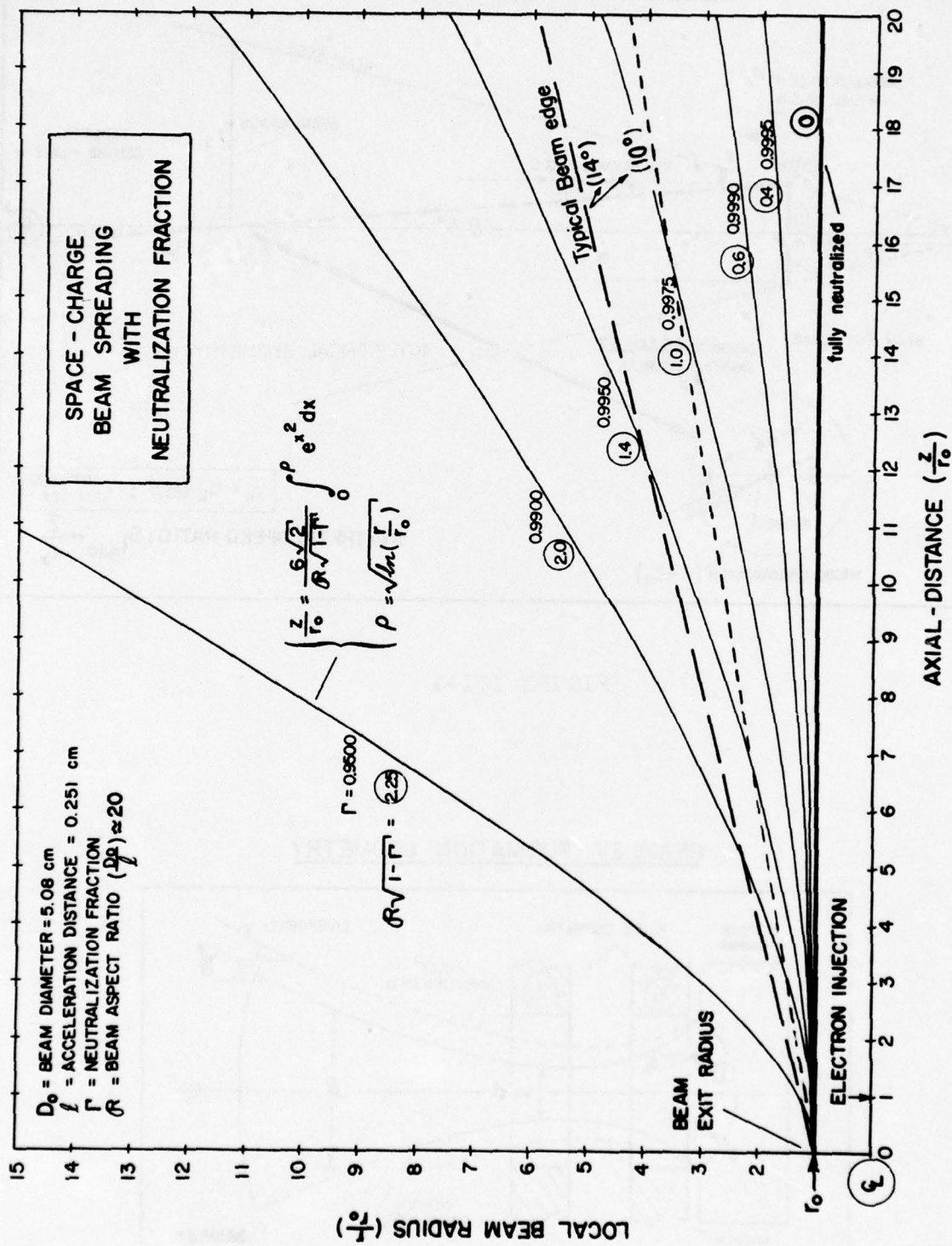


FIGURE III-3

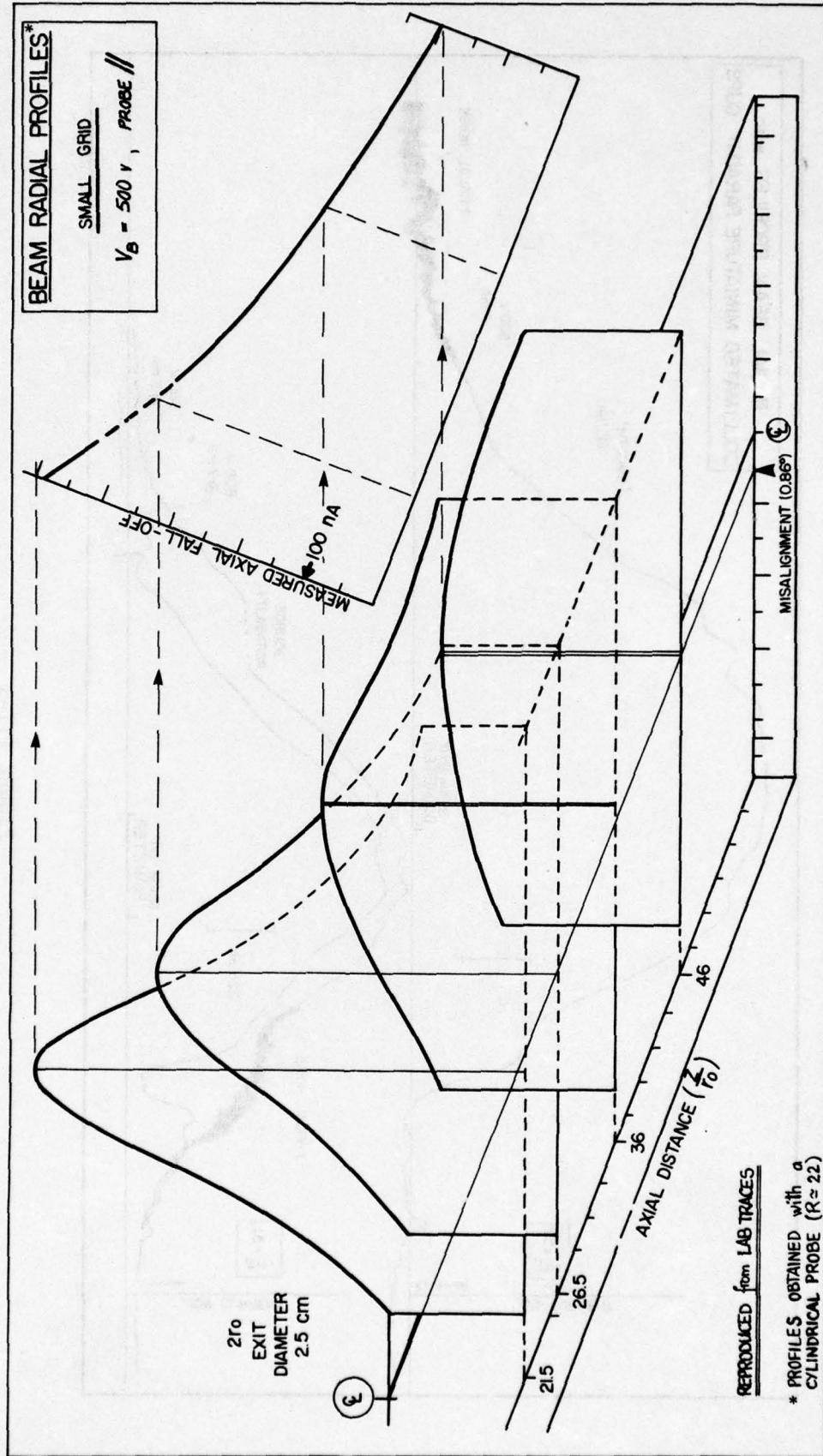


FIGURE III-4

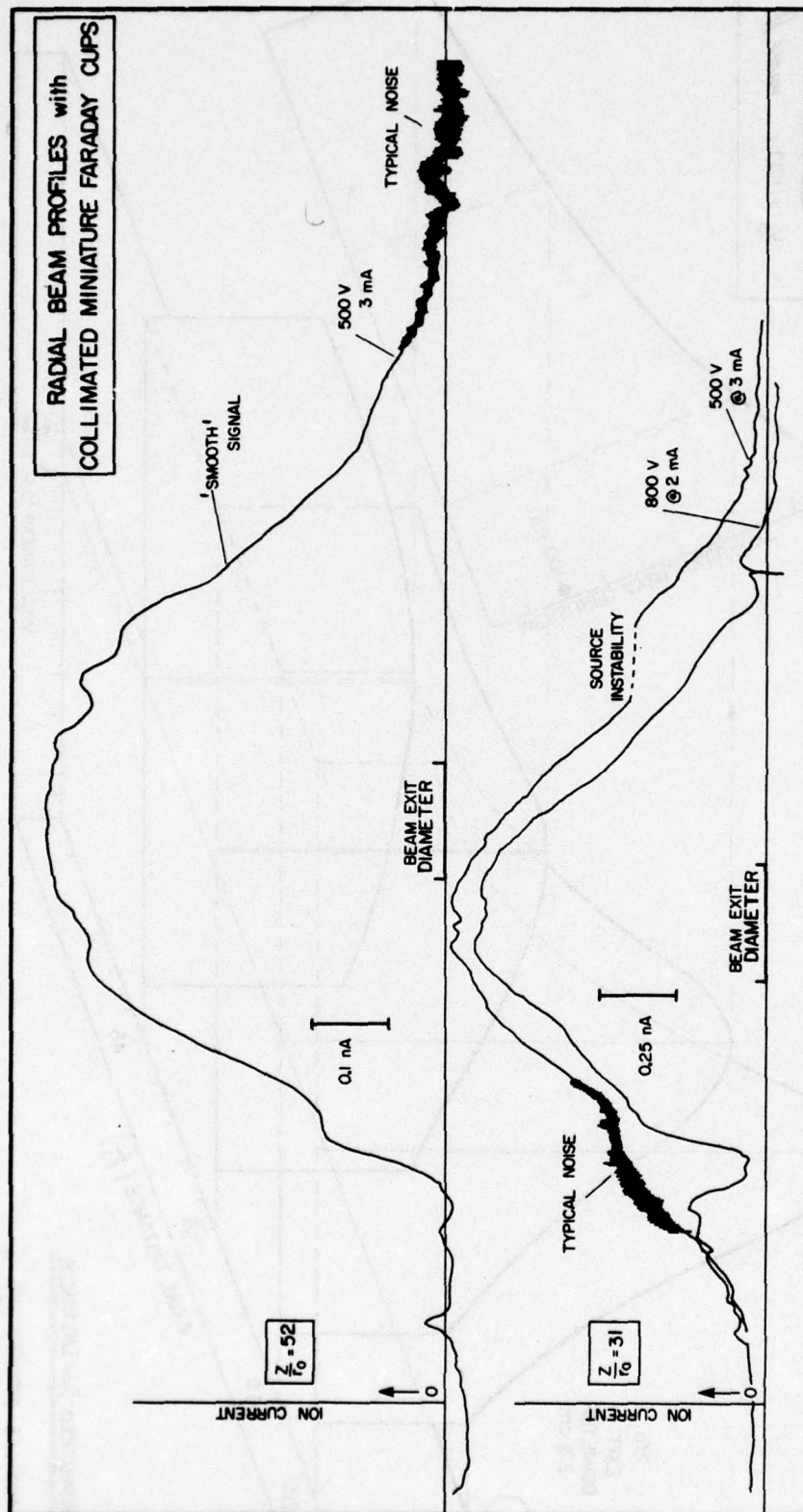


FIGURE III-5

NORMALIZED RADIAL DENSITY PROFILE
from MEASURED RADIAL TRAVERSES
(Gaussian envelope model)

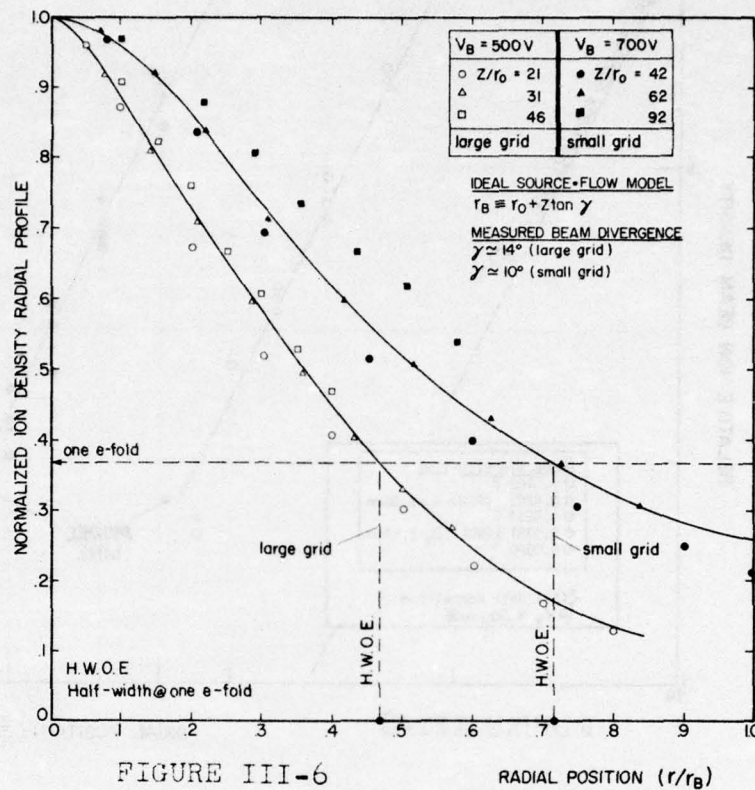


FIGURE III-6

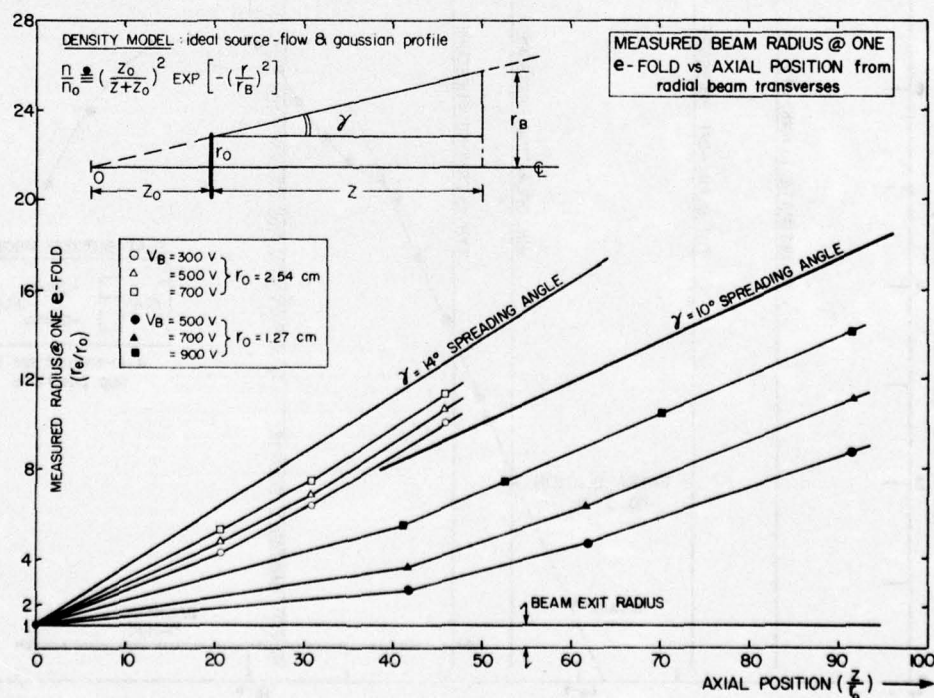


FIGURE III-7

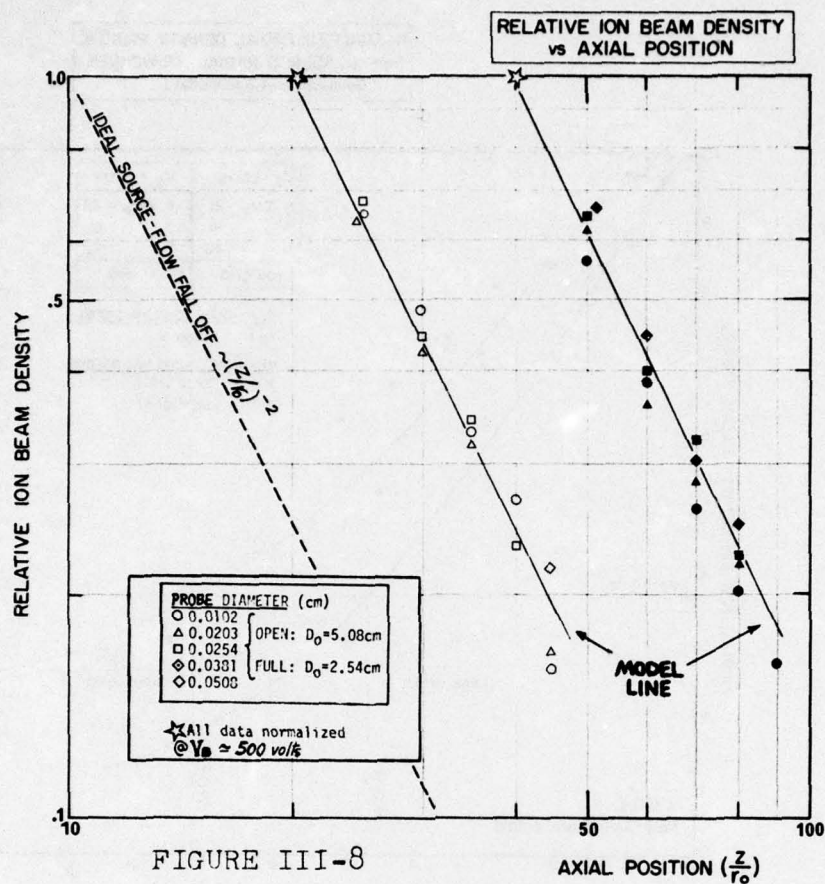


FIGURE III-8

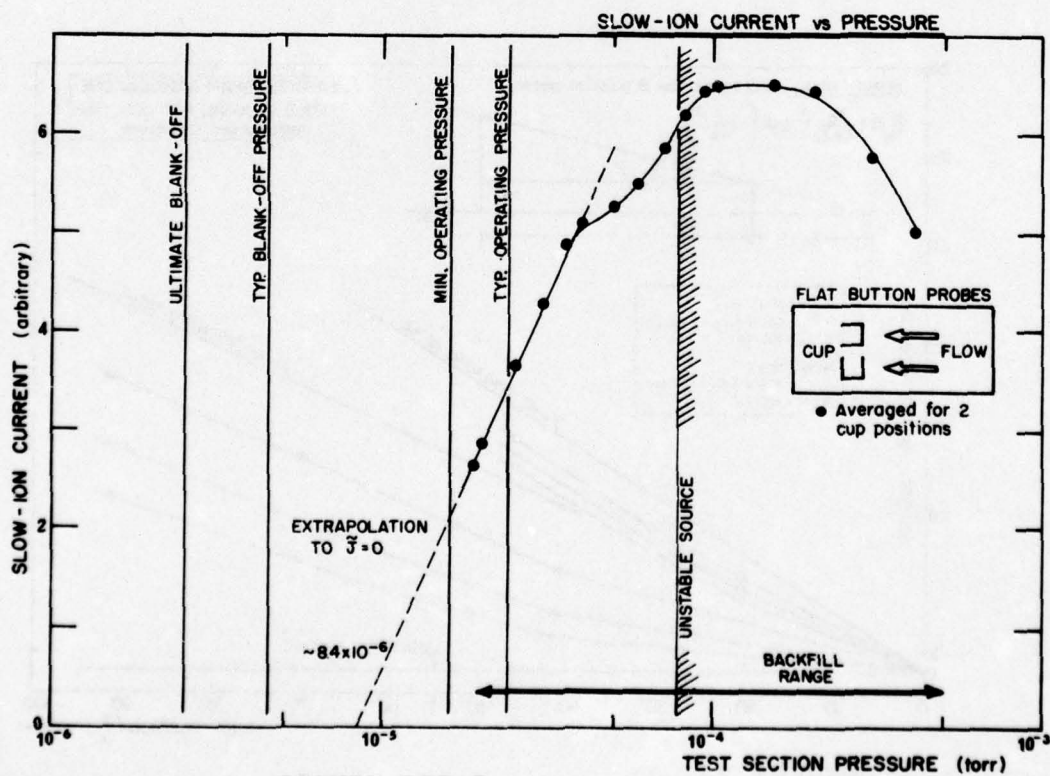


FIGURE III-9

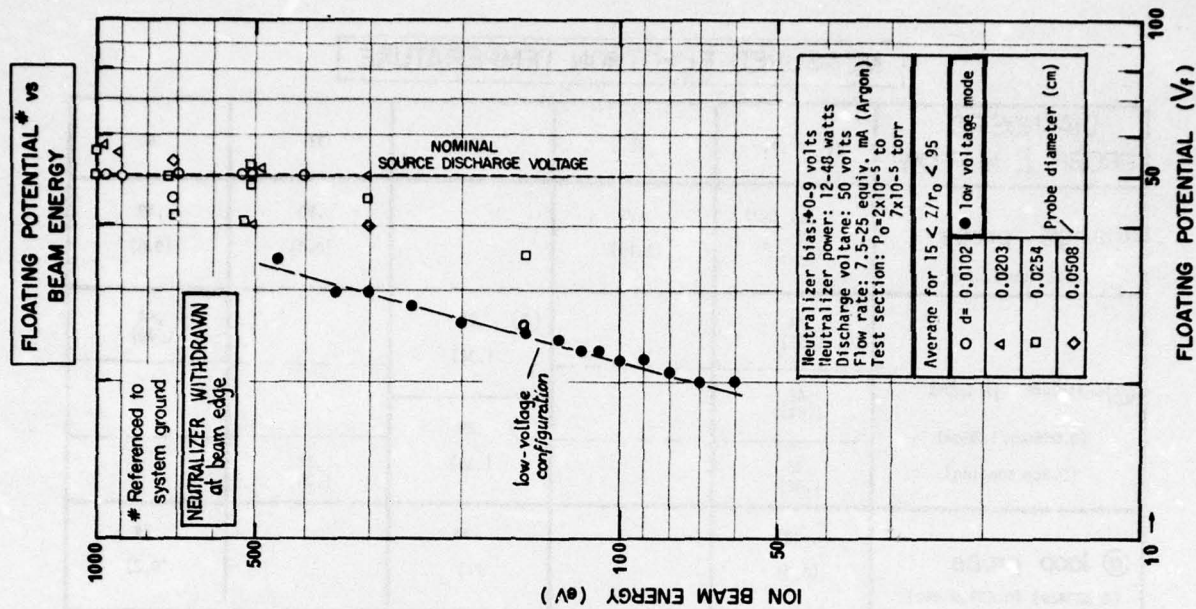


FIGURE III-11

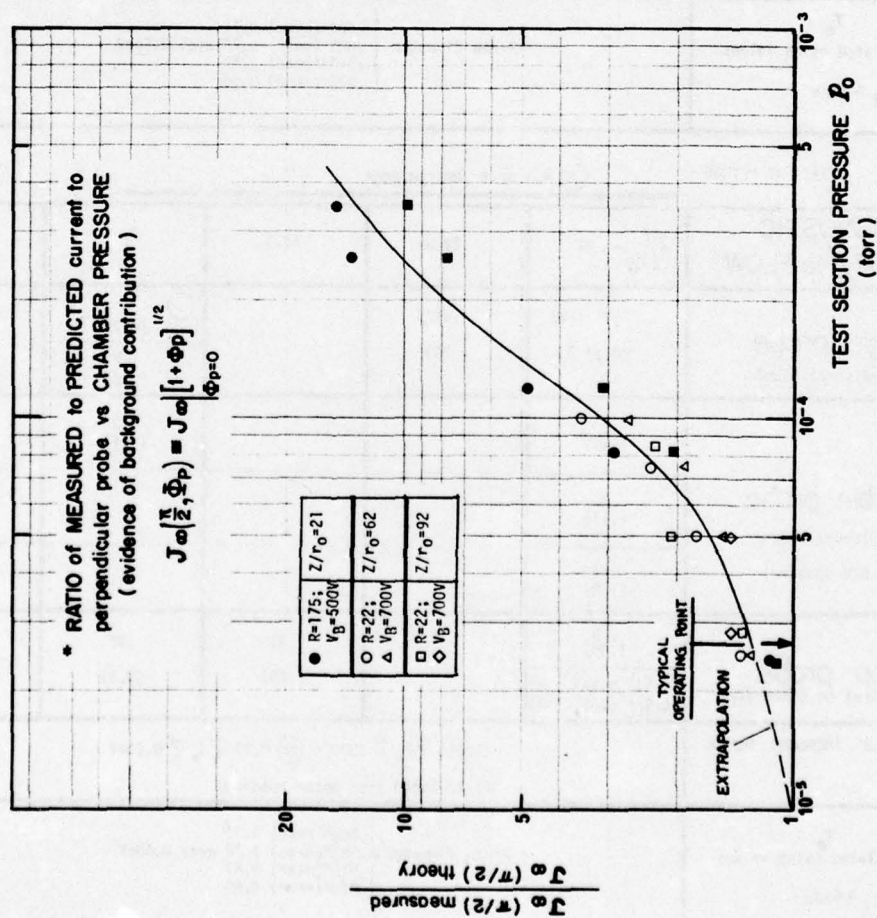


FIGURE III-10

MEASURED ELECTRON TEMPERATURE

DIAGNOSTIC PROBE \perp to FLOW	$z/r_0 = 21$	22.5	23.5	31	46
⊙ single probe (0.0254cm/1.80cm)	.65 (eV) (1.0) #	.73 (1.15)		.60 (0.8)	.50 (0.6)
⊙ double probe (0.0254cm/1.80cm) (0.8cm spacing)	.44 (.50)		② .28 (.32)		.44 (.40)
	.48 (.64)		② .29 (.35)		
	.46 (.42)			.35 (.36)	
⊙ loop probe (0.0254cm) (0.635cm dia)	.33 (0.3)		.38 (-)		.24 (0.2)
neutralizer filament temp. (T_w)	2500°K $\lesssim T_w \lesssim 3300^\circ\text{K}$ (or) $0.21 \lesssim T_w \lesssim 0.28\text{eV}$ (calculated from meter reading)				
T_e calculated using values of $n_{i\perp}$ & ϵ_{\min}	* Probe diameter $\begin{cases} .004''(\text{mean}) & 0.71 \\ .008''(\text{mean}) & 0.76 \text{ ave: } 0.66\text{eV} \\ .010''(\text{mean}) & 0.57 \\ .020''(\text{mean}) & 0.60 \end{cases}$				

() TANGENT METHOD

② Run AE-5 .004"/0.690"

DIAGNOSTIC PROBE \parallel to FLOW	$z/r_0 = 21$	22.5	23.5	31	46
⊙ single probe (0.0254cm/1.80cm)	.71 (eV) (0.7) #	.62 (.75)		① - (0.7)	.60 (0.4)
⊙ double probe (0.0254cm/1.80cm) (0.8cm spacing)	.54 (.65)			.43 (.44)	.41 (-)
	.36 (.42)				
	.46 (.38)				
⊙ loop probe (0.0254cm) (0.635cm dia)	.38 (.30)		.35 (.25)	.35 (0.3)	.28 (0.3)
	0.37 (.5) 0.34 (.3) 0.32 (.4) ③				
neutralizer filament temp.	2500°K $\lesssim T_w \lesssim 3300^\circ\text{K}$ (or) $0.21 \lesssim T_w \lesssim 0.28\text{eV}$ (calculated from meter reading)				
T_e calculated using values of $n_{i\perp}$ & ϵ_{\min}	* Probe diameter $\begin{cases} .004''(\text{mean}) & 0.71 \\ .008''(\text{mean}) & 0.76 \text{ ave: } 0.66\text{eV} \\ .010''(\text{mean}) & 0.57 \\ .020''(\text{mean}) & 0.60 \end{cases}$				

() TANGENT METHOD

① Run A36-1 .004"/.288"

③ Radial traverse T_e on \mathcal{C} 2r_B, 3r_B, 4.5r_B.

FIGURE III-12

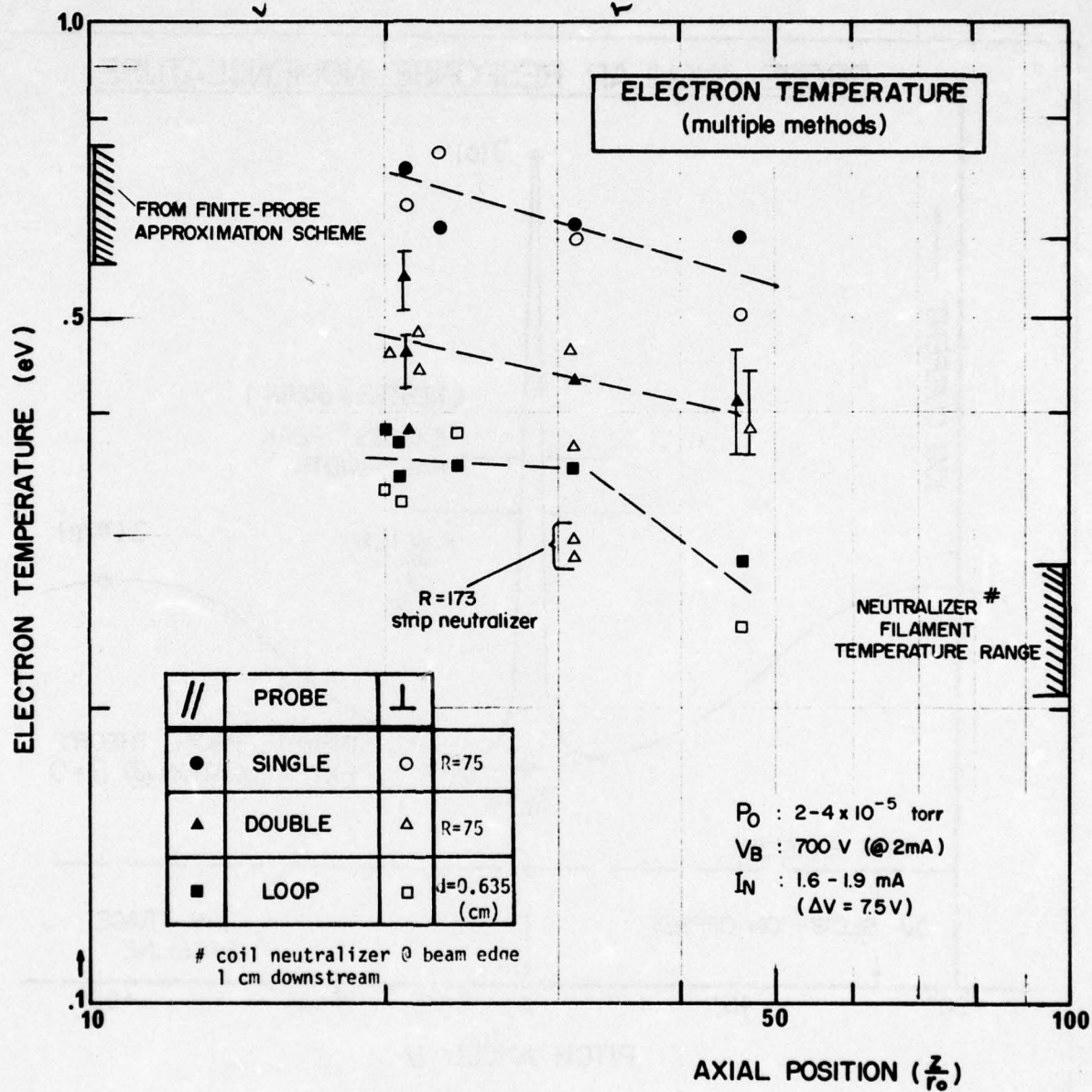


FIGURE III-13

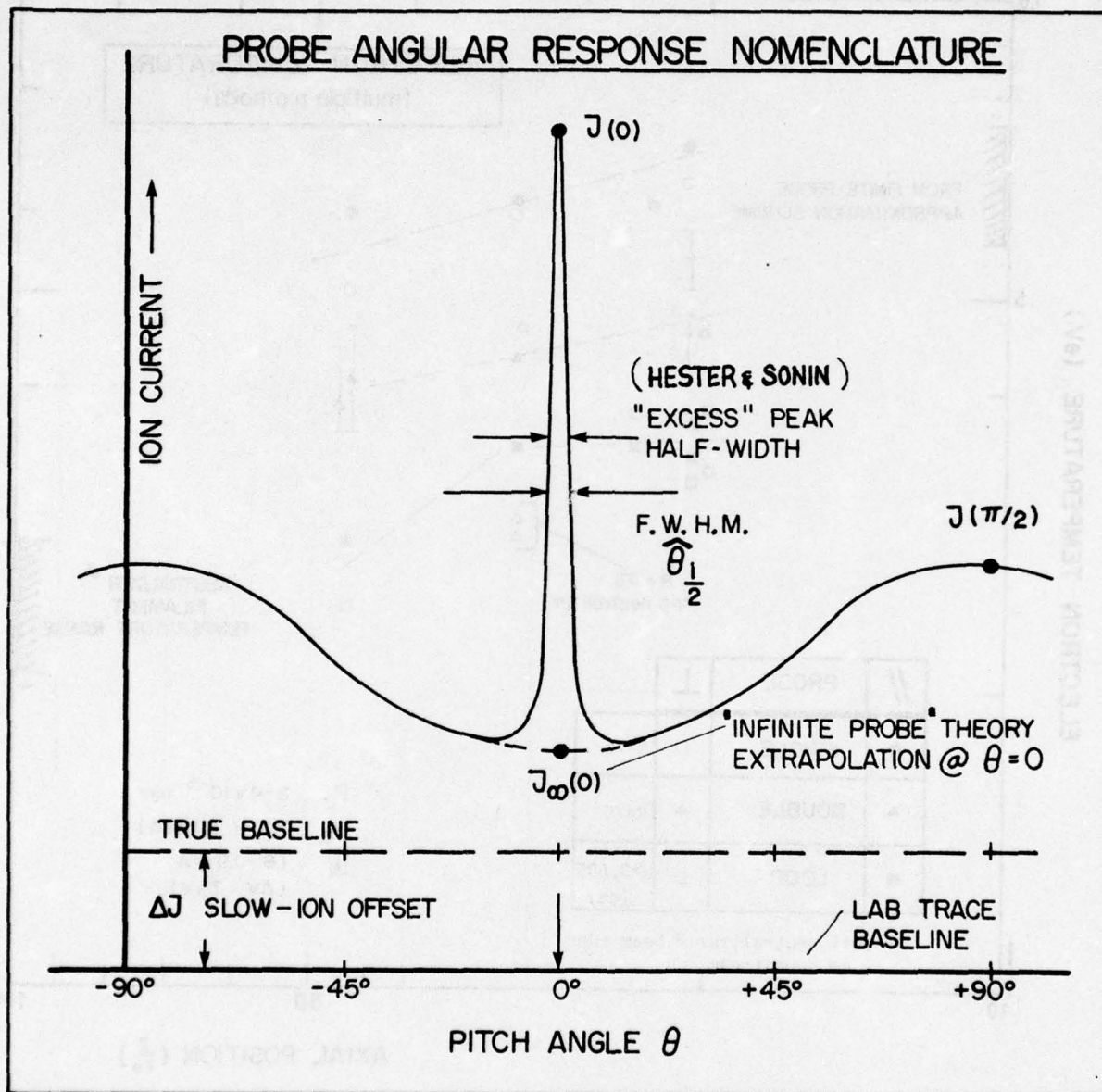


FIGURE IV-1

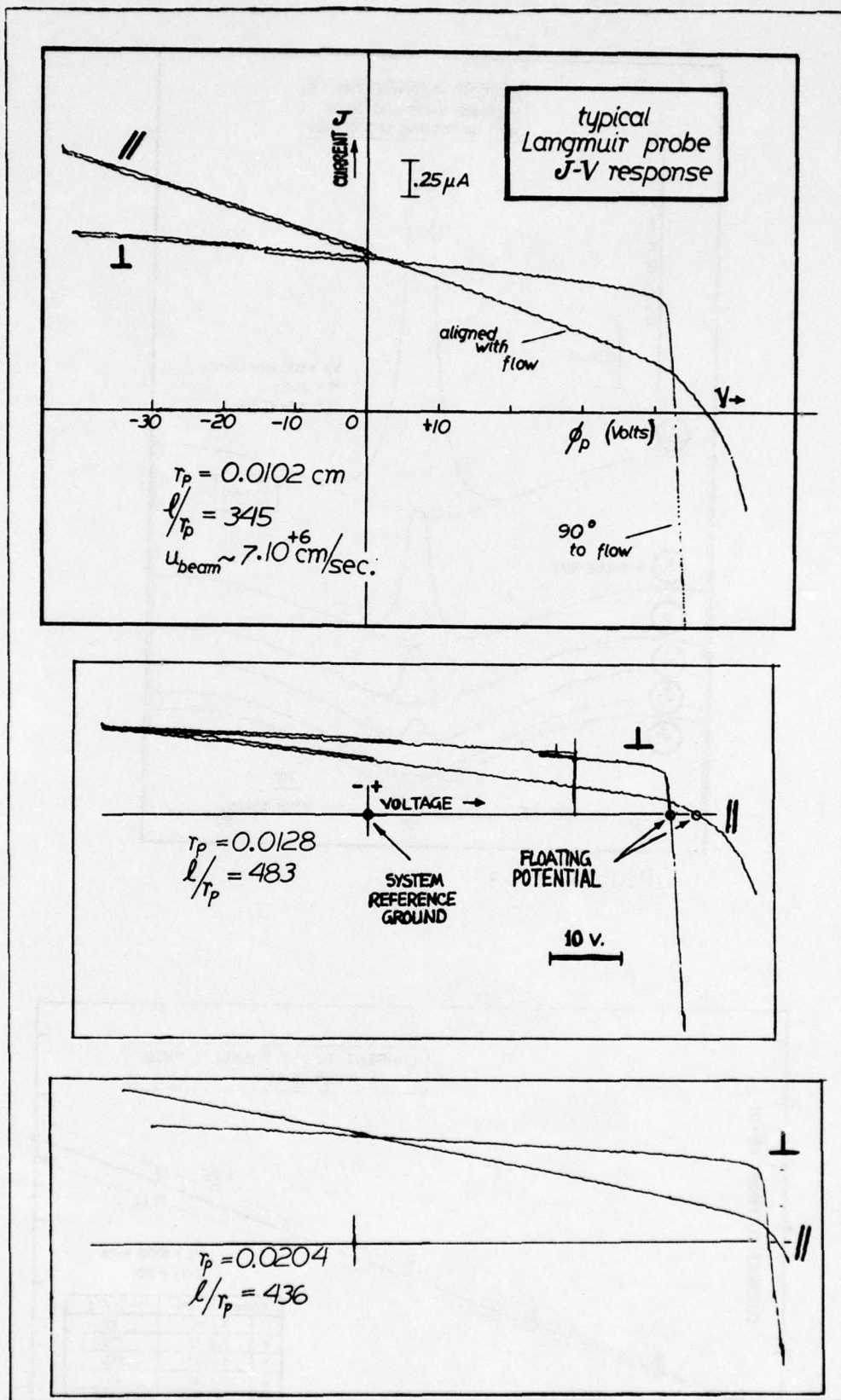


FIGURE IV-2

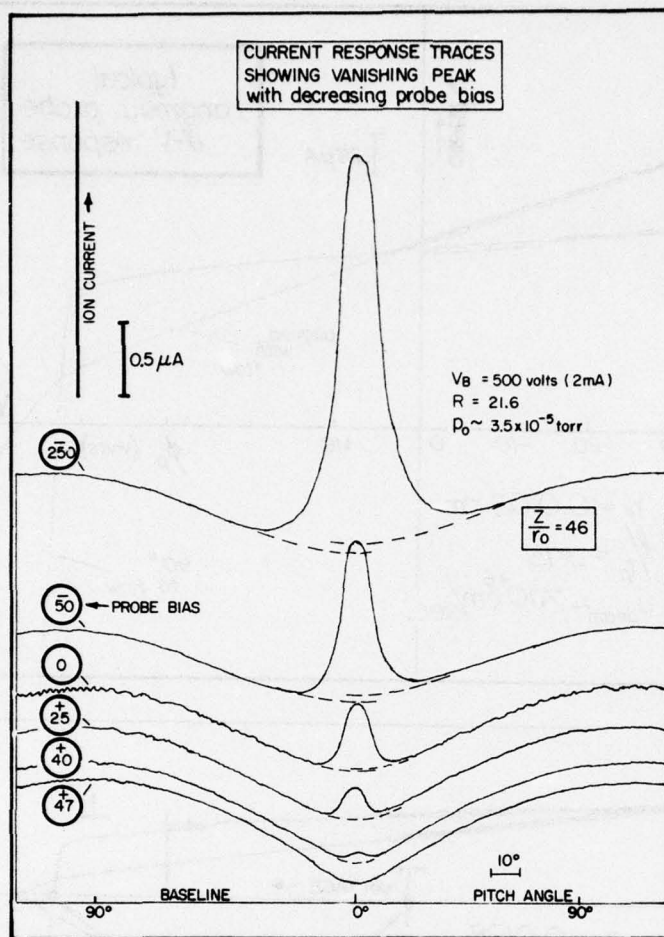


FIGURE IV-3

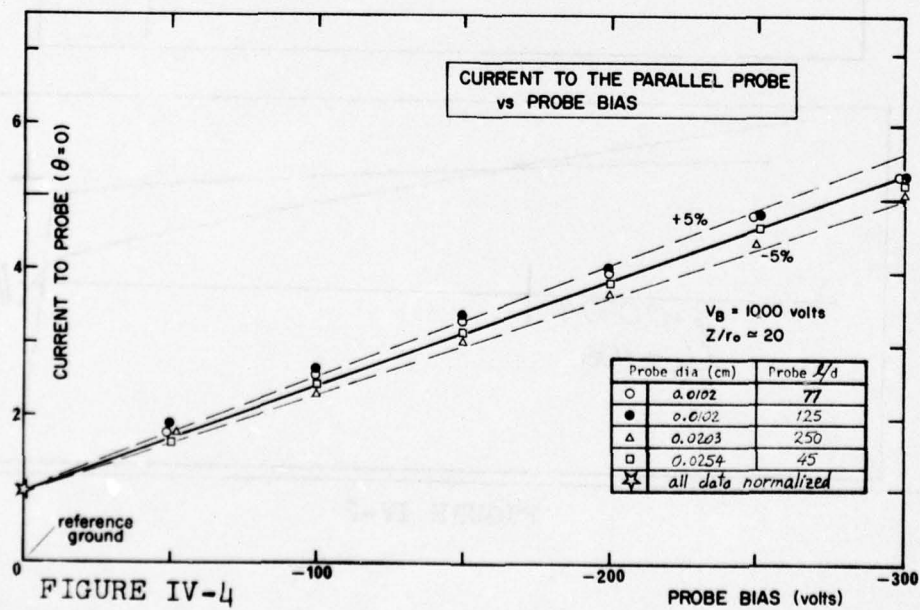
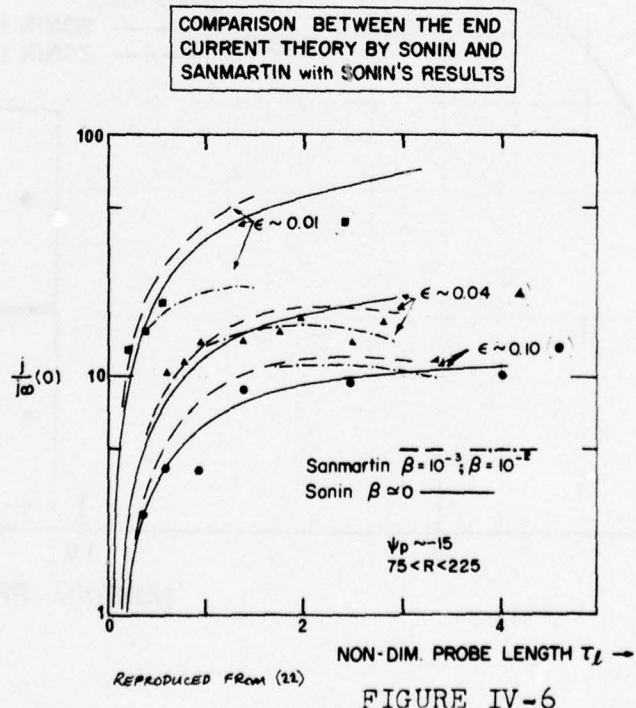
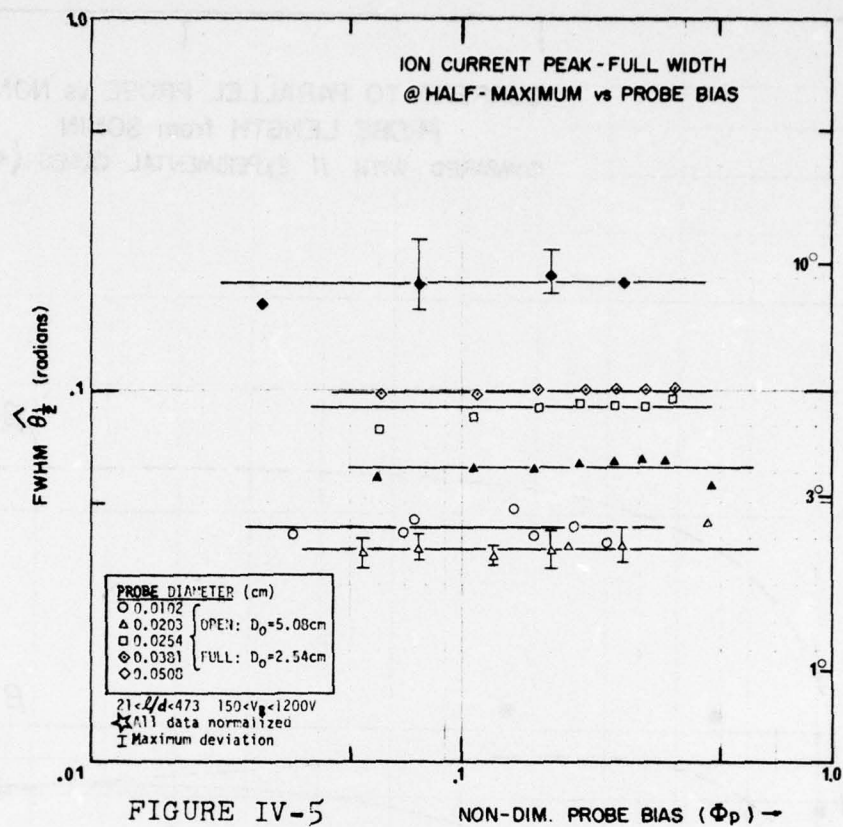


FIGURE IV-4



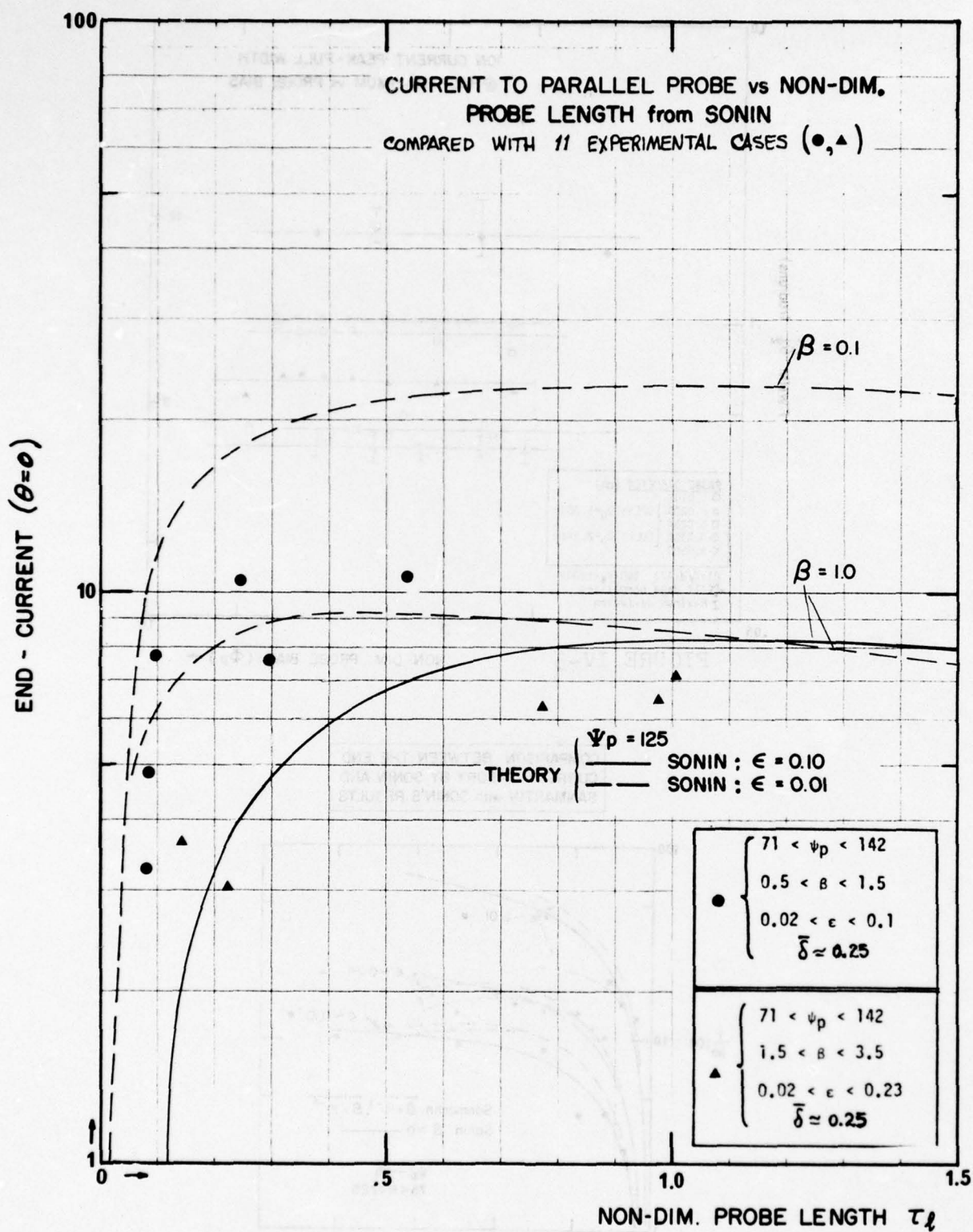
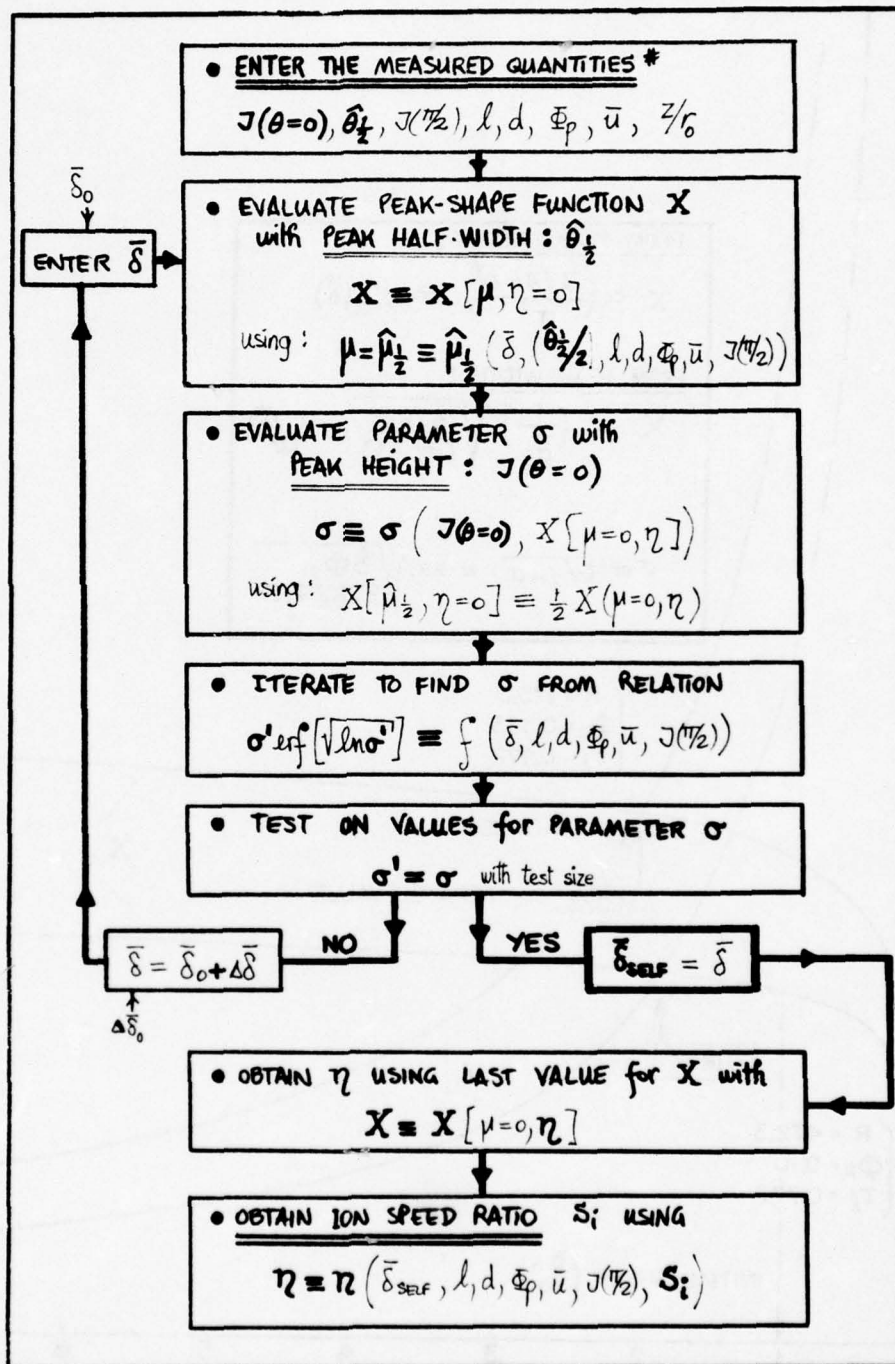


FIGURE IV-7

FLOW-CHART TO DETERMINE THE ION SPEED RATIO :

SELF-CONSISTENT SOLUTION FOR $\bar{\delta}$
 USING ION SPEED RATIO SENSITIVITY
 OF PEAK HEIGHT (CURRENT @ $\theta=0$) and
 PEAK HALF-WIDTH SIMULTANEOUSLY



* ALL ANALYTICAL RELATIONS OBTAINED FROM Ref. 18

FIGURE IV-8

A GEOMETRICAL REPRESENTATION OF THE
SELF-CONSISTENT SOLUTION FOR δ

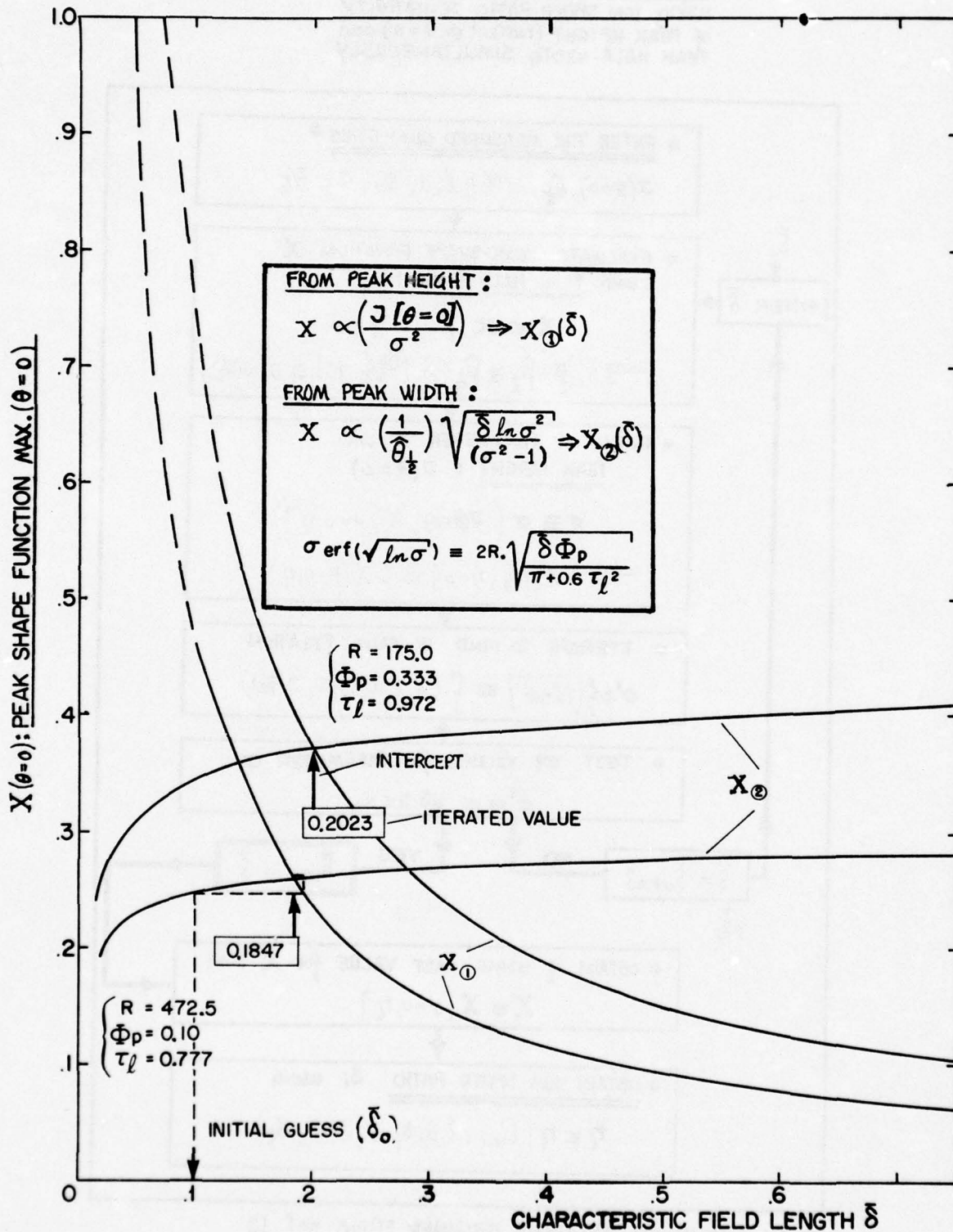


FIGURE IV-9

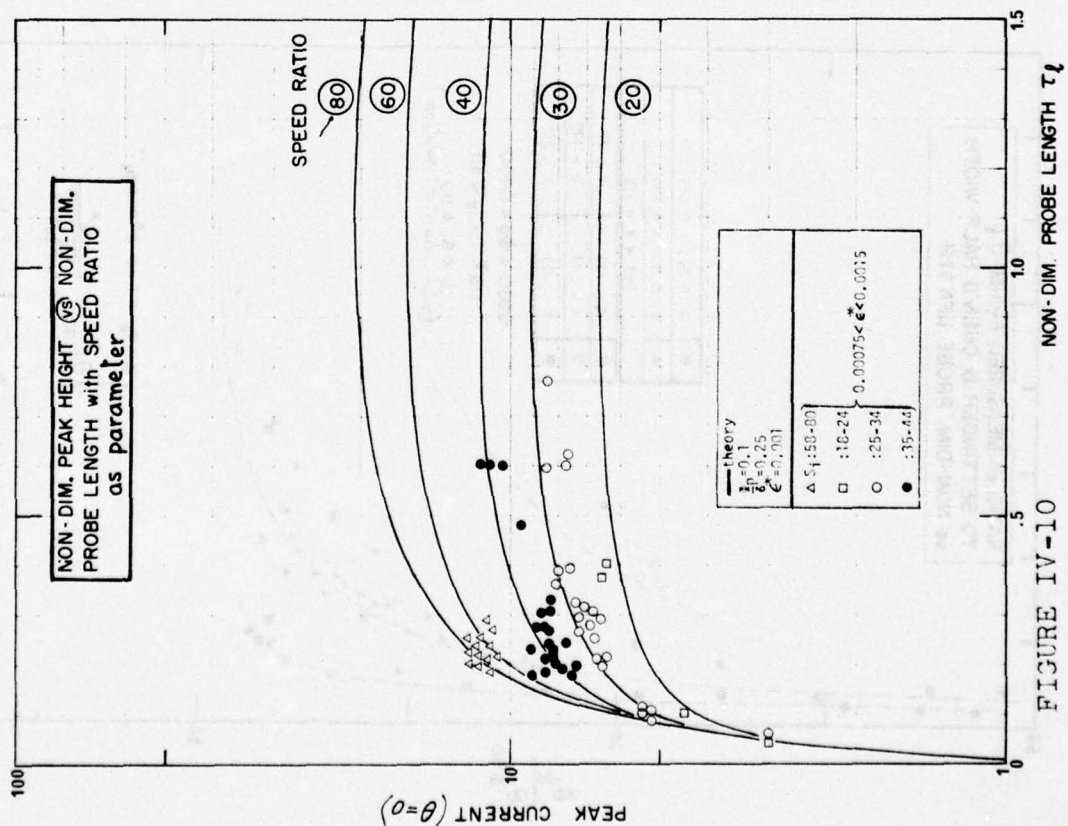


FIGURE IV-10

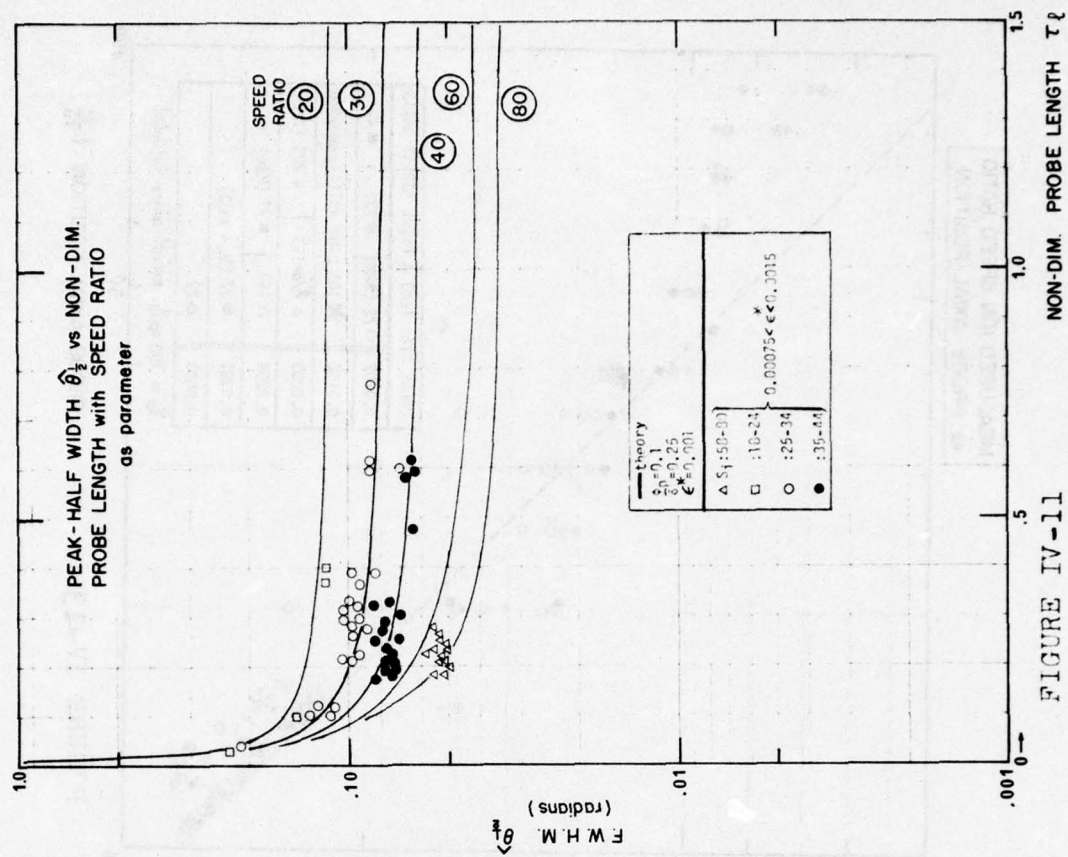


FIGURE IV-11

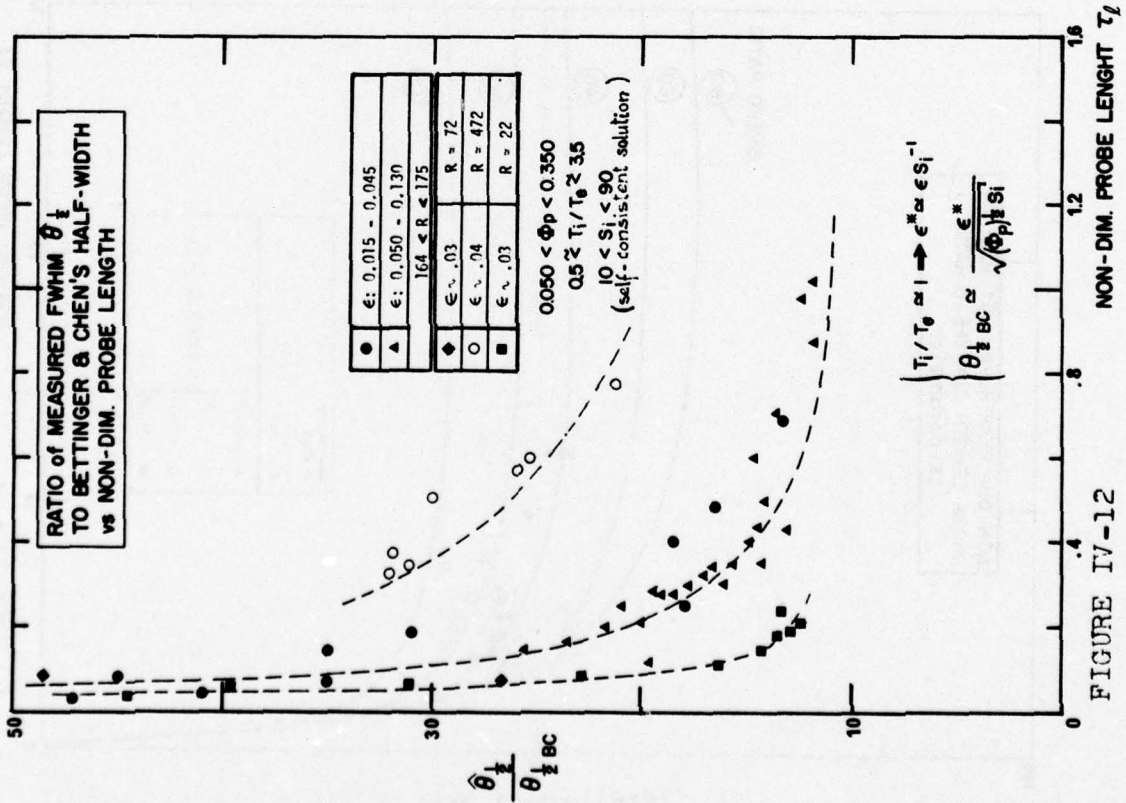


FIGURE IV-12

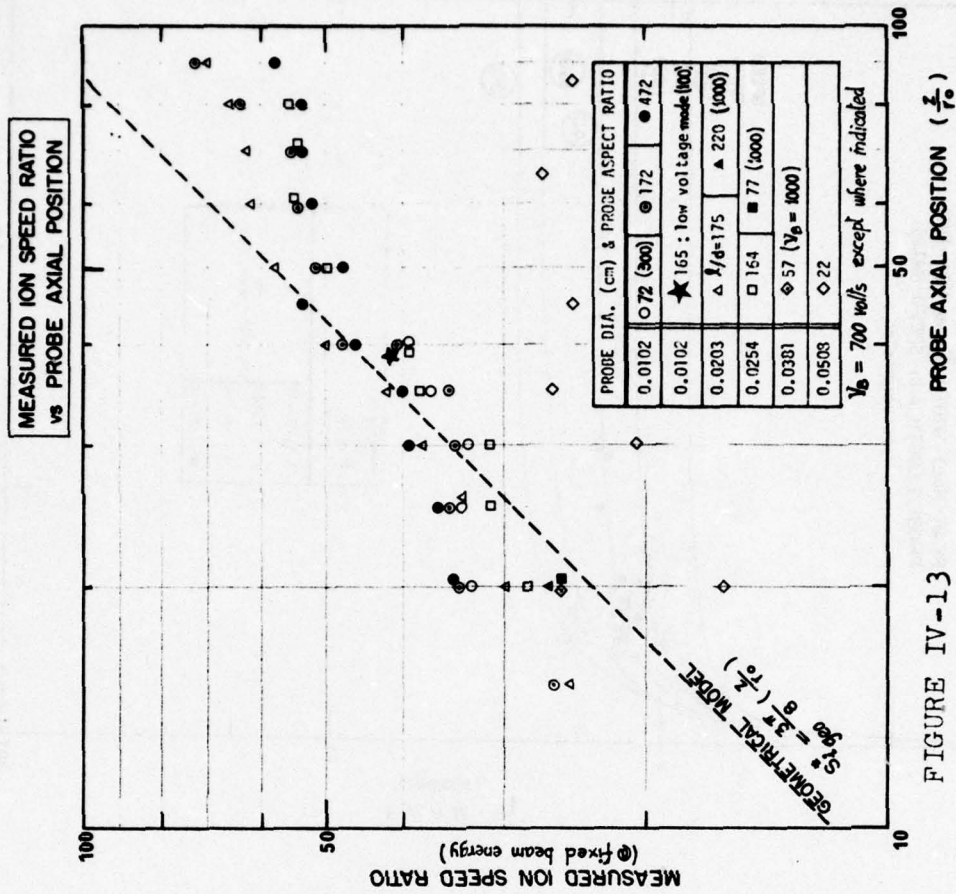


FIGURE IV-13

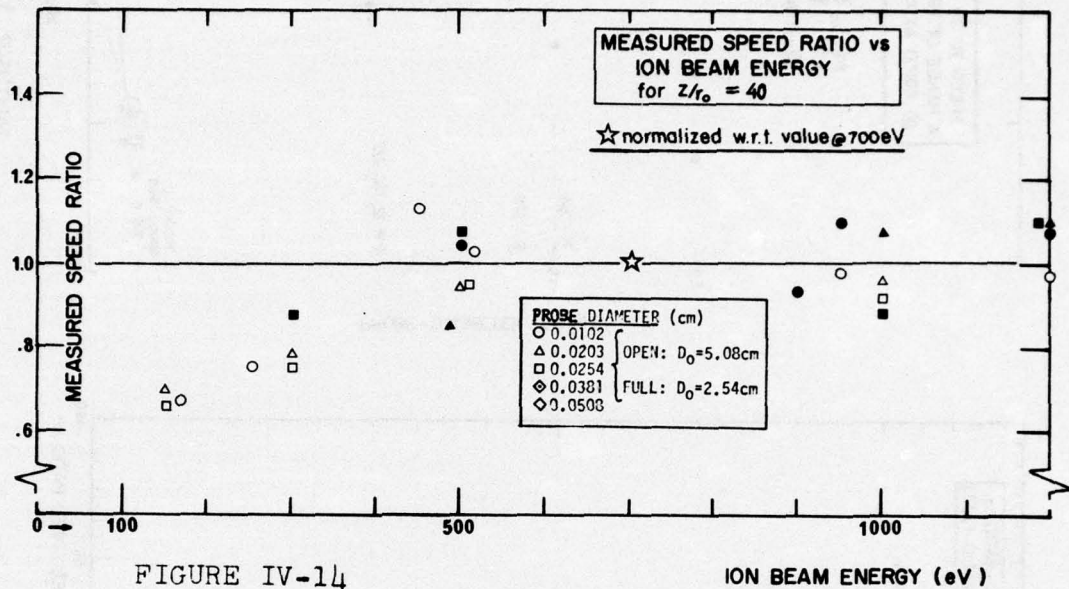


FIGURE IV-14

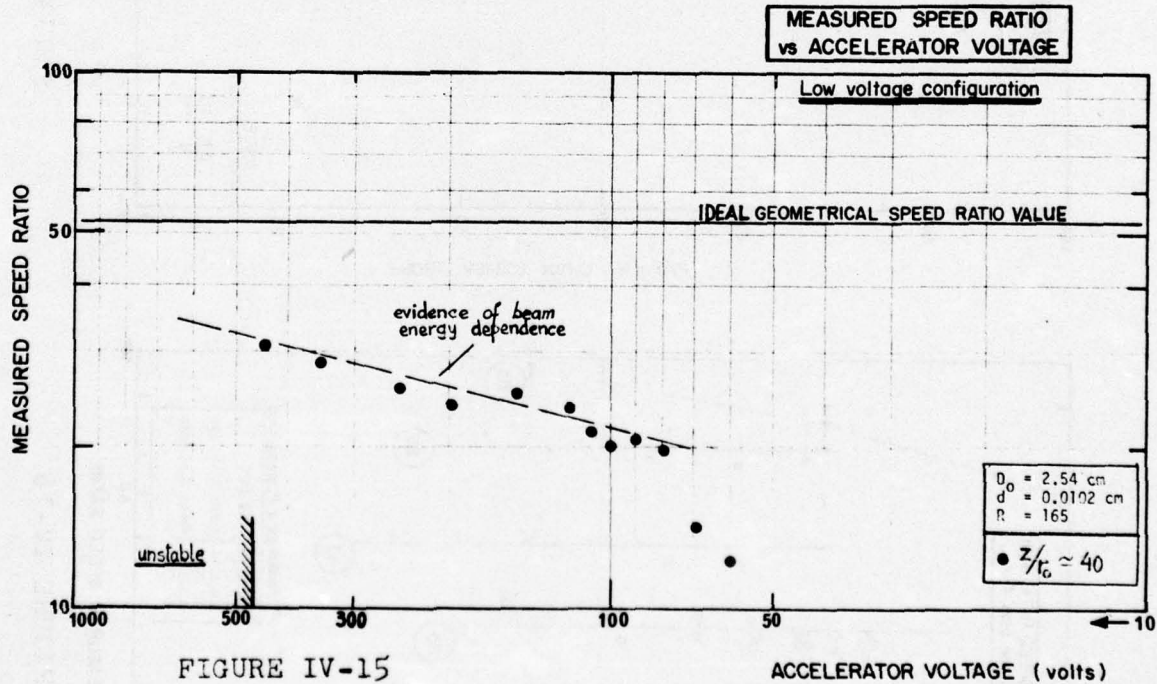


FIGURE IV-15

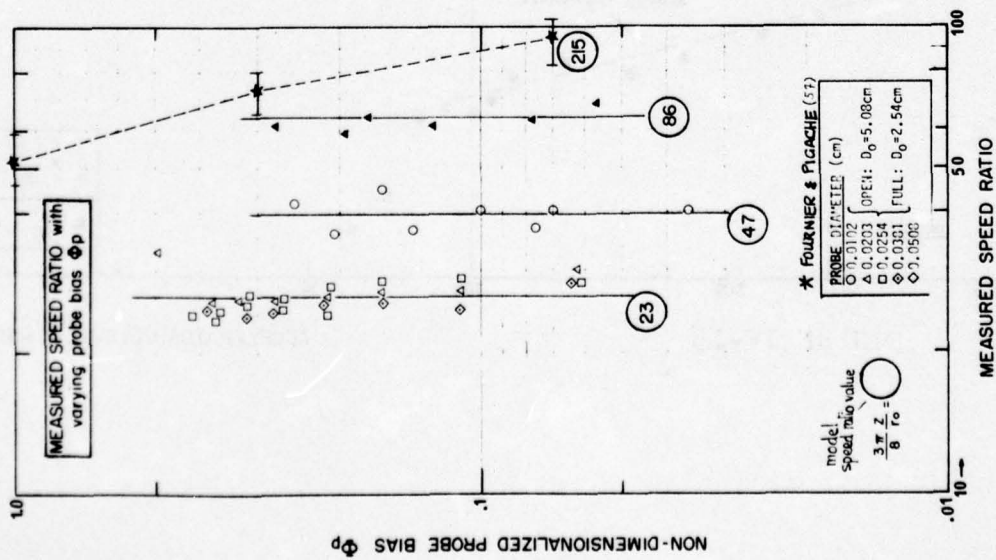


FIGURE IV-16

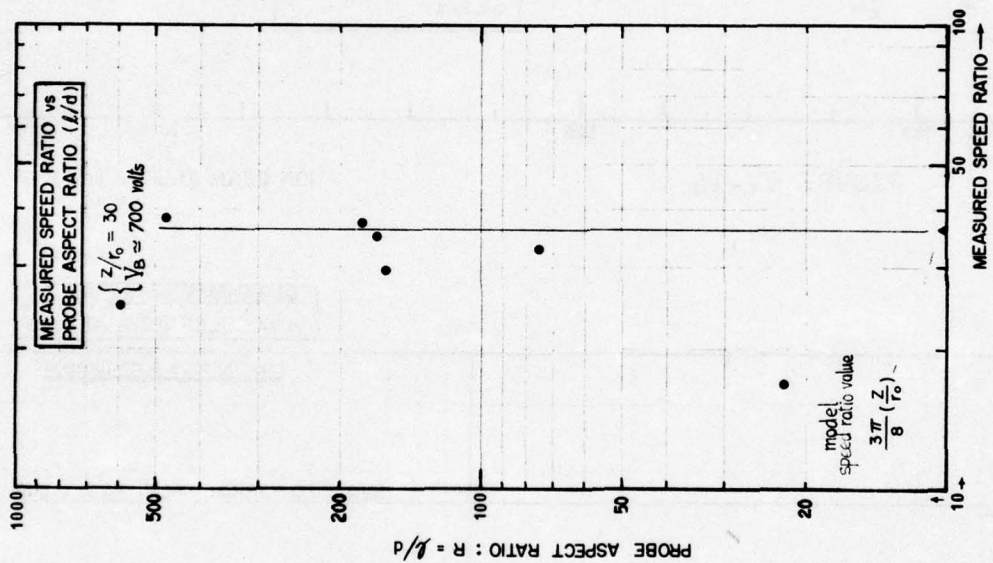


FIGURE IV-17

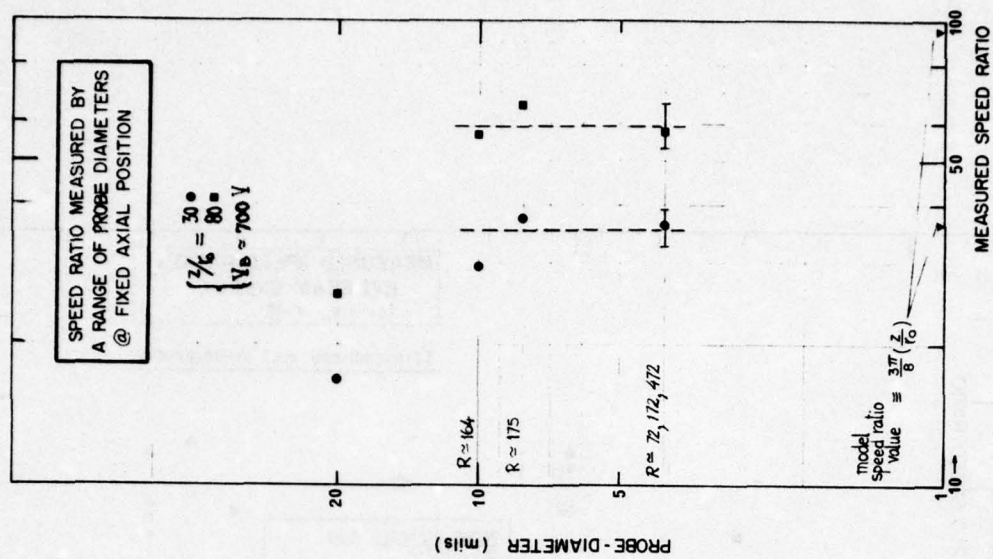


FIGURE IV-18

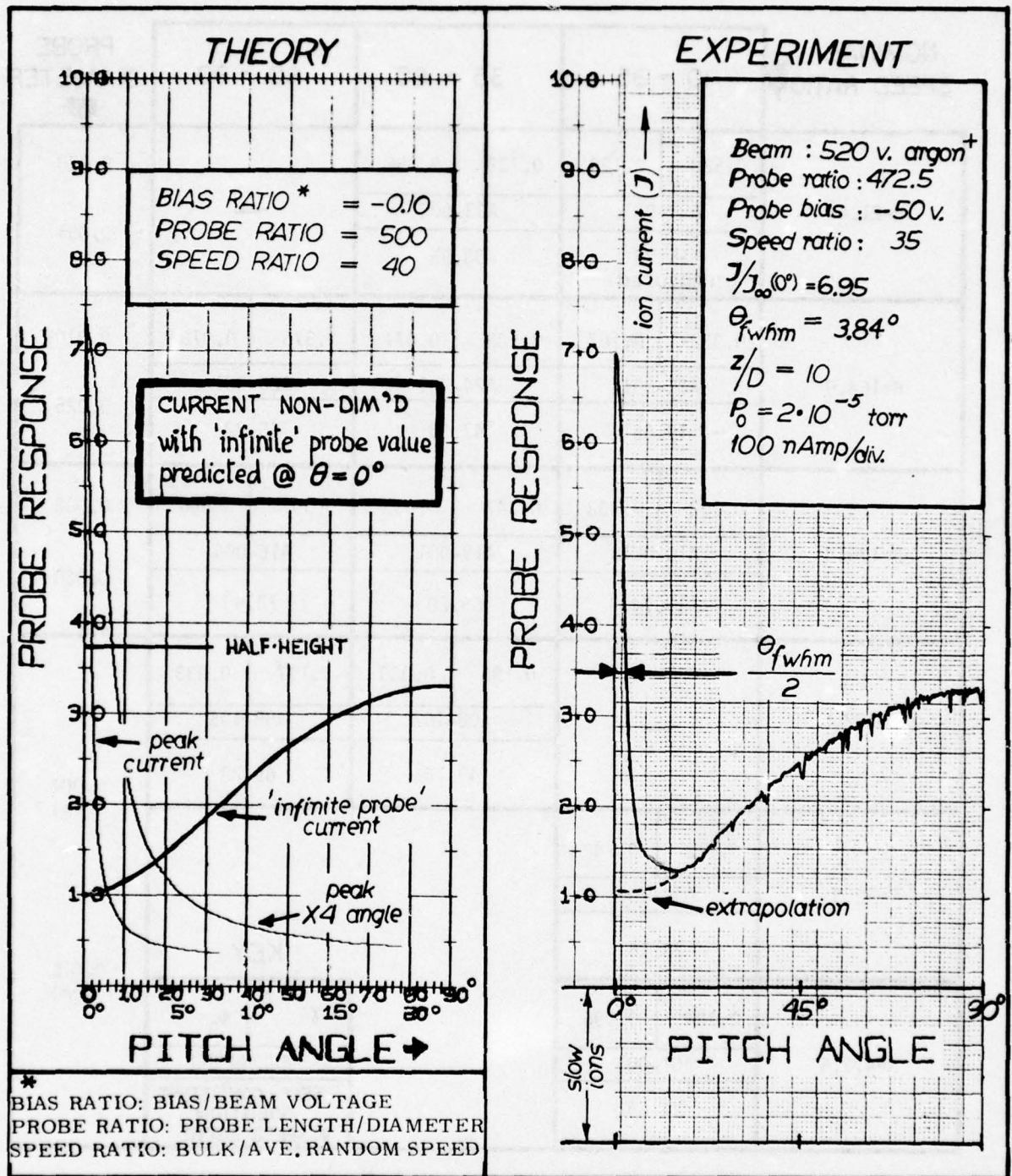


FIGURE IV-19

PROBE RESPONSE SELECTION TABLE[#]

NOMINAL SPEED RATIO	10 - 35		35 - 60		60 - 90		PROBE DIAMETER
§ R=21.6	0.528	0.129	0.732	0.056	—		0.020
	A30-001		A33-002				0.051
	15.73 (measured)		38.95				
R=164.0	0.330	0.167	0.589	0.071	0.375	0.078	0.010
	A26-001		A24-001		A20-001		0.025
	19.55		47.33		65.22		
R=175.0	0.202	0.333	0.347	0.033	0.307	0.056	0.008
	A10-001		A19-001		A16-004		0.020
	19.74		55.20		72.40		
R=172.5	—		0.196	0.033	0.197	0.033	0.004 (in)
			A08-102		A08-105		
			49.16		69.28		
R=72.0	0.412	0.143					0.010 (cm)
	A36-101						
	23.16						
R=472.5	0.134	0.096					
	A01-001						
	34.64						
<div>KEY</div> <div><div>$\bar{\sigma} =$</div><div>$\Phi_p =$</div></div> <div>RUN NUMBER</div> <div>SELF - CONSISTENT SOLUTION ➔ SPEED RATIO</div>							

KEY

$\bar{\delta}$ = +

$\bar{\delta}_p$ = ++

RUN NUMBER

SELF-CONSISTENT
SOLUTION
→ SPEED RATIO

+ $\bar{\delta}$ = CHARACTERISTIC FIELD LENGTH (self-consistent value)

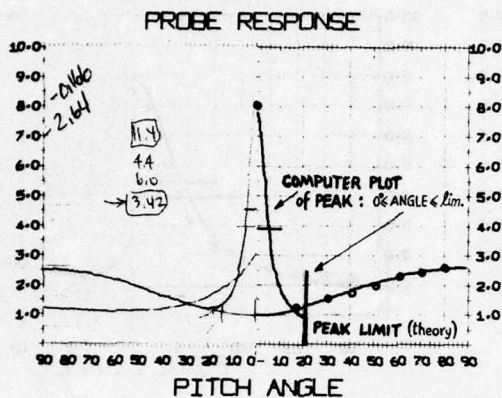
++ $\bar{\delta}_p$ = NON-DIM. PROBE BIAS : $e\phi_p / (\frac{1}{2} M \bar{u}^2)$

§ R = PROBE ASPECT RATIO (l/d)

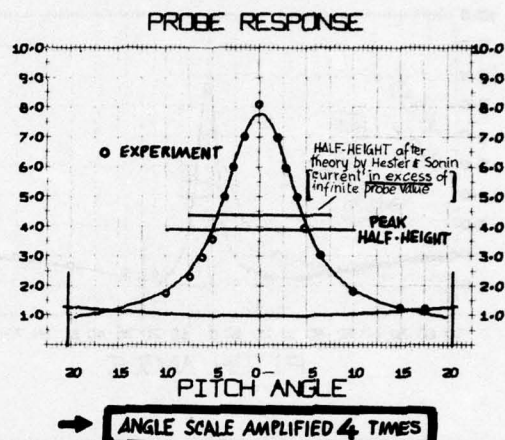
SELECTION REPRESENTATIVE OF RANGE OF PARAMETERS STUDIED

FIGURE IV-20

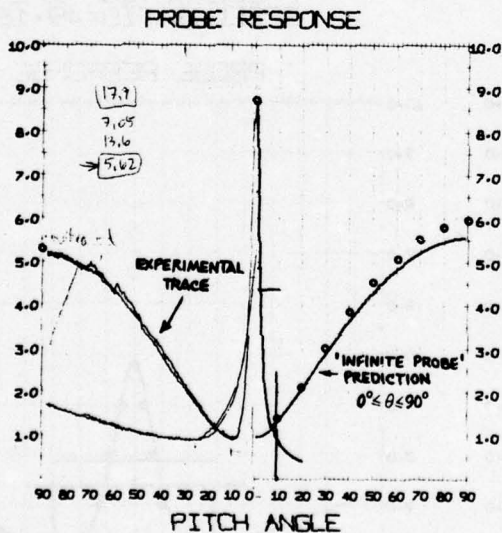
*RUN=A26*001
 PROBE BIAS = 0.167
 PROBE RATIO= 164.0
 SPEED RATIO=19.55 (SELF-CONSISTENT SOLUTION)



*RUN=A26*001
 PROBE BIAS = 0.167
 PROBE RATIO= 164.0
 SPEED RATIO=19.55



*RUN=A19*001
 PROBE BIAS = 0.033
 PROBE RATIO= 175.0
 SPEED RATIO=55.20



*RUN=A19*001
 PROBE BIAS = 0.033
 PROBE RATIO= 175.0
 SPEED RATIO=55.20

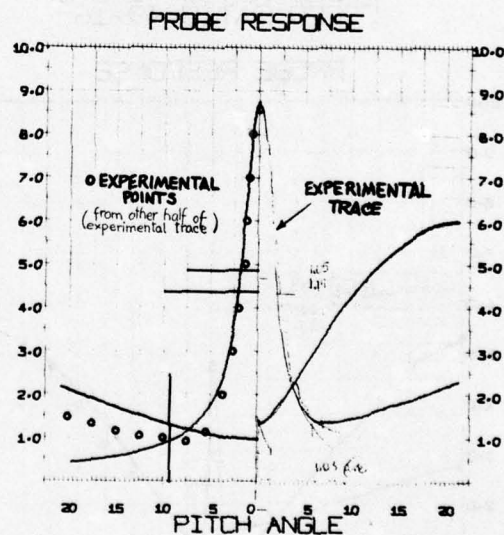
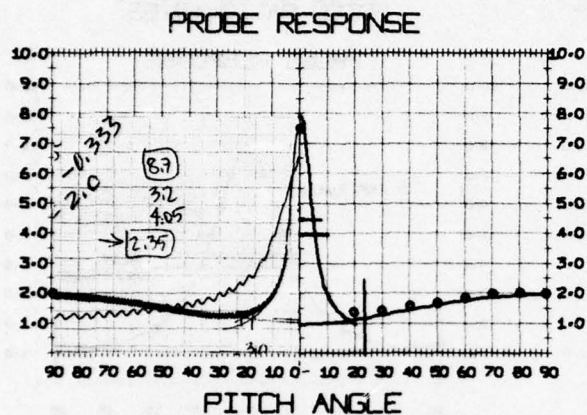
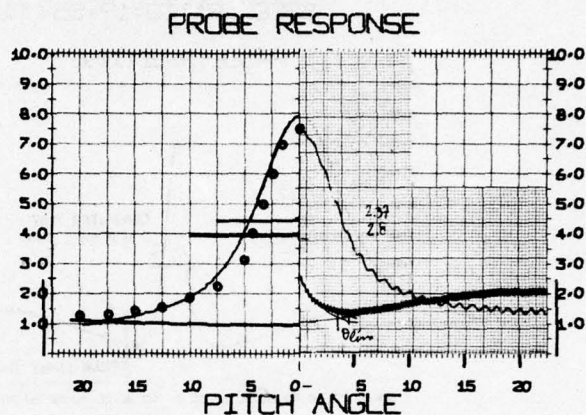


FIGURE IV-21a)

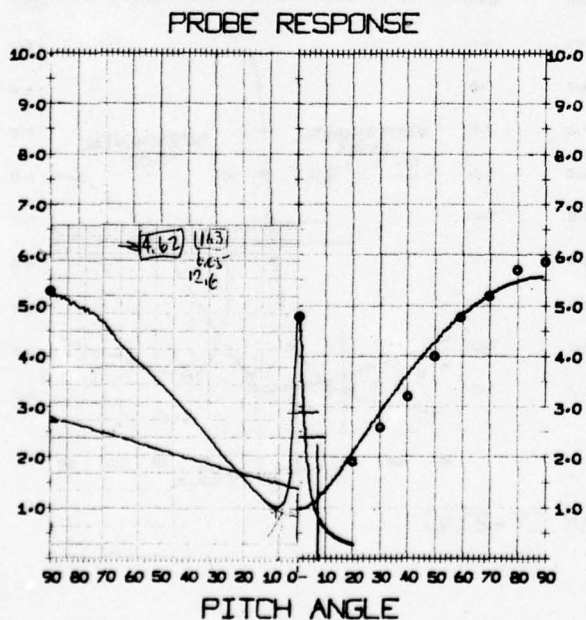
*RUN*A10*001
 PROBE BIAS = 0.333
 PROBE RATIO= 175.0
 SPEED RATIO=19.74



*RUN*A10*001
 PROBE BIAS = 0.333
 PROBE RATIO= 175.0
 SPEED RATIO=19.74



*RUN*A08*102
 PROBE BIAS = 0.033
 PROBE RATIO= 172.5
 SPEED RATIO=49.16



*RUN*A08*102
 PROBE BIAS = 0.033
 PROBE RATIO= 172.5
 SPEED RATIO=49.16

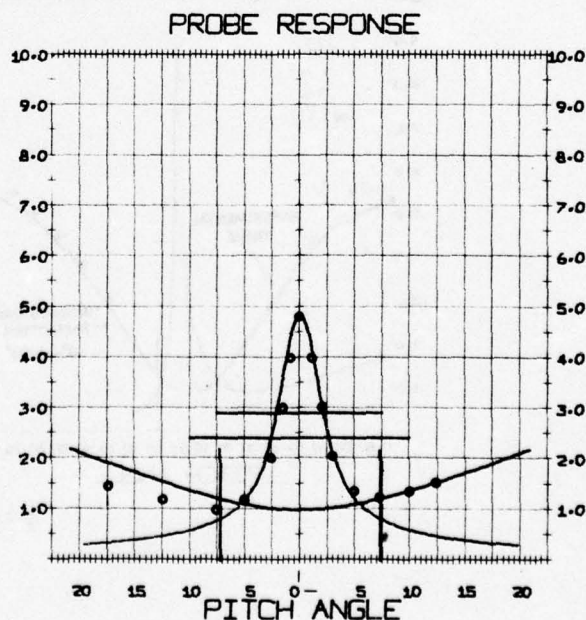
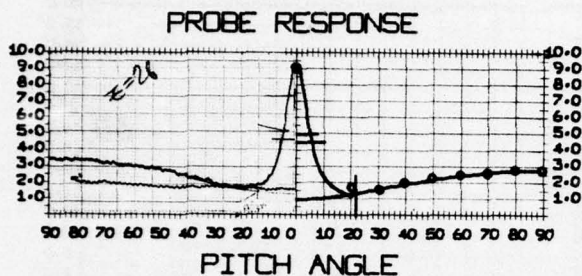
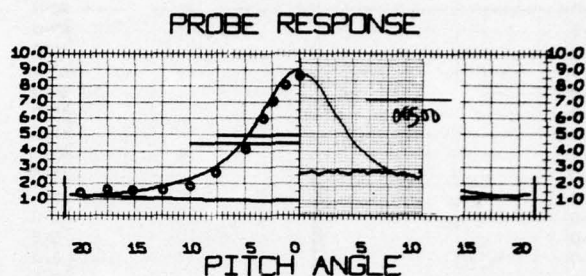


FIGURE IV-21b

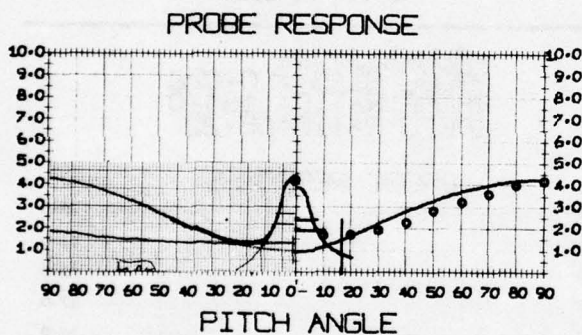
*RUN*A36*101
 PROBE BIAS = 0.143
 PROBE RATIO= 72.0
 SPEED RATIO=23.16



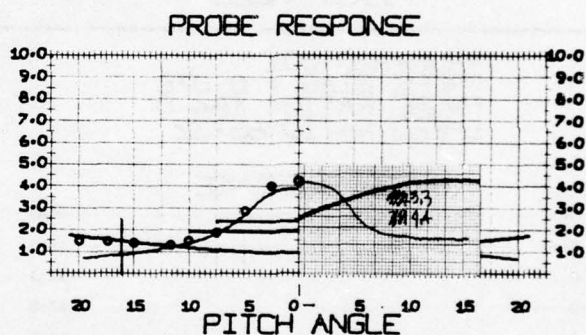
*RUN*A36*101
 PROBE BIAS = 0.143
 PROBE RATIO= 72.0
 SPEED RATIO=23.16



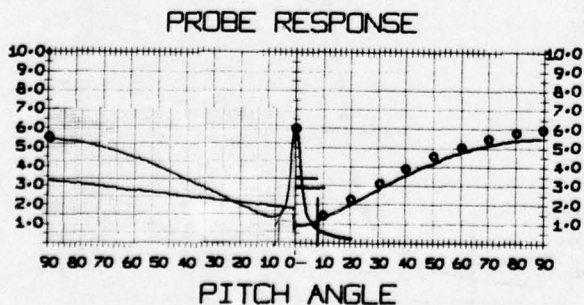
*RUN*A33*002
 PROBE BIAS = 0.056
 PROBE RATIO= 21.6
 SPEED RATIO=38.95



*RUN*A33*002
 PROBE BIAS = 0.056
 PROBE RATIO= 21.6
 SPEED RATIO=38.95



*RUN*A08*105
 PROBE BIAS = 0.033
 PROBE RATIO= 172.5
 SPEED RATIO=69.28



*RUN*A08*105
 PROBE BIAS = 0.033
 PROBE RATIO= 172.5
 SPEED RATIO=69.28

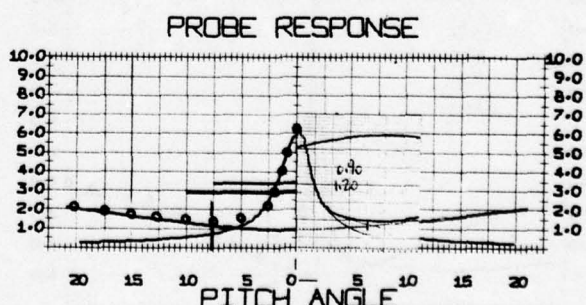
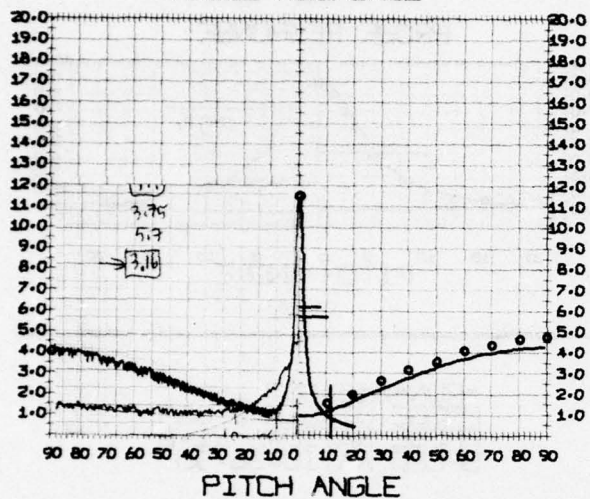


FIGURE IV-21c

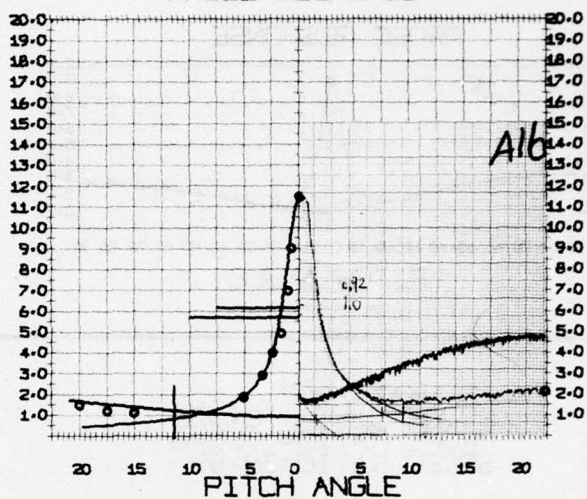
*RUN*A16*004
 PROBE BIAS = 0.056
 PROBE RATIO= 175.0
 SPEED RATIO=72.40

PROBE RESPONSE



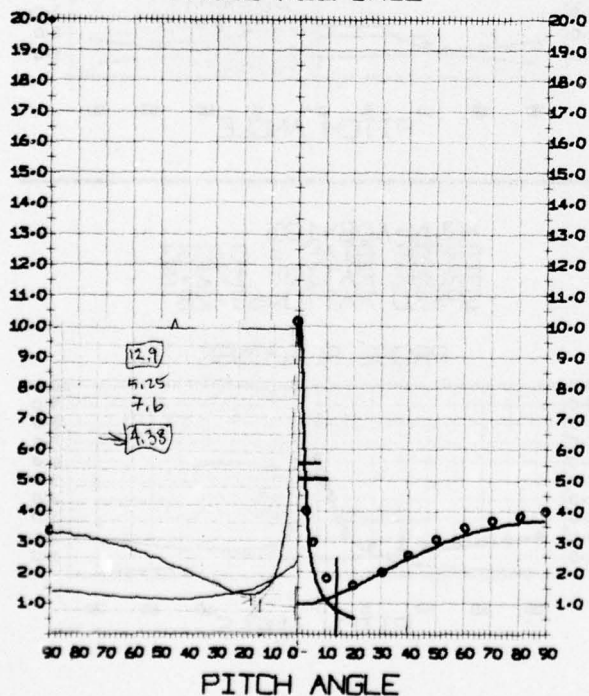
*RUN*A16*004
 PROBE BIAS = 0.056
 PROBE RATIO= 175.0
 SPEED RATIO=72.40

PROBE RESPONSE



*RUN*A20*001
 PROBE BIAS = 0.078
 PROBE RATIO= 164.0
 SPEED RATIO=65.22

PROBE RESPONSE



*RUN*A20*001
 PROBE BIAS = 0.078
 PROBE RATIO= 164.0
 SPEED RATIO=65.22

PROBE RESPONSE

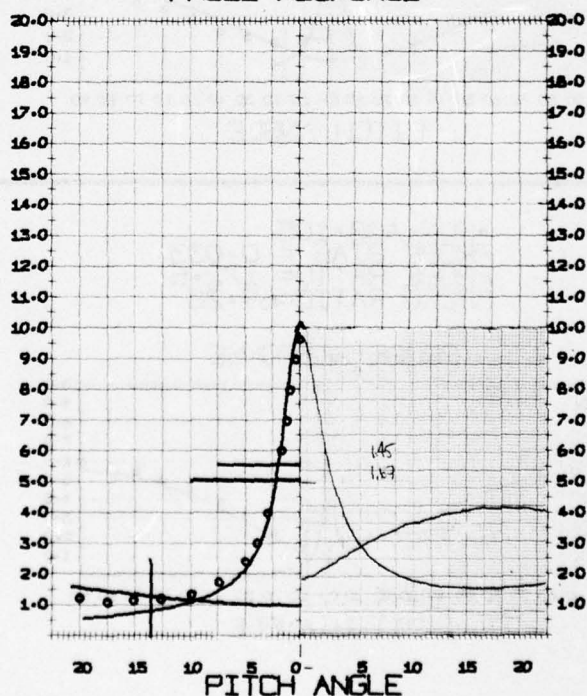
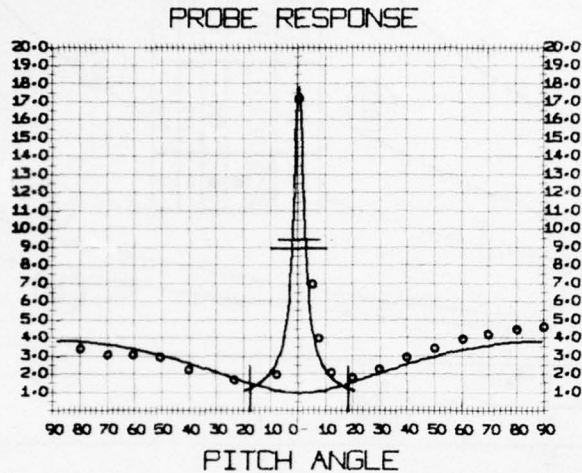
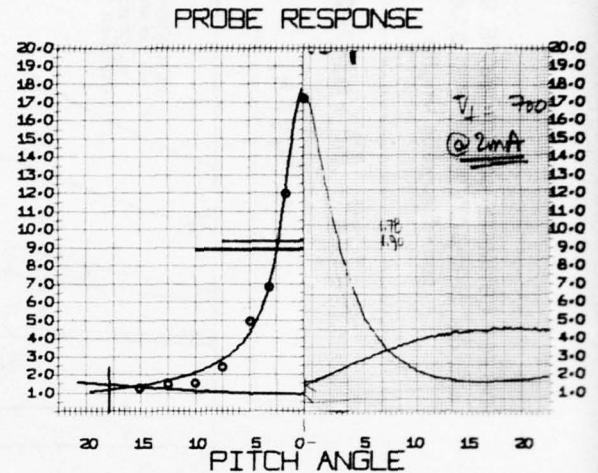


FIGURE IV-21d

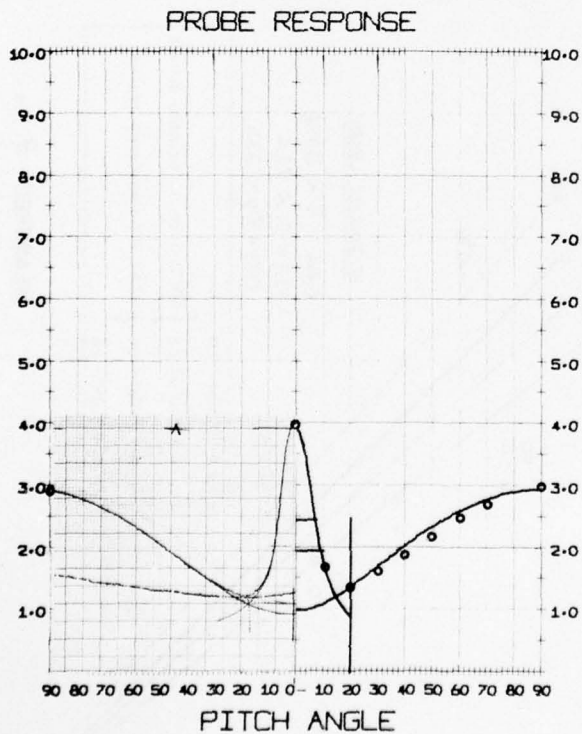
*RUN*A24*001
 PROBE BIAS = 0.071
 PROBE RATIO= 164.0
 SPEED RATIO=47.33



*RUN*A24*001
 PROBE BIAS = 0.071
 PROBE RATIO= 164.0
 SPEED RATIO=47.33



*RUN*A30*001
 PROBE BIAS = 0.129
 PROBE RATIO= 21.6
 SPEED RATIO=15.73



*RUN*A30*001
 PROBE BIAS = 0.129
 PROBE RATIO= 21.6
 SPEED RATIO=15.73

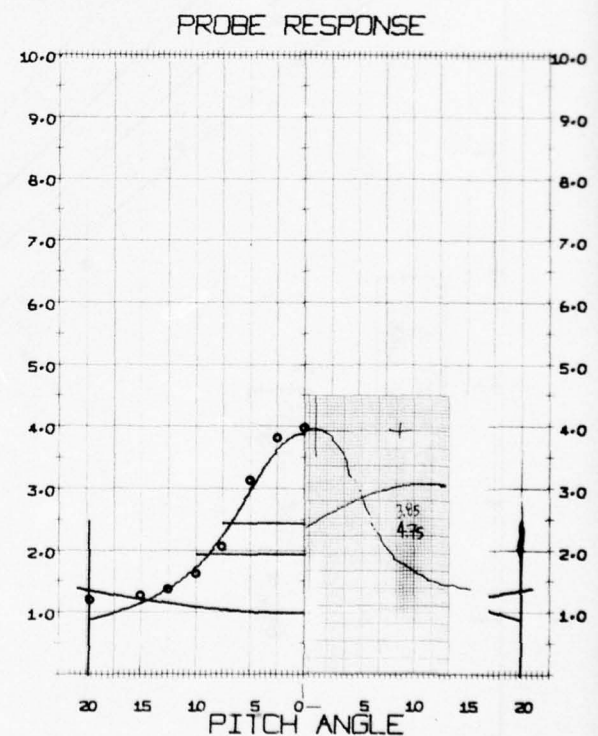


FIGURE IV-21e

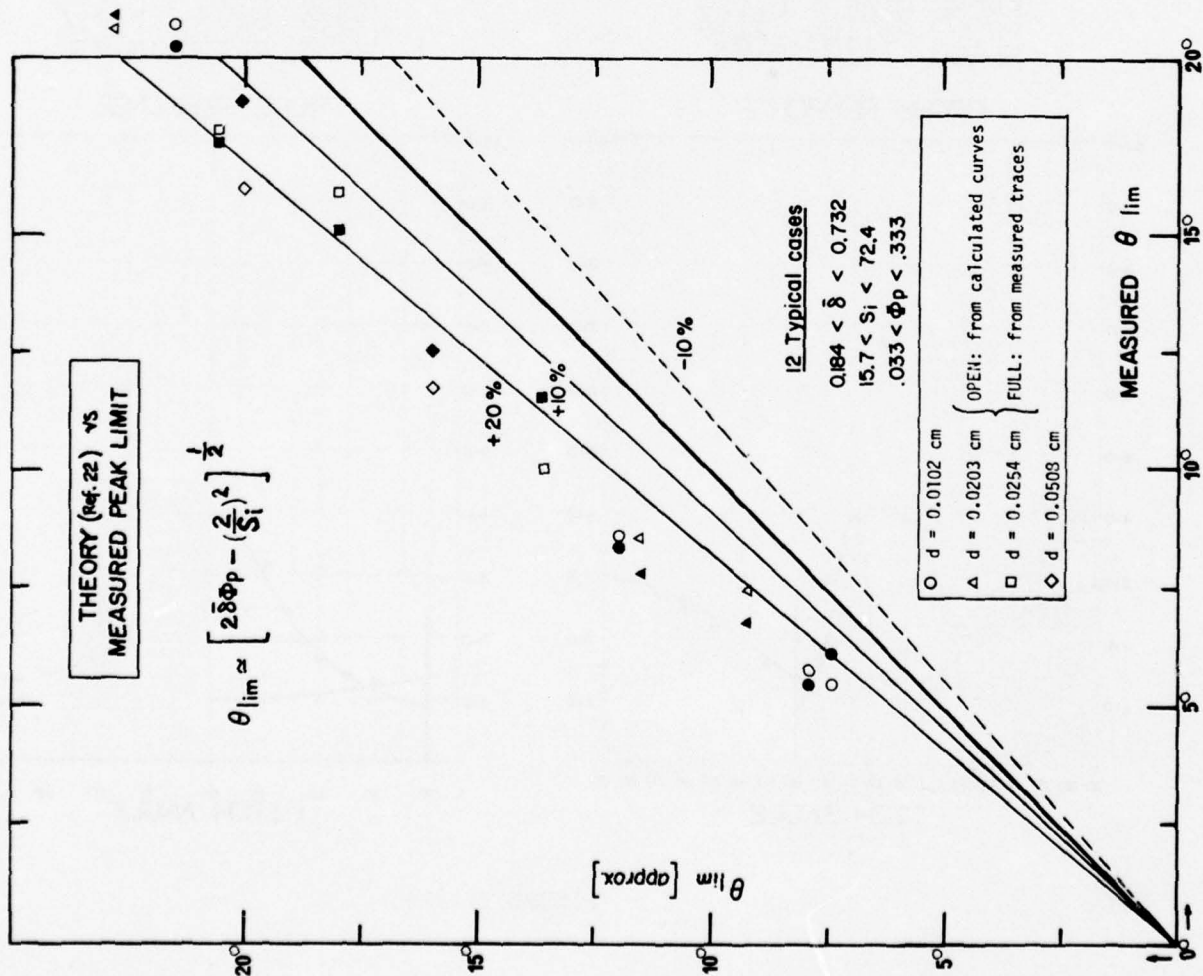


FIGURE IV-22

DIRECT ESTIMATE OF THE PROBE BIAS RATIO
with the CHARACTERISTIC FIELD LENGTH and
non-dim. probe lengths

$$\Phi_p \approx \text{EXP} \left[2\delta^{-1} - \ln \delta + 0.307 - 2 \ln \left(\frac{1}{\epsilon^*} \right) \right]$$

$$\epsilon^* \equiv (\tau_0 / \sqrt{2} R)$$

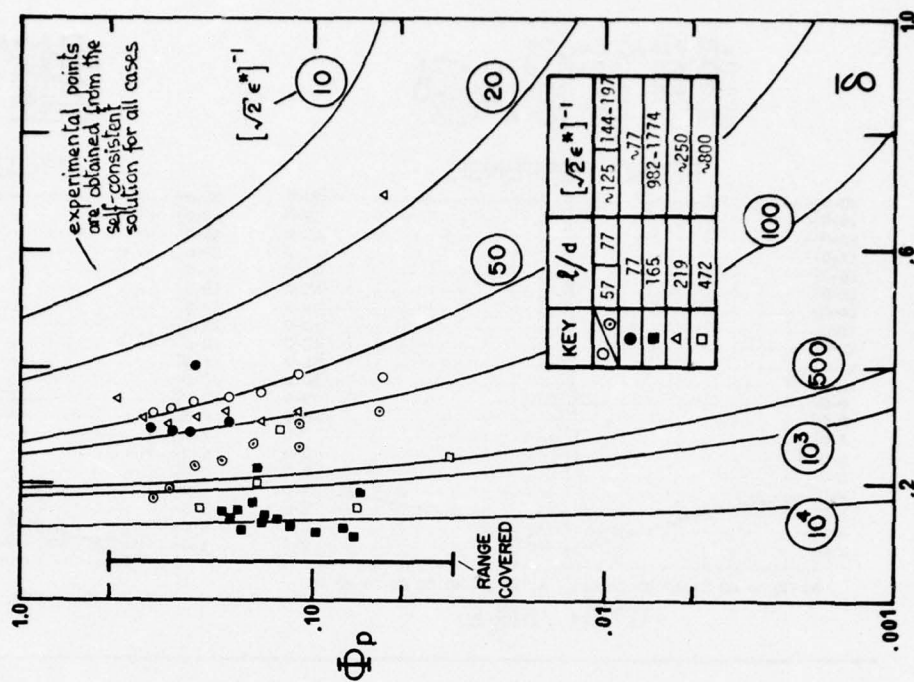


FIGURE IV-23

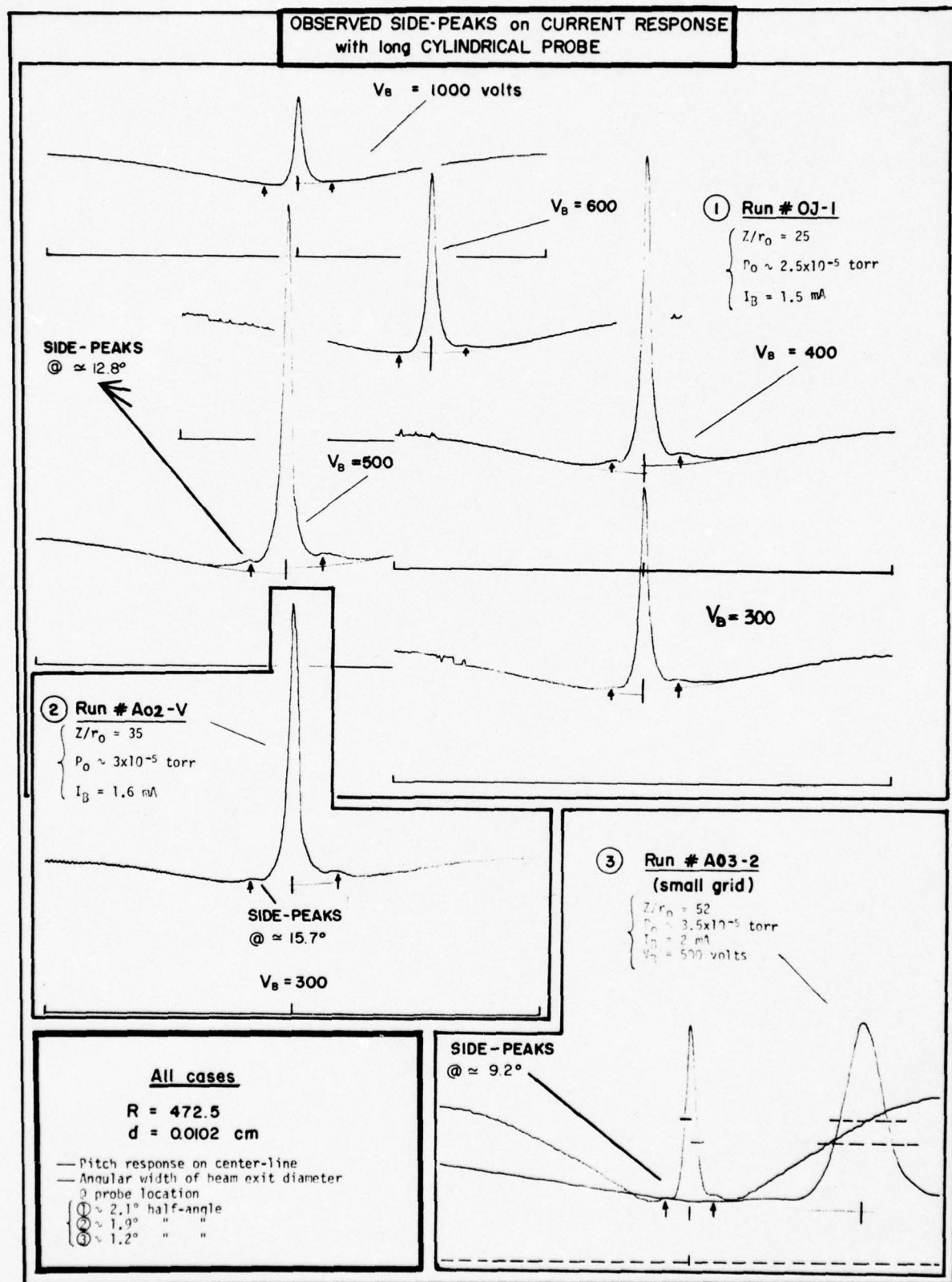


FIGURE IV-24

APPENDIX A - MASS-FLOW MONITORING

A simple and reliable system was constructed to control and monitor the very small argon mass-flows required for this experiment ($\approx 0.1 \mu\text{l/sec}$). The system is composed of a known volume V with a source exit pressure

$$P_e \ll P_v \text{ (ideal pump)}$$

and the feed-line volume is negligible. The system temperature is maintained constant at T_o , thus

$$\begin{aligned} P &= P_o \quad (\text{at } t = 0) \\ T &= T_o \end{aligned}$$

(1) The mass flow at steady-state is given by the gas-law relationship

$$\dot{W} = \frac{MV}{RT} \dot{P} = \frac{MV}{RT} \left(\frac{P - P_o}{\Delta t} \right)$$

(2) With $T = 300^\circ\text{K}$ and argon gas from a volume $V = 5.175\text{l}$, we have

$$\dot{W} \approx 8.5 \times 10^{-2} \dot{P} \text{ (mg/sec)}$$

for \dot{P} ($\text{Nt/m}^2/\text{sec}$) or

$$\dot{W} \approx 0.45 \dot{P} \text{ (equiv. ampere)*}$$

with \dot{P} (torr/min)

(3) Therefore, the mass-flow is known by monitoring the pressure drop of the reference volume with time, provided the total drop is small with respect to the initial pressure (see Fig. A-1)

$$\Delta P \ll P_o$$

Typically, with

$$P_o \approx 750 \text{ torr}$$

$$\Delta t \approx 5 \text{ hours}$$

$$\frac{\Delta P}{\Delta t} \approx (1 \text{ torr}/20 \text{ min})$$

then, we verify (3) since

$$\frac{\Delta P}{P_o} \sim 2\%$$

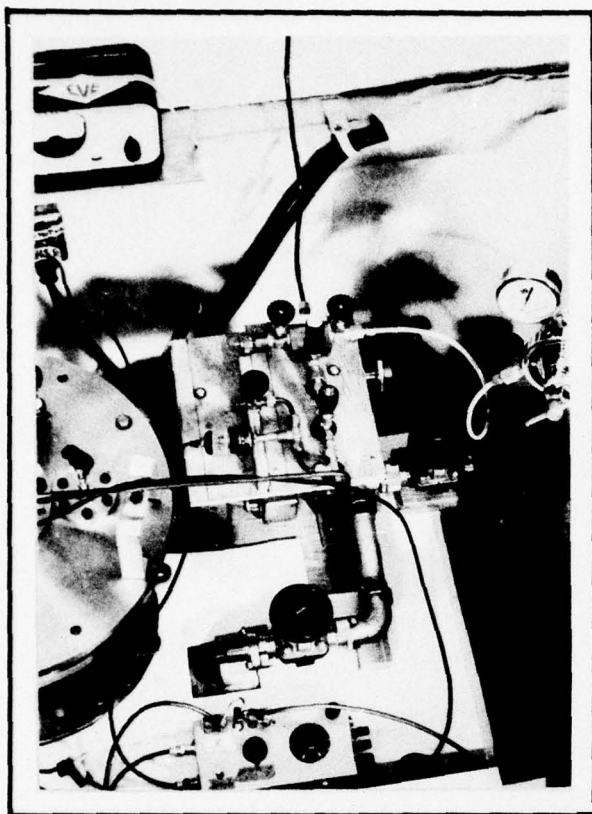
* The equivalent ampere is a quantity which assumes that 6.25×10^{18} neutral atoms represent as many single-charge units.

(4) For argon we have the relations

$$1 \text{ eq. amp} = 0.42 \text{ mg/sec}$$

$$1 \text{ eq. amp} = 0.187 \text{ torr-l/sec @ STP}$$

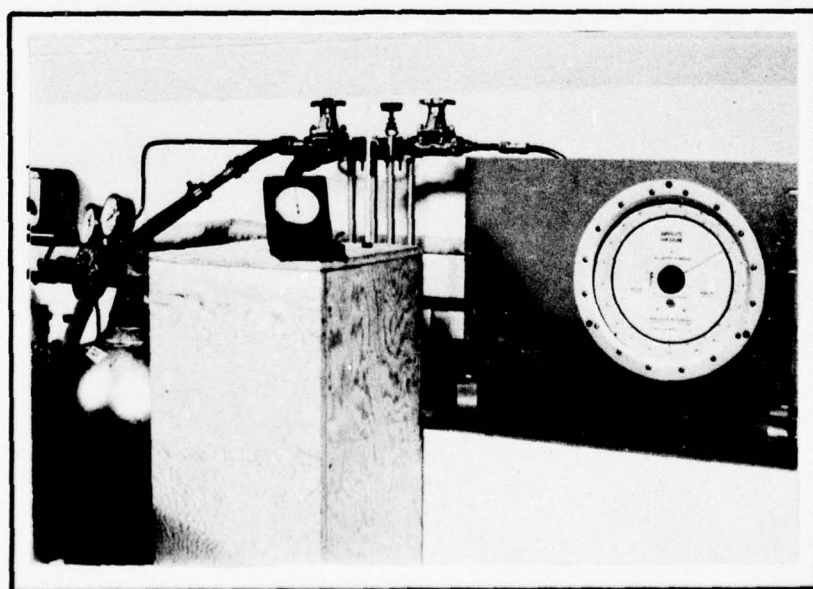
$$1 \text{ eq. amp} = 0.178 \text{ } \mu\text{l/sec @ STP}$$



MASS FLOW CONTROLS



GAS RESERVOIR and
THERMAL INSULATION BOX



MASS FLOW dP/dt MONITORS

FIGURE A-1

FARADAY-CUP PROBE

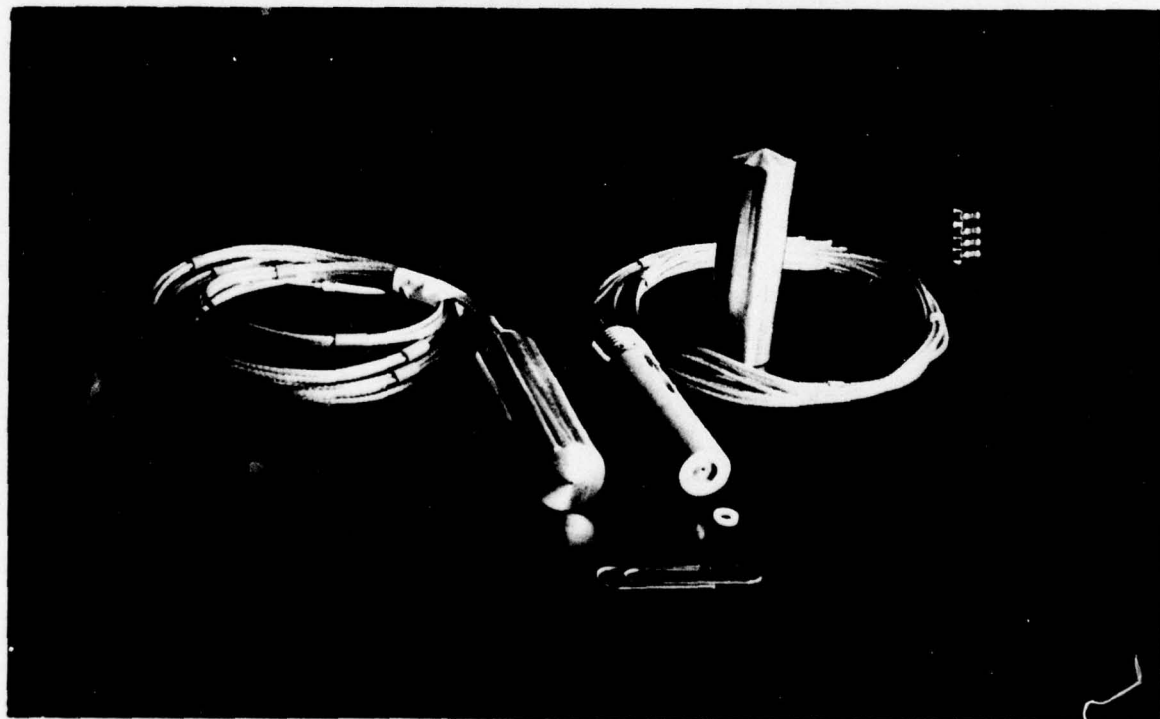
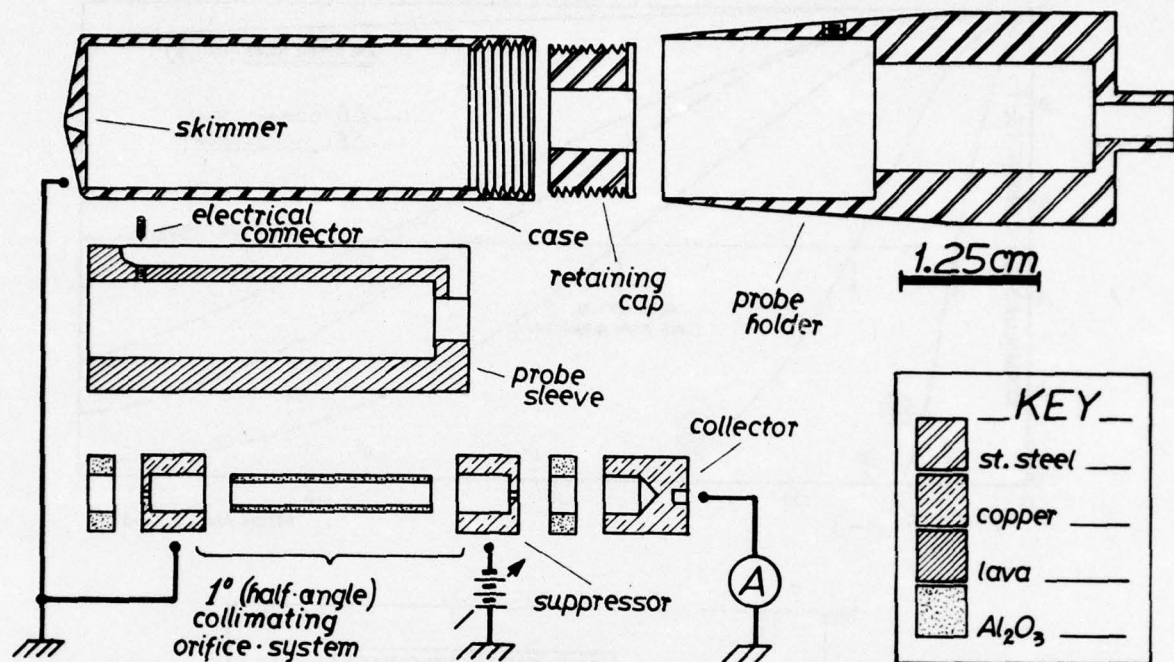
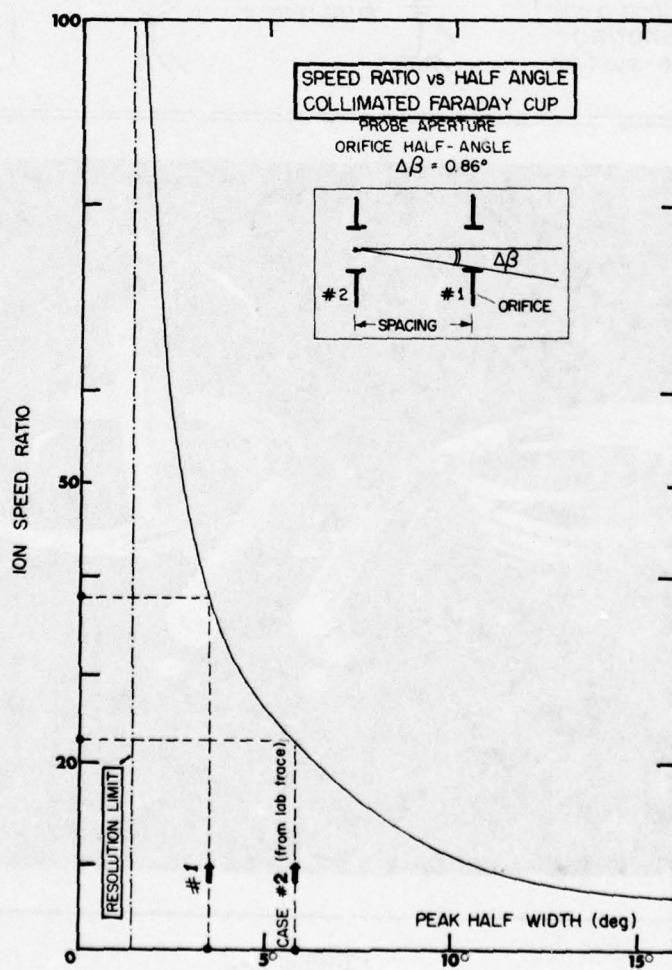
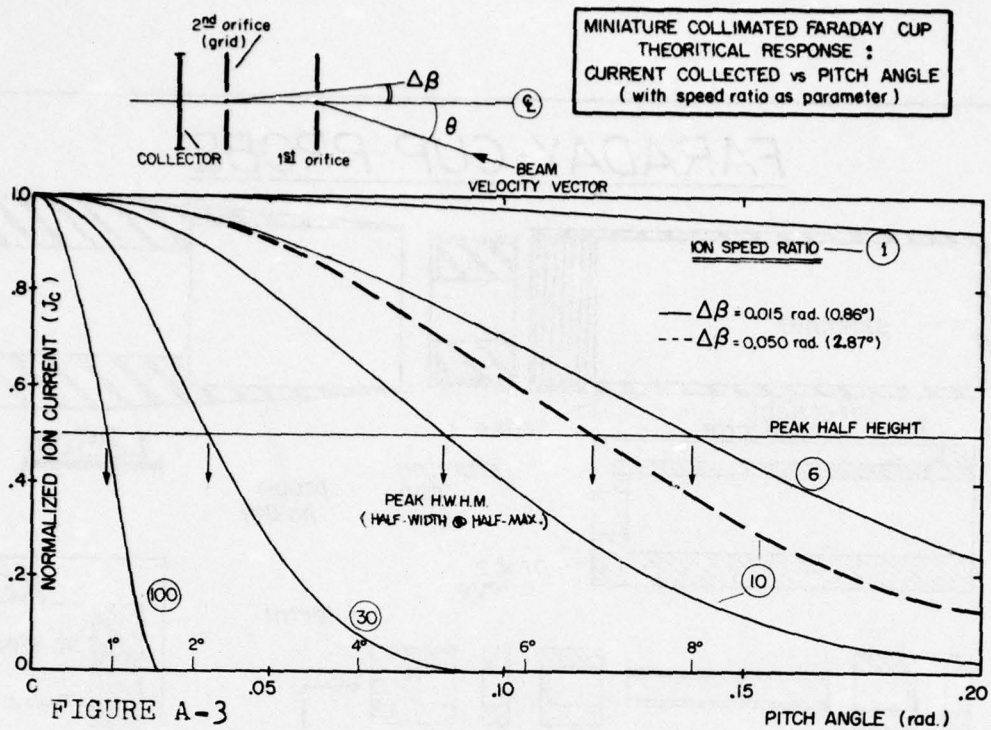


FIGURE A-2



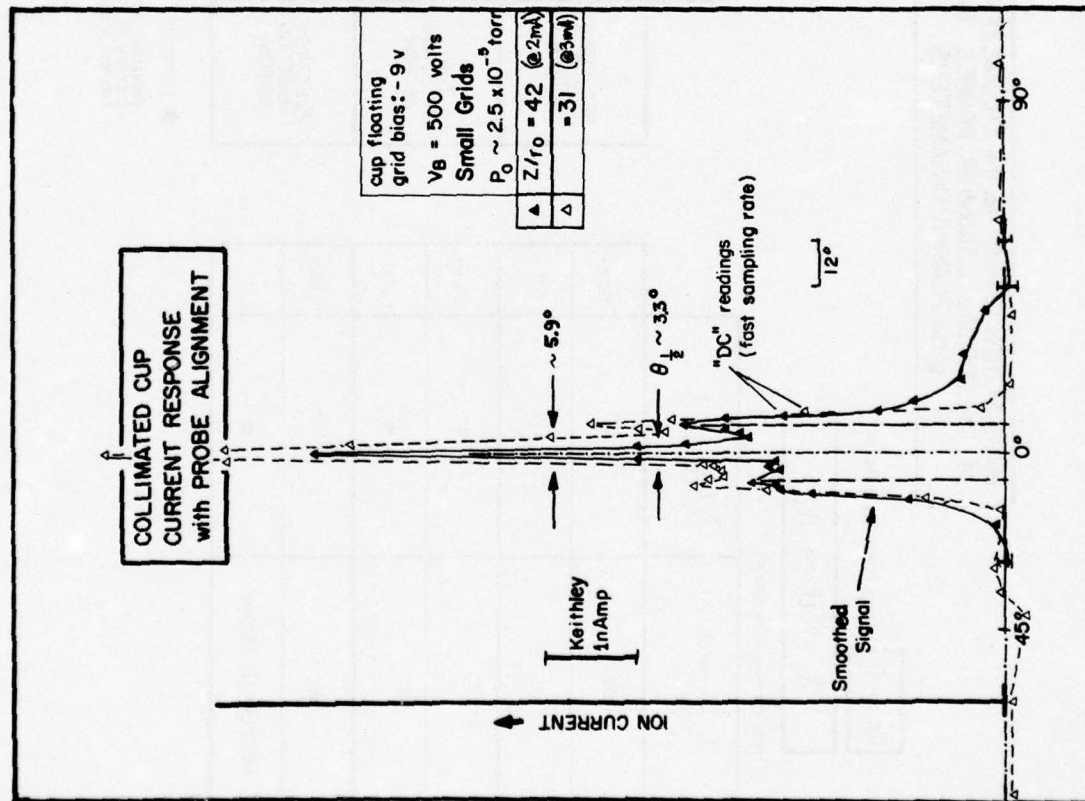


FIGURE A-5

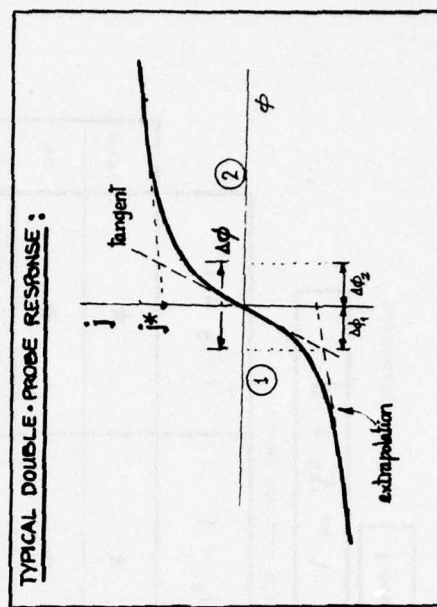
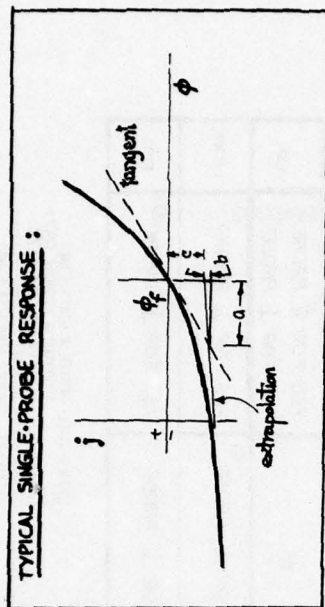


FIGURE A-6

MASS MOTION EFFECT on the CHARACTERISTICS
of CYLINDRICAL LANGMUIR PROBES for the
given PLASMA PARAMETERS

$Kn \gg 1$ (THIN-PROBE-COLLISIONLESS)

$\lambda \gg d \gg \Lambda_D$

(CONVENTIONAL THIN SHEATH)

	$T_i/T_e \gg 1$	$T_i/T_e \ll 1$	
RETARDING FIELD REGION	NO	NO	THEORY
	NO	NO	EXP.
ION COLLECTING REGION	YES	★	THEORY
	YES	★	EXP.
ELECTRON COLLECTING REGION	★	NO	THEORY
	NO FOR \perp PROBE	★	EXP.

$Kn \gg 1$ (THIN-PROBE-COLLISIONLESS)

$\lambda \gg \Lambda_D \geq d$

(OPTICAL LIMIT-THICK SHEATH)

	$T_i/T_e \gg 1$	$T_i/T_e \leq 1$	
RETARDING FIELD REGION	★	★	THEORY
	★	★	EXP.
ION COLLECTING REGION	NO FOR \perp PROBE	NO FOR \perp PROBE YES FOR \parallel PROBE VALUING EFFECT FOR $T_e \rightarrow 1$	THEORY
	★	YES FOR \parallel PROBE NO FOR \perp PROBE	EXP.
ELECTRON COLLECTING REGION	YES FOR \perp PROBE	YES FOR \perp PROBE	THEORY
	YES FOR \perp PROBE	YES FOR \perp PROBE	EXP.

★ INCOMPLETE

(POSITIVE IONS

RESONANT FLOW WITH $\vec{v}_i \cdot \vec{v}_e \cdot N_e \cdot \vec{v}_h$

IN MAGNETIC FIELDS

① COLD-IONS: HESTER & SMITH (18)

② FORTNEY & PROCTOR (57)

③ JARVIS: BETTIGER & CHEN (17)

④ TAILLET, SPITZER, FORTNEY (24)

⑤ COOPMAN & SMALL (32)

FORTNEY (25)

FIGURE A-7

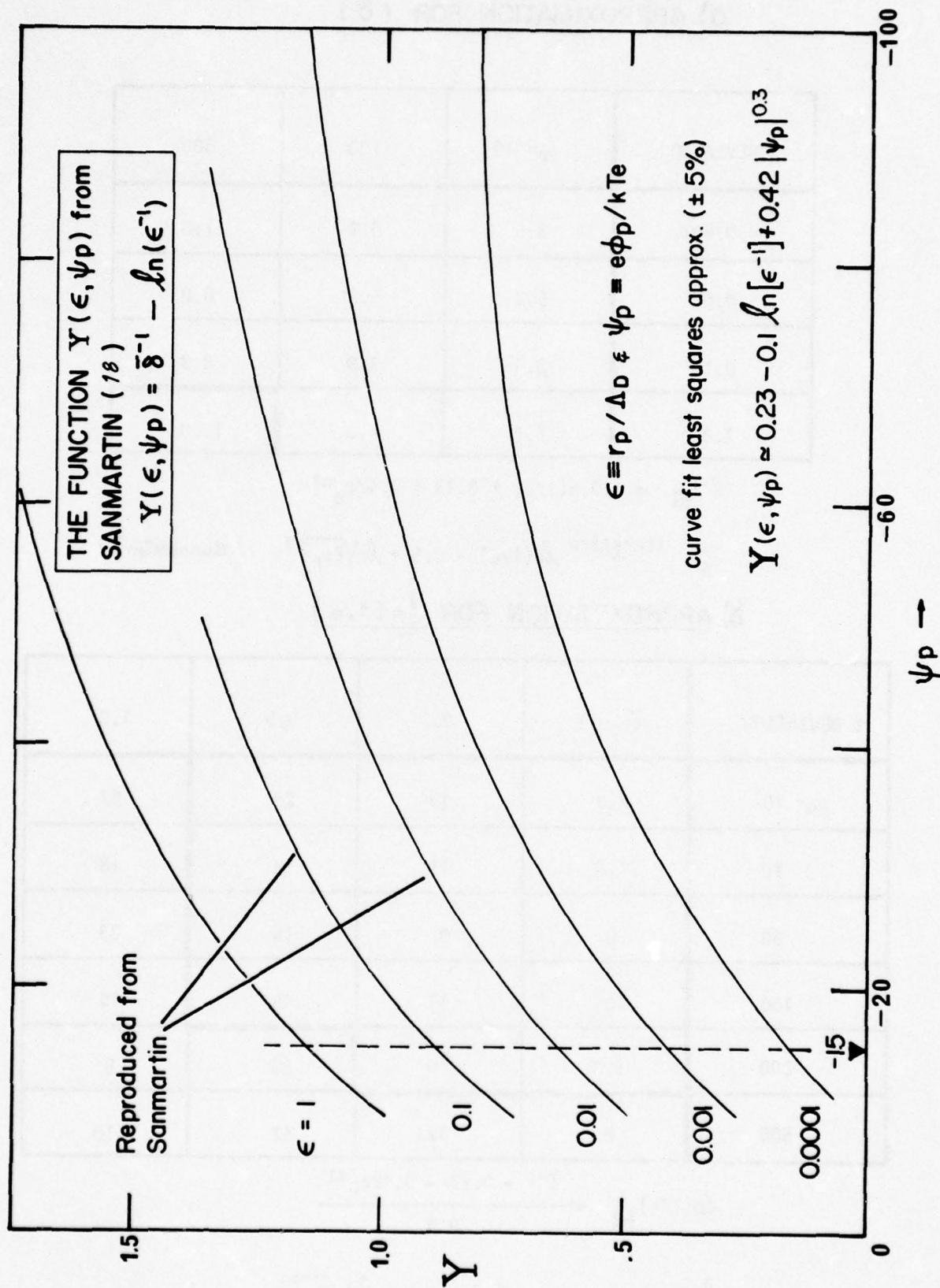


FIGURE A-8

a) APPROXIMATION FOR ($\bar{\delta}$)

% DEVIATION	$\psi_p = 10$	100	500
$\epsilon = 0.001$	3.6	0.9	1.8
0.01	5.3	1.2	6.0
0.10	8.4	3.8	8.3
1.0	6.4	2.8	15.0

$$\bar{\delta}^{-1}_{fit} \approx 0.9 \ln(1/\epsilon) + 0.23 + 0.42\psi_p^{0.3}$$

$$\bar{\delta}^{-1}_{S} \text{ iteration } \ln(1/\epsilon) = 0.5 + \ln\sqrt{2\psi_p\bar{\delta}^{-1}} \quad (\text{Sanmartin})$$

b) APPROXIMATION FOR $\ln(1/\epsilon)$

% DEVIATION	$\bar{\delta} = 0.1$	0.3	0.5	1.0
$\psi_p = 10$	2.3	13	23	97
20	1.0	11	18	18
50	0	9	15	23
100	0	11	45	15
200	1.3	19	53	5
500	6	124	42	10

$$\ln(1/\epsilon)_{fit} \approx \frac{\bar{\delta}^{-1} - 0.23 - 0.42\psi_p^{0.3}}{0.9}$$

$$\ln(1/\epsilon)_{Sanmartin} \approx \bar{\delta}^{-1} + 0.5 - \ln\sqrt{2\psi_p\bar{\delta}^{-1}}$$

FIGURE A-9

OUTLINE OF THE METHOD DEPICTING THE APPROXIMATE SOLUTION OF $(Y_1 - Y_2)$ YIELDING AN ESTIMATE OF $\epsilon(T_e) \equiv \epsilon_M$ AND T_e

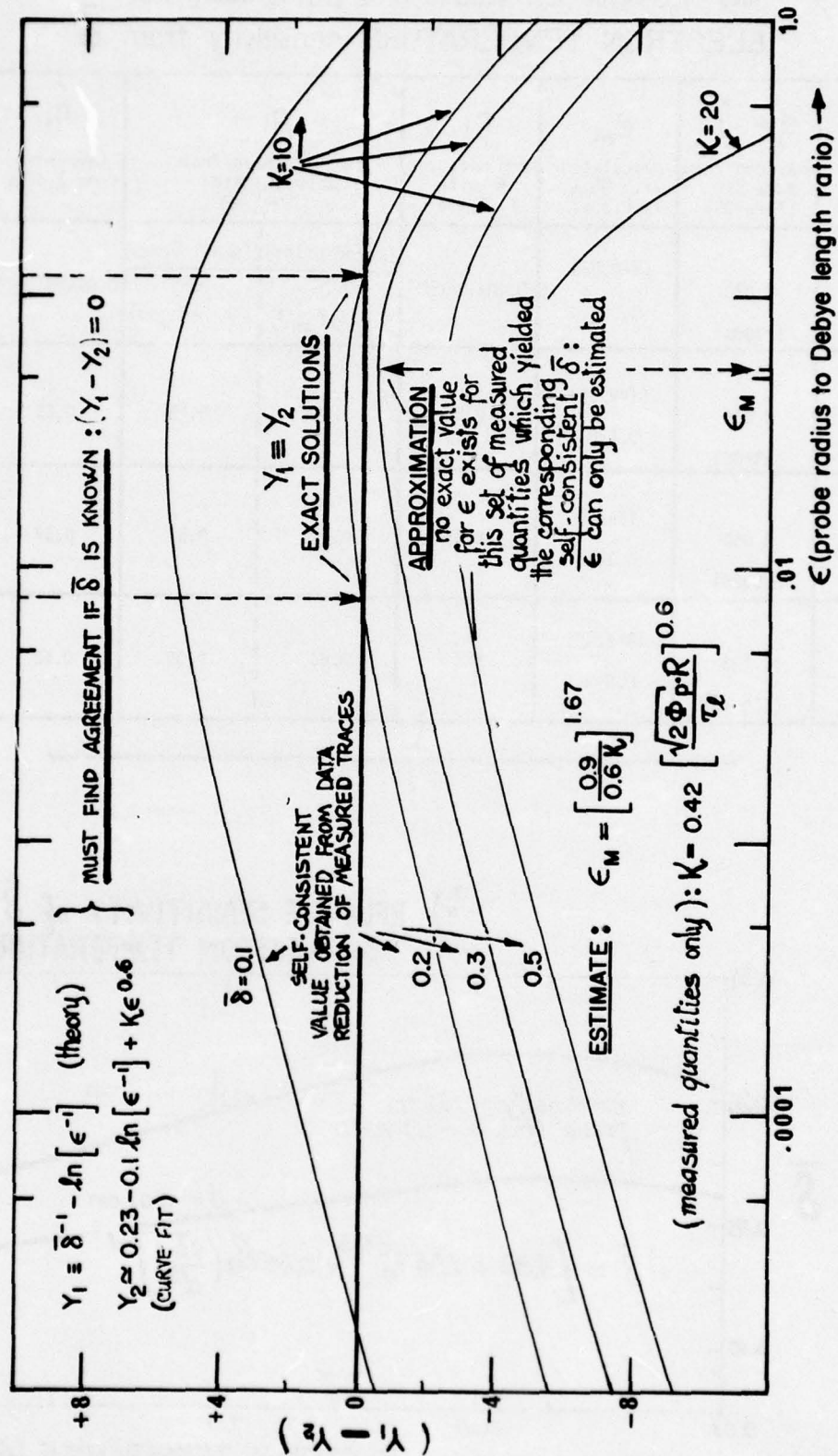
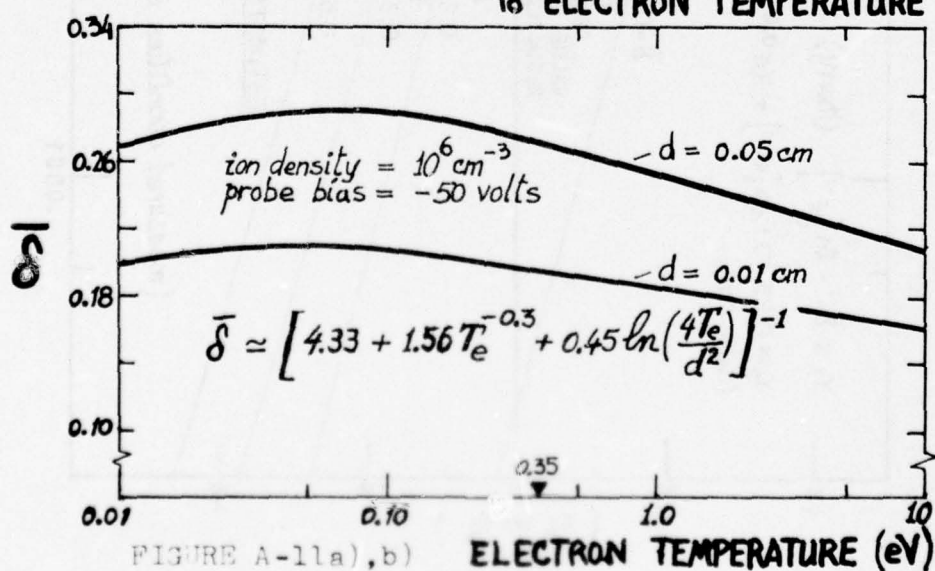


FIGURE A-10

a) ESTIMATED values of ϵ, n_i, T_e using the
ELECTRON TEMPERATURE sensitivity from $\bar{\delta}$

PROBE DIA. (cm)	$\epsilon_M = \frac{r_p}{\lambda_D}$ measured from data fit ($Z/r_0=30$)	ϵ_M calculated with γ_0 & $T_e \sim 0.35\text{eV}$	n_i from measured ϵ with $T_e \sim 0.35\text{eV}$	n_i measured mean from \perp probe data ($Z/r_0=30$)		n_i (average) from \perp data	T_e from measured $n_i(\perp \text{ probe})$ & ϵ measured
				(large grids)	(small grids)		
0.0102	0.020 ($\pm 300\%$)	($\bar{\delta}=0.22$) 0.035	$0.60 \times 10^7 \text{cm}^{-3}$	0.76 ($\times 10^7 \text{cm}^{-3}$)	0.58 ($\times 10^7 \text{cm}^{-3}$)	$0.67 \times 10^7 \text{cm}^{-3}$	0.71eV
0.0203	0.035 ($\pm 340\%$)	($\bar{\delta}=0.30$) 0.128	0.54	0.68	0.55	0.62	0.76eV
0.0254	0.052 ($\pm 590\%$)	($\bar{\delta}=40$) 0.342	0.65	0.63	0.51	0.57	0.57eV
0.0508	0.105 ($\pm 660\%$)	($\bar{\delta}=0.48$) 0.619	0.66	0.65	0.39	0.52	0.60eV

b) RELATIVE SENSITIVITY of $\bar{\delta}$
to ELECTRON TEMPERATURE



APPENDIX B - PROBE SPURIOUS EFFECTS

Both magnetic and R.F. fields can be neglected here; the spurious effects on the collection of positive ions can be described briefly under three headings:

- ion current over-estimation
- ion current under-estimation
- contamination

(i) Ion Current Over-Estimation

Over-estimation may originate from secondary-electron emission from the probe due to thermionic effects, photo-emission, ion and metastable atom collisions or ion and atom bombardment (2nd Townsend yield) at the metallic surface (Ref. 79). The first three sources can be neglected, from rate-process probabilities and surface energy considerations (Ref. 13), though ion and metastable atom bombardment is occurring in this regime. Secondary-electron yield from direct bombardment would constitute the major contribution. Reported figures indicate a maximum yield of about 0.1 electron/ion at incident energies up to 1.5 KeV, for singly ionized argon on atomically clean W. Gas covered ('dirty') conditions, which occur when foreign atoms are adsorbed on the surface, would give a figure generally much lower (Ref. 63) and an estimate of 0.05 is representative of the maximum yield in this regime. Similarly metastable-atom bombardment would not imply any significant contribution. From these conservative estimates therefore, no correction was made to the collected currents. Finally, more insidious effects such as reflections, oscillations and 'trapped' orbits have been neglected.

(ii) Ion Current Under-Estimation

Since the probe is made strongly negative for the present study, this second category is more likely to be less important than the sources indicated under (i). Ion reflections or ejections and sputtering of heavy particles (generally neutrals from the metal) although significant in some instances (see Appendix C), is of little concern to us here. Finally, from conservative estimates, doubly-charged ions would not contribute to more than about 4% of the net currents.

(iii) Contamination

This subject has been treated in Appendix C, yet it is worth noting that contamination of the probe can account for some error since it can imply that the true collecting surface is not known precisely. Conducting or insulating layers on the collector, or on the ceramic stem, could originate from a few sources: backstreaming oil, evaporation of tungsten from the source and the neutralizer filaments, and possibly from backspotted material (copper and aluminum) from within the test section; the knowledge of such possibilities has led us to regular and careful inspection of the probes. A black layer of baked oil was occasionally observed on the insulator parts and found to be slightly conductive. The probe was then flame cleaned and fresh ceramic cement was applied. Both hot tungsten emitters required on the accelerator were screened to prevent direct line-of-sight with the probe. No significant metallic coating was observed for extensive running periods.

APPENDIX C - ION-BOMBARDMENT PROBE CLEANING

The subject of probe cleaning for diagnostic purposes is a difficult subject on which to obtain full agreement from all probe users. The probe sampling sequence pertinent to this experiment lasts a few seconds. It is obvious that during that time a steady-state has been established since probe coverage has reached one molecular layer in a matter of 10 to 50 msec in our range of operation.

Fournier and Pigache have reported in Ref. 57 a cleaning sequence of 10 minutes for an argon beam on copper or stainless steel surfaces, with the following properties:

$$0.01 \text{ Coulomb/cm}^2 @ 2 \text{ KeV } (5 \times 10^{-6} \text{ torr})$$

This represents roughly the same power consumed as that of resistive (ohmic) heating at 500°C for the same period. For tungsten and for the region of operation typical for our experimental conditions, we can expect the following estimates (Refs. 79,80)

cleaning time:	10 minutes
beam energy:	1 KeV argon ⁺
beam density:	80 $\mu\text{amp/cm}^2$

We have taken the following data from the literature:

(1) Binding energy on tungsten (300°K)

H ₂ O, N ₂ , O ₂ , CO ₂	$\approx 100 \text{ Kcal/mole}$
CO, CH ₄ , H ₂	$\approx 50 \text{ Kcal/mole}$
Ar	$\approx 2 \text{ Kcal/mole}$

(2) Sticking coefficient on tungsten wire (300°K)

N ₂ , H ₂ , Ar	$\approx 0.1 - 0.3$
O ₂	≈ 0.2

The necessary cleaning power reported by F-P amounts to

$$\text{Ion cleaning: } 8 \times 10^{-5} \text{ KW/cm}^2 @ 10 \text{ min.}$$

$$\text{Ohmic cleaning: } 10 \times 10^{-5} \text{ KW/cm}^2 @ 10 \text{ min.}$$

In fact, we can see that some power is being delivered to the surface layers and probably suffices to knock off most of the top layers. For room temperature in fact, at 5×10^{-5} torr, the N₂ contributes a non-negligible impingement power of the order of

$$W_{N_2} \approx 0.4 \times 10^{-5} \text{ KW/cm}^2$$

We estimate the number of foreign molecules stuck on the surface of the probe with a sticking coefficient $\alpha = 0.2$ on tungsten to get a rate at a pressure of 5×10^{-5} torr (300°K) of

$$\Gamma_{\text{surf}} \simeq \alpha \Gamma_0 \simeq 4 \times 10^{15} \text{ cm}^{-2} \text{ sec}^{-1}$$

If the maximum binding energy is set at about 100 Kcal/mole, this yields for each molecule

$$E_{\text{bind}} \simeq 7 \times 10^{-19} \text{ joule}$$

If we assume that the ions share half of their incoming energy and that the neutral 'hit' on the surface shares also half with its neighbours, then an ion delivers roughly

$$E_{\text{clean}} \simeq \frac{1}{4} E_{\text{ion}}$$

at 1 KeV therefore, one requires about

$$\Gamma_{\text{ion}} \simeq 8 \times 10^{13} \text{ ion/sec-cm}^2$$

or a corresponding power

$$W_{\text{ion clean}} \simeq 1 \times 10^{-5} \text{ KW/cm}^2$$

This simplified model falls a bit short of the figure reported by Pigache for copper and stainless steel. It is quite plausible, however, to assume that the incoming ion would share less than half its kinetic energy and that moreover a compound sticking coefficient would be obtained because of the many species accumulated on the surface. This simplified model is therefore taken as accurate to within an order of magnitude. The impingement currents required (10-100 μA) are in fact easily obtainable with the standard operating conditions of the ion source used for this experiment.

APPENDIX D - MEASUREMENT OF ION SPEED RATIO

USING SMALL COLLIMATED FARADAY CUPS

A method proposed by Fournier and Pigache (Ref. 25) outlines a possibility for measuring the ion speed ratio in mesothermal plasma flows using small collimated Faraday cups. The basic principles invoked are not new. However, these types of collectors, used mostly as ionospheric plasma probes, are greatly refined by achieving an improved angular sensitivity. A simple analytical treatment of the current collection mechanism is required to obtain the basis for the measuring technique. Briefly, it reduces to using the fact that the collimated cup is made velocity selective when its attitude with respect to a plasma stream is varied, from a parallel to a transverse alignment with the bulk velocity of the ions in the flow. The collimated cups have the distinct advantage over the cylindrical probes that the current collection is not sensitive to the presence of a randomized slow-ion content within the beam. This comes from the fact that the 'open window' constitutes a solid angle considerably smaller than 4π . This is a situation virtually the opposite of the one encountered with the 'bare' probe which sees nearly 4π steradians.

The plasma conditions which prevail are compatible with the conditions pertinent to our investigation. The electrons are randomized and possess a given temperature, smaller than say a few volts, and the sheath thickness is large. The probe orifice is considerably smaller than the Debye length. Thus the authors assume that no electrostatic field effects will be influencing the ions near the entrance of the cup. They also assume that the space within the collecting enclosure is field-free and that no significant effects are introduced because of contamination of the internal surfaces of the collector. The system is shown in Fig. A-2. The collector is left floating, for simplicity, while an electron suppressing grid is biased at some negative voltage - 9 volts in this case. Therefore, the problem is reduced to a simplified 'kinetic theory' collection of the ions in the stream.

The cup is first aligned with the beam geometric centre-line and is pitched about its first aperture by an angle α , from 0° to 90° . The collector has an angular acceptance of $2(\Delta\theta)$. The ions in the stream have a predominant directed velocity v and a random velocity w . The system of coordinates (spherical symmetry w , θ , ϕ) is chosen such that the x-axis will be arbitrarily aligned with the direction of v . The ion distribution away from the cup is given by the equilibrium Maxwellian formulation, as was assumed throughout this investigation, i.e.,

$$f_w \propto \exp\{-(w_x - v)^2 + w_y^2 + w_z^2\}$$

The directed speed is given by

$$|v| = \bar{u} \cos\alpha$$

where \bar{u} is the average bulk ion velocity and (α) is the angle between the geometric centreline of the beam and the x-axis. Therefore, the current density is given by

$$\vec{j} \equiv e \int_{\text{open}} f_w \vec{u} d\vec{u}$$

where \vec{u} is the velocity along some line-of-sight from the collector, which is at an angle (β) from the x-axis, i.e.

$$|\vec{u}| = |\vec{w}| \sin\phi \cos(\theta - \beta)$$

The integration must be carried out over the entire 'OPEN AREA' viewed by the collector, and which is defined by the double-aperture system. This range of integration is defined using the following limits:

$$0 \leq w < \infty$$

$$\beta - \Delta\beta \leq \theta \leq \beta + \Delta\beta$$

$$\frac{\pi}{2} - \Delta\beta \leq \phi \leq \frac{\pi}{2} + \Delta\beta$$

The ion current to the collector is found by integrating (j) over all possible lines-of-sight (β) allowed by the collimated orifices. Thus

$$j(\beta, \alpha) = \int_{\text{open}} dw d\theta d\phi w^3 \cos(\theta - \beta) \sin^2\phi \exp[-(w^2 - 2wv \cos\phi \cos\theta + v^2)]$$

where $v = v(\alpha)$ and

$$I'(\alpha) = \int_{-\Delta\beta}^{+\Delta\beta} j(\beta, \alpha) d\beta$$

A nondimensional expression is obtained by normalizing this result using the value at zero degree of incidence ($\alpha = 0$), i.e. the nondimensional ion current is given by

$$I(\alpha) \equiv \frac{I'(\alpha)}{I'(\alpha = 0)}$$

The analytical expression for $j(\beta, \alpha)$ was obtained from Ref. 25 and a plot of $I(\alpha)$ was generated by numerical integration for various ion speed ratios. These results are presented in Fig. A-3. By cross-plotting the peak half-width and the corresponding speed ratio a master plot can be obtained such as the one shown in Fig. A-4. Such a plot readily yields the relation between $\theta_{\frac{1}{2}}$ and S_1 . Consequently the range of sensitivity of the method can be assessed for each aperture angle. A measurement of the absolute peak half-width taken from a current versus angle trace can directly yield the ion speed ratio. Two experimental cases reproduced in Fig. A-5 are shown for comparison in Fig. A-4.

The speed ratios assumed for these two examples are about 44 and 34, respectively, according to the simple geometrical (conical beam) model outlined in Chapter III. The measurements are short of these model values by 50% for the smaller values of S_i and by 20% for the large S_i . Although preliminary results show a limited agreement we can recognize the relatively promising features of this measuring method. The relatively simple construction has the rewarding advantage of giving an excellent resolution of the beam density which can prove useful for accurate mapping of the stream (see Fig. III-6). As with the slender cylindrical probe used in this study, the current angular response of the cups is exceptionally sharp for small angles about the main stream direction. This makes them quite useful in locating the local velocity vector within the beam. Although the currents collected by the cups are considerably smaller than the ones achieved using our cylindrical probes, under similar operating flow conditions, the signals monitored were significantly 'cleaner', as we have mentioned earlier, because of the absence of a background noise (DC offset) coming from slow resident ions in the beam.

APPENDIX E - CRITERIA FOR COLLISIONLESS REGIME

The various criteria delineating the collisionless plasma regime, which is largely satisfied in this investigation involving the use of cylindrical electrostatic probes in a high speed, low density plasma flow, are outlined schematically below:

- (1) The plasma is said to be rarefied when mechanisms involving close encounters are negligible in comparison with collective phenomena, i.e. (macroscopic force-field assumption)

$$n \Lambda_D^3 \gg 1$$

- (2) In the case where condition (1) is finite, an extra condition must be realized so that large disturbances caused by individual particles can be neglected and it reads

$$\lambda_{mfp} \gg d$$

where d in this case refers to the probe diameter.

- (3) One can neglect the effects of neutrals on the charged particle collection if

$$\lambda_a \gg d, \lambda_e \gg d, \lambda_i \gg d$$

provided all mean-free paths (mfp) have been carefully analyzed (see Appendix F).

- (4) Finally, with all three conditions satisfied, the collector must be a 'probe' in the true sense, such that the sampling currents are negligible compared with the currents responsible for maintaining the plasma fluid (Ref. 13), viz

$$i_{\text{probe}} \ll I_{\text{source}}$$

and that the probe serves as an ideal sink for all charged species.

APPENDIX F - LENGTH AND TIME SCALES

(1) Pertinent Mean-Free-Paths

The various mean-free-paths (λ) can be described schematically as follows for a singly ionized argon plasma, where e, i, a, represent electrons, ions and atoms, respectively and P is the neutral pressure

$$(a) \quad \lambda_{aa} \simeq 4.18 P^{-1} \text{ [cm] for } P \text{ [}\mu\text{Hg]}$$

Since only moderate temperatures are involved and, if we assume that no significant rate-process occurs (charge-exchange, recombination...), then for the plasma regime pertinent to this study we have*

$$(b) \quad \lambda_{ia} \simeq \left(\frac{M \mu_i \bar{c}_i}{Z e} \right) \simeq \lambda_{ai}$$

and for charge-transfer, for an ion energy smaller than ~ 1.5 KeV

$$\lambda_{ia}^{CT} \simeq 3.3 \times n_a^{-1} \times 10^{14} \text{ [cm]}$$

For an electron temperature of 1 eV then

$$(c) \quad \lambda_{ea} \simeq 1.2 n_a^{-1} \times 10^{16} \text{ [cm]}$$

and

$$(d) \quad \lambda_{ei} \simeq 2.5 [n_e \ln \Lambda_{ee}]^{-1} \cdot T_e^2 \times 10^{13} \text{ [cm]}$$

for T_e in [eV] and where

$$\Lambda_{ee} \equiv 9 \left[\frac{4\pi}{3} \Lambda_D^3 n_e \right]$$

Moreover if we assume that

$$v_{ei} \simeq \left(\frac{m}{M} \right) v_{ie}$$

we get

$$(e) \quad \lambda_{ie} \simeq \lambda_{ei} \left(\frac{M T_i}{m T_e} \right)$$

$$(f) \quad \lambda_{ee} \simeq \left(\frac{Z^2}{2\sqrt{2}} \right) \lambda_{ei}$$

$$(g) \quad \lambda_{ii} \simeq \lambda_{ee} \cdot \left(\frac{T_i}{T_e} \right)^2 \cdot \left[\frac{\ln \Lambda_{ee}}{Z^4 \ln \Lambda_{ii}} \right]$$

* μ_i : ion mobility.

(2) Pertinent Time Scales

Using the following conditions reported herein,

$$\frac{T_i}{T_e} \approx 1; \quad T_e \approx \frac{1}{3} \text{ eV}$$

$$n_i \lesssim 10^8 \text{ cm}^{-3}$$

$$n_a \approx 5 \times 10^{11} \text{ cm}^{-3} \text{ (test section)}$$

and referring to (1) we can see that all the pertinent mean-free-paths (mfp) are larger than the test section diameter (2.3m). If we now denote the characteristic time-scales by τ , we can see that these time-scales are all significantly longer than the ion drift-time past the probe (τ_{drift}). We summarize them below.

- $\tau_{ei} \equiv \frac{\lambda_{ei}}{\langle v_e \rangle} \approx 5 \times 10^{-5} \text{ sec.}$
- $\tau_{ie} \approx (M/m) \tau_{ei} \approx 1.4 \times 10^{-2} \text{ sec.}$
- $\tau_{ee} \approx (2\sqrt{2})^{-1} \tau_{ei} \approx 2 \times 10^{-5} \text{ sec.}$
- $\tau_{ii} \approx (M/m)^{\frac{1}{2}} \tau_{ee} \approx 3 \times 10^{-4} \text{ sec.}$
- $\tau_{aa} \approx 10^{-2} \text{ sec.}$
- $\tau_{ea} \approx 1.8 \times 10^{-4} \text{ sec.}$
- $\tau_D \equiv \text{ion disturbance time} \equiv \frac{2\pi}{\Omega_{pi}} \approx 5 \times 10^{-5} \text{ sec.}$
- $\tau_{\text{drift}} \equiv \text{ion drift-time}$
 (characteristic length ℓ) $\equiv \frac{\ell}{u} \approx 10^{-6} \text{ sec.}$
- $\tau_{\text{mfr}} \equiv \text{monolayer formation time} \approx 0.2 \text{ sec.}$
 (@ air, 10^{-5} torr)
- $\tau_{\text{trace}} \equiv \text{characteristic 'sample' time} \approx \text{few seconds.}$

APPENDIX G - TANGENT METHODS TO MEASURE T_e

In order to simplify the measurements of the electron temperature from ideal Langmuir probe characteristics, a geometrical construction allows a probe user to extract an approximated value directly from the recorder I-V trace, for both single and double-probe configurations. Using Sonin's analysis (Ref. 13), the single-probe collection can be represented by the relation of the net current

$$j \equiv j_e - j_i$$

where

$$j_e = j_0 \exp(-\psi) \text{ (Boltzmann)}$$

and $\psi \equiv e\phi/kT_e$. Therefore since j_0 is independent of T_e

$$\left(\frac{kT_e}{e} \right)^{-1} \equiv \frac{d}{d\phi} (\ln j_e)$$

Thus at the floating potential ϕ_f we have $j \equiv 0$ and

$$\left(\frac{kT_e}{e} \right) = \frac{j_i(\phi_f)}{\left(\frac{dj}{d\phi} \right) \Big|_{\phi_f} - \left| \frac{dj_i}{d\phi} \right|_{\phi_f}}$$

Therefore, using the simple construction shown in Fig. A-6 for the single-probe characteristics, we have

$$\left(\frac{kT_e}{e} \right) = \frac{c}{\left(\frac{c+b}{a} \right) - \left(\frac{b}{a} \right)} = a$$

such that a quick estimate of T_e can be obtained by taking the tangent at the floating potential point.

For a double-probe constructed with two identical probes we can use the ideal probe characteristic reproduced in Fig. A-6. If (1) and (2) indicate the collection regions for probe No. 1 and probe No. 2, respectively, then from Ref. 66 we have

$$j_1 \equiv j^* \left[\exp \left(\frac{-e \Delta\phi_1}{kT_e} \right) - 1 \right] = j \quad (1)$$

$$j_2 \equiv j^* \left[1 - \exp \left(\frac{-\Delta\phi_2}{kT_e} \right) \right] = j \quad (2)$$

where j^* is the constant ion current to the probes obtained by extrapolation

$$j^* = c \exp \left[\frac{-e \phi_{\text{space}}}{kT_e} \right]$$

Thus if $\Delta\phi_1 + \Delta\phi_2 = 0$ (ideally)

$$\frac{kT_e}{e} \equiv \frac{\left(\frac{j^*}{2} \right)}{\left| \frac{dj}{d\phi} \right|_{\phi_s}}$$

and by construction the estimate for T_e is reduced to measuring the voltage difference $\Delta\phi$ between the intercepts obtained with the slope, or tangent at $\phi = 0$, and the extrapolated values of j^* , i.e.

$$\frac{kT_e}{e} \approx \frac{|\Delta\phi|}{4}$$

APPENDIX H - PROBE STRUCTURAL EFFECTS

The long cylindrical probes are treated here as cantilevered cylindrical thin beams. Indeed, a number of structural effects could threaten their integrity as ideal collectors. Such effects can be summarized as follows:

- . flexure or bending from the action of gravity,
- . oscillation at the natural frequency or at induced frequencies from different sources such as probe traversing mechanism and foundation noise,
- . thermal expansion,
- . non-uniformity of cross-section caused in part by inherent metal properties or by deformation occurring in construction: roughness, extrusions, kinks.

After inspection, we find that all but the first can be considered negligible. The pure bending relationships are given by (Ref. 83):

$$(1) \quad \xi_{\max} = \frac{Wl^3}{8EI} = \underline{\text{max. tip deflection}}$$

where E is Young's Modulus and W is the weight

$$W = \rho \frac{\pi d^2}{4} l$$

and the moment of inertia is given by

$$I = \frac{\pi d^4}{4}$$

For small angles then,

$$(2) \quad \theta_s = \frac{4}{3} \left(\frac{\xi_{\max}}{l} \right) = \underline{\text{initial tip slope @ max. deflection}}$$

$$(3) \quad \omega_{\text{nat}} = \frac{3.515}{l^2} \sqrt{gl \left(\frac{EI}{W} \right)} = \underline{\text{natural frequency}}$$

Upon rearranging (1) we get the normalized maximum deflection

$$\xi_{\max}^* = \left(\frac{\xi_{\max}}{d} \right) = \frac{4\rho l R^3}{E}$$

where R is the probe aspect ratio (l/d) and (ρ) is the material density and

$$\theta_s = \arctan \left(\frac{4}{3} \frac{\xi_{\max}^*}{R} \right)$$

$$\omega_{\text{nat}} = 3.515 \sqrt{\frac{g}{0.008d}} \cdot (\xi_{\max}^*)^{-\frac{1}{2}}$$

for (d) in mils and $g = 32.2 \text{ ft/sec}^2$. Using a typical range of parameters pertinent to this study, we see that one obtains significant bending for a long slender tungsten probe, e.g., using

$$R = 500 \text{ and } d = 0.004 \text{ in.}$$

then

$$\xi_{\max}^* \approx 6.5$$

$$\theta_s \approx 1^\circ$$

$$\omega_{\text{nat}} \approx 30 \text{ Hz}$$

Therefore some care must be taken with our long slender probe ($R \approx 472.5$, $d = 0.004 \text{ in.}$) since anomalous probe effects can be perceived, along with oscillations, which are within the sensitivity of the equipment. In fact, visual observation indicated that such oscillations were present when a nearby experimental facility was operated (UTIAS Low Density Wind Tunnel), and measurements were restricted to 'quiet' periods when using the longer probes.

APPENDIX I - INVERSE PROBLEM FOR LONG CYLINDRICAL PROBES

A systematic method outlined by Sajben and Lee (Ref. 84) demonstrates the concept of solving the inverse problem for the collection of electrostatic probes in general, i.e. when the analytical description of the current collection is known a priori, one can uniquely determine the fundamental state properties of the plasma. The interesting advantage of the method consists in the determination of the plasma properties n_e , T_e , ϕ_{space} for each point on the current-voltage characteristic such that a single trace can yield a set of statistically redundant measurements of these quantities.

In order to verify the overall ability of the method we have attempted to apply it to the steady-dynamic case using the analytical description obtained in Chapter I, together with some experimental I-V traces. Although no quantitative description is provided here the preliminary results have shown that the scheme yields two solutions for T_e and that the region of sensitivity is reduced to a very small range of potentials around the floating value ($V_f \pm 5$ volt).

This fact that the solution for T_e is not unique and that the sensitivity of the method is quite limited is interesting, as it corroborates both the relative non-sensitivity of the ion current collection by the parallel probe to the electron temperature, and the duality of the solution also obtained by our approximation described in Appendix J. Therefore, we conclude that this method would be of no significant help for treating the dynamic case involving long negative parallel cylinders, although it can prove useful to probe users for the study of quiescent plasmas.

APPENDIX J - STATUS OF THE MASS-MOTION EFFECT

The study of the end effect has actually contributed to shed more light on the long debated question whether or not the bulk displacement of the plasma, or the 'mass-motion', would effect the characteristics of the current collection of cylindrical Langmuir probes. We provide in Fig. A-7 an evaluation of the current status on this subject in a fashion advocated by French (Ref. 7).

Two flow regimes are considered, namely that of collisionless thin and thick sheath, respectively*

$$(1) \quad Kn \gg 1; \quad \lambda \gg d \gg \Lambda_D$$

$$(2) \quad Kn \gg 1; \quad \lambda \gg \Lambda_D \geq d$$

The second case corresponds to the regime of interest to this study, and we have indicated it by the hatched region in Fig. I-1. We indicate by YES that either a theory or an experimental investigation, or both, confirm the existence of an effect due to the bulk displacement of the plasma relative to the probe. A NO indicates that no mass-motion effect is observed or predicted. An * indicates that, to our knowledge, the information pertinent to the corresponding conditions is incomplete in the literature.

The region implemented by the results obtained in this investigation, using the analysis of J. R. Sanmartin, is enhanced by the heavy-line frame for the ion collecting region. Another area of interest was covered recently by the work of Taillet et al (Ref. 24). They actually demonstrated both analytically and by computer simulation that the electron collection region would indeed be altered by the plasma motion. This interesting prediction has effectively been corroborated by the experimental results obtained by Koopman and Segall using a high-speed plasma produced when a pulsed laser beam impacts on copper or aluminum targets (Ref. 32).

Finally, it can be pointed out that the experimental apparatus used in conjunction with the present investigation could prove useful in completing this survey for the regimes requiring more elucidation.

*Kn: Knudsen number $\equiv \lambda/r_p$ and r_p the probe radius ($d = 2r_p$)

APPENDIX K - ESTIMATE OF ELECTRON TEMPERATURE

As we have intuitively indicated in Chapter I the end effect is relatively insensitive to the electron temperature. However, we have seen that the effective scaling length $\bar{\delta}$ of the potential field around the probe needs to be adjusted because the finite probe draws ions from a region within the cylindrical sheath which is smaller than the one estimated by the classical sheath theory. This restricted region is effectively defined by the limits:

$$\tau_l \lesssim 3$$

$$0 < \frac{r}{r_p} < \rho_m$$

This has justified the definition of a characteristic field length $\bar{\delta}$ which is described by Sanmartin using the following exact relation

$$\bar{\delta}^{-1} \equiv \ln(\epsilon^{-1}) + Y(\epsilon, \psi_p) \quad (1)$$

Sanmartin, in fact, does not define $Y(\epsilon, \psi_p)$ analytically, but rather provides the graphical description we have reproduced in Fig. A-8. We have fitted these curves numerically. This has yielded the following estimate ($\pm 5\%$)

$$Y(\epsilon, \psi_p) \simeq 0.23 - 0.1 \ln(\epsilon^{-1}) + 0.42 |\psi_p|^{0.3} \quad (2)$$

This estimate was compared with the approximation explicitly given by Sanmartin for $\bar{\delta}$ in I.39. Therefore, using Eq. I.38 his results read

$$\bar{\delta}_s^{-1} \simeq \ln(\epsilon^{-1}) - 0.5 + \ln \sqrt{2\psi_p \bar{\delta}} \quad (3)$$

whereas

$$\bar{\delta}_{\text{fit}}^{-1} \simeq 0.9 \ln(\epsilon^{-1}) + 0.23 + 0.42 \psi_p^{0.3} \quad (4)$$

This comparison is outlined in two tables shown in Fig. A-9 for a range of parameters. The agreement is excellent except for the comparison between the values of $\ln(\epsilon^{-1})$ predicted at large probe bias (ψ_p).

Since our self-consistent method described in Section IV.2.3 actually determines $\bar{\delta}$ using experimental measurements exclusively related to ion features and to probe characteristics, it is conceivable to expect some electron temperature information out of the value of $\bar{\delta}_{\text{self}}$. The relatively small sensitivity of $\bar{\delta}$ to electron temperature is, however, apparent from Fig. A-11. We have plotted the expression obtained in Eq. (3) using the exact relation for ϵ and ψ_p , namely

$$\epsilon \equiv \frac{r_p}{\Lambda_D(T_e)}$$

$$\psi_p \equiv \psi_p(T_e) = \frac{e\phi_p}{kT_e}$$

and we notice that a three-order of magnitude change in T_e implies merely a $\pm 20\%$ change in $\bar{\phi}$, using a typical set of experimental conditions.

Nevertheless, an attempt to measure T_e indirectly was made. This method implies that once $\bar{\phi}$ is known

$$\bar{\phi} = \bar{\phi}_{\text{self}}$$

one must find an agreement between the value of function $Y(\epsilon, \psi_p)$ obtained from (1) and from (2), that is:

$$Y_1 \equiv Y_1(\epsilon, \psi_p) = \bar{\phi}_{\text{self}}^{-1} - \ln(\epsilon^{-1})$$

$$Y_2 \equiv Y_2(\epsilon, \psi_p) \simeq 0.23 - 0.1 \ln(\epsilon^{-1}) + 0.42 \psi_p^{0.3}$$

with

$$F \equiv |Y_1 - Y_2| \equiv 0 \quad (5)$$

If, however, one plots $F(\epsilon)$, one notices that for certain values of $\bar{\phi}$ condition (5) is never satisfied. This has led us to use an approximate solution of (5) using

$$\frac{\partial F}{\partial \epsilon} \equiv 0 \quad @ \quad \epsilon = \epsilon_m$$

as shown in Fig. A-10. The estimates of ϵ using this scheme, and labelled ϵ_m , are inherently only marginally accurate. For instance, an error of less than 10% on the value of $\ln(\epsilon^{-1})$ leads to error of about 50% on the value of ϵ with $\epsilon \simeq 0.01$. Nevertheless, an average value of T_e was obtained with this relatively coarse method. It is on average about 100% in disagreement with the direct measurements of T_e (Chapter III), i.e.

$$T_{em} \simeq 2T_e$$

as shown in the table presented in Fig. A-11. This is nevertheless quite interesting since the single-probe results also suggest a measured value of T_e about a factor of 2 too high. This, in fact, constitutes an extra indication that the bulk motion does introduce some distortion in the electron temperature sensitive region of the current versus voltage probe characteristic, as was suggested in typical I-V probe responses (see Fig. IV-2), and as was corroborated elsewhere (Appendix J).

UTIAS Report No. 202

Institute for Aerospace Studies, University of Toronto
ION TEMPERATURE MEASUREMENT IN A FLOWING COLLISIONLESS PLASMA USING AN END EFFECT OF CYLINDRICAL LANGMUIR PROBES

Mercure, H. P. E. 91 pages 80 figures
1. Ion temperature probe 2. Probes in collisionless plasma 3. End-effect
4. Langmuir probes 5. Probes in plasma flow
I. Mercure, H.P.E.

II. UTIAS Report No. 202

An experimental verification of the end effect theory of long cylindrical Langmuir probes in a high-speed collisionless plasma flow is reported. This effect is observed as a sharp departure from the predicted 'infinite probe' current when a strongly negative probe is aligned with the flow. Both the height and the width of the ion current peak measured about the zero-degree attitude are strongly sensitive to ion temperature. The effect is verified for a mesothermal argon plasma with probe radius to Debye length ratio $0.005 < \epsilon < 0.5$ and for ion to electron temperature ratios close to unity. A scheme is developed to obtain a self-consistent measurement of the ion temperature using the basic characteristics of the finite-probe angular response after a modification of J. R. Sammartin's theory.

A versatile ion source was constructed after a state-of-the-art electrostatic ion thruster. It provides, together with a large size vacuum chamber, a simulation facility for which the plasma stream characteristics can be tailored and the ion speed ratio easily modeled for diagnostic purposes.

A range of flow conditions and of probe parameters are investigated and the overall applicability and reliability of the method to measure T_i are assessed. Potential areas of applications are outlined.

Available copies of this report are limited. Return this card to UTIAS, if you require a copy.



UTIAS Report No. 202

Institute for Aerospace Studies, University of Toronto
ION TEMPERATURE MEASUREMENT IN A FLOWING COLLISIONLESS PLASMA USING AN END EFFECT OF CYLINDRICAL LANGMUIR PROBES

Mercure, H. P. E. 91 pages 80 figures
1. Ion temperature probe 2. Probes in collisionless plasma 3. End-effect
4. Langmuir probes 5. Probes in plasma flow
I. Mercure, H.P.E.

II. UTIAS Report No. 202

An experimental verification of the end effect theory of long cylindrical Langmuir probes in a high-speed collisionless plasma flow is reported. This effect is observed as a sharp departure from the predicted 'infinite probe' current when a strongly negative probe is aligned with the flow. Both the height and the width of the ion current peak measured about the zero-degree attitude are strongly sensitive to ion temperature. The effect is verified for a mesothermal argon plasma with probe radius to Debye length ratio $0.005 < \epsilon < 0.5$ and for ion to electron temperature ratios close to unity. A scheme is developed to obtain a self-consistent measurement of the ion temperature using the basic characteristics of the finite-probe angular response after a modification of J. R. Sammartin's theory.

A versatile ion source was constructed after a state-of-the-art electrostatic ion thruster. It provides, together with a large size vacuum chamber, a simulation facility for which the plasma stream characteristics can be tailored and the ion speed ratio easily modeled for diagnostic purposes.

A range of flow conditions and of probe parameters are investigated and the overall applicability and reliability of the method to measure T_i are assessed. Potential areas of applications are outlined.

Available copies of this report are limited. Return this card to UTIAS, if you require a copy.



UTIAS Report No. 202

Institute for Aerospace Studies, University of Toronto
ION TEMPERATURE MEASUREMENT IN A FLOWING COLLISIONLESS PLASMA USING AN END EFFECT OF CYLINDRICAL LANGMUIR PROBES

Mercure, H. P. E. 91 pages 80 figures
1. Ion temperature probe 2. Probes in collisionless plasma 3. End-effect
4. Langmuir probes 5. Probes in plasma flow
I. Mercure, H.P.E.

II. UTIAS Report No. 202

An experimental verification of the end effect theory of long cylindrical Langmuir probes in a high-speed collisionless plasma flow is reported. This effect is observed as a sharp departure from the predicted 'infinite probe' current when a strongly negative probe is aligned with the flow. Both the height and the width of the ion current peak measured about the zero-degree attitude are strongly sensitive to ion temperature. The effect is verified for a mesothermal argon plasma with probe radius to Debye length ratio $0.005 < \epsilon < 0.5$ and for ion to electron temperature ratios close to unity. A scheme is developed to obtain a self-consistent measurement of the ion temperature using the basic characteristics of the finite-probe angular response after a modification of J. R. Sammartin's theory.

A versatile ion source was constructed after a state-of-the-art electrostatic ion thruster. It provides, together with a large size vacuum chamber, a simulation facility for which the plasma stream characteristics can be tailored and the ion speed ratio easily modeled for diagnostic purposes.

A range of flow conditions and of probe parameters are investigated and the overall applicability and reliability of the method to measure T_i are assessed. Potential areas of applications are outlined.

Available copies of this report are limited. Return this card to UTIAS, if you require a copy.



UTIAS Report No. 202

Institute for Aerospace Studies, University of Toronto
ION TEMPERATURE MEASUREMENT IN A FLOWING COLLISIONLESS PLASMA USING AN END EFFECT OF CYLINDRICAL LANGMUIR PROBES

Mercure, H. P. E. 91 pages 80 figures
1. Ion temperature probe 2. Probes in collisionless plasma 3. End-effect
4. Langmuir probes 5. Probes in plasma flow
I. Mercure, H.P.E.

II. UTIAS Report No. 202

An experimental verification of the end effect theory of long cylindrical Langmuir probes in a high-speed collisionless plasma flow is reported. This effect is observed as a sharp departure from the predicted 'infinite probe' current when a strongly negative probe is aligned with the flow. Both the height and the width of the ion current peak measured about the zero-degree attitude are strongly sensitive to ion temperature. The effect is verified for a mesothermal argon plasma with probe radius to Debye length ratio $0.005 < \epsilon < 0.5$ and for ion to electron temperature ratios close to unity. A scheme is developed to obtain a self-consistent measurement of the ion temperature using the basic characteristics of the finite-probe angular response after a modification of J. R. Sammartin's theory.

A versatile ion source was constructed after a state-of-the-art electrostatic ion thruster. It provides, together with a large size vacuum chamber, a simulation facility for which the plasma stream characteristics can be tailored and the ion speed ratio easily modeled for diagnostic purposes.

A range of flow conditions and of probe parameters are investigated and the overall applicability and reliability of the method to measure T_i are assessed. Potential areas of applications are outlined.

Available copies of this report are limited. Return this card to UTIAS, if you require a copy.



UNCLASSIFIED

SECURITY CLASSIFICATION OF THIS PAGE (When Data Entered)

19 REPORT DOCUMENTATION PAGE		READ INSTRUCTIONS BEFORE COMPLETING FORM
1. REPORT NUMBER AFOSR - TR - 76 - 1411	2. GOVT ACCESSION NO.	3. RECIPIENT'S CATALOG NUMBER
4. TITLE (and Subtitle) ION TEMPERATURE MEASUREMENT IN A FLOWING COLLISIONLESS PLASMA USING AN END EFFECT OF CYLINDRICAL LANGMUIR PROBES.	5. TYPE OF REPORT & PERIOD COVERED INTERIM rept.	
7. AUTHOR(s) HUBERT P. E. MERCURE	6. PERFORMING ORG. REPORT NUMBER Report No 202	
9. PERFORMING ORGANIZATION NAME AND ADDRESS UNIVERSITY OF TORONTO INSTITUTE FOR AEROSPACE STUDIES, 4925 DUFFERIN ST DOWNSVIEW, ONTARIO, CANADA M3H 5T6	8. CONTRACT OR GRANT NUMBER(s) AF-AFOSR 73-2091-71	
11. CONTROLLING OFFICE NAME AND ADDRESS AIR FORCE OFFICE OF SCIENTIFIC RESEARCH/NA BLDG 410 BOLLING AIR FORCE BASE, D C 20332	10. PROGRAM ELEMENT, PROJECT, TASK AREA & WORK UNIT NUMBERS 681307 9781-03 61102F	
14. MONITORING AGENCY NAME & ADDRESS (if different from Controlling Office) 12 157P. 14 UTIAS-202	12. REPORT DATE Jul 1976 for Dec 75	
	13. NUMBER OF PAGES 46	
	15. SECURITY CLASS. (of this report) UNCLASSIFIED	
15a. DECLASSIFICATION/DOWNGRADING SCHEDULE		
16. DISTRIBUTION STATEMENT (of this Report) Approved for public release; distribution unlimited.		
17. DISTRIBUTION STATEMENT (of the abstract entered in Block 20, if different from Report)		
18. SUPPLEMENTARY NOTES		
19. KEY WORDS (Continue on reverse side if necessary and identify by block number) ION TEMPERATURE PROBE PROBES IN COLLISIONLESS PLASMA END-EFFECT LANGMUIR PROBES PROBES IN PLASMA FLOW		
20. ABSTRACT (Continue on reverse side if necessary and identify by block number) An experimental verification of the end effect theory of long cylindrical Langmuir probes in a high-speed collisionless plasma flow is reported. This effect is observed as a sharp departure from the predicted "infinite probe" current when a strongly negative probe is aligned with the flow. Both the height and the width of the ion current peak measured about the zero-degree attitude are strongly sensitive to ion temperature. The effect is verified for a mesothermal argon plasma with probe radius to Debye length ratio $0.005 < \epsilon < 0.5$ and for ion to electron temperature ratios close to unity. A scheme is developed to obtain a		

DD FORM 1 JAN 73 1473

EDITION OF 1 NOV 65 IS OBSOLETE

UNCLASSIFIED

SECURITY CLASSIFICATION OF THIS PAGE (When Data Entered)

178 920 KB

UNCLASSIFIED

SECURITY CLASSIFICATION OF THIS PAGE(When Data Entered)

self-consistent measurement of the ion temperature using the basic characteristics of the finite-probe angular response after a modification of J R Sanmartin's theory. A versatile ion source was constructed after a state-of-the-art electrostatic ion thruster. It provides, together with a large size vacuum chamber, a simulation facility for which the plasma stream characteristics can be tailored and the ion speed ratio easily modeled for diagnostics purposes. A range of flow conditions and of probe parameters are investigated and the overall applicability and reliability of the method to measure T_i are assessed. Potential areas of applications are outlined.

UNCLASSIFIED

SECURITY CLASSIFICATION OF THIS PAGE(When Data Entered)